



# UCC

University College Cork, Ireland  
Coláiste na hOllscoile Corcaigh



# Tyndall

National Institute  
Institiúid Náisiúnta

## European Semiconductor Laser Workshop

# ESLW 2019

27-28 September 2019

Tyndall National Institute  
University College Cork  
Cork, Ireland

## Book of abstracts

Sponsored by



## **ESLW Organising Committee**

### **Workshop Chair**

**Bryan Kelleher**

University College Cork & Tyndall National Institute

### **Local Organising Committee**

**Benjamin Lingnau**

University College Cork & Tyndall National Institute

**John McInerney**

University College Cork & Tyndall National Institute

**Frank Peters**

University College Cork & Tyndall National Institute

**William Whelan-Curtin / Liam O'Faolain**

Cork Institute of Technology & Tyndall National Institute

### **Technical Committee**

**Stephane Barland**

Université Côte d'Azur (FR)

**Stefan Breuer**

Technische Universität Darmstadt (DE)

**Lorenzo Columbo**

Politecnico di Torino (IT)

**Alejandro Giacomotti**

CNRS/C2N, Paris (FR)

**Antonio Hurtado**

University of Strathclyde (UK)

**Julien Javaloyes**

University of the Balearic Islands, Palma de Mallorca (ES)

**Bryan Kelleher**

University College Cork & Tyndall National Institute (IE)

**Sylwester Latkowski**

Technische Universiteit Eindhoven, Eindhoven (NL)

**Kathy Lüdge**

Technische Universität Berlin (DE)

**Miguel Soriano**

Instituto de Fisica Interdisciplinar y Sistemas Complejos, Palma de Mallorca (ES)

**Guy Verschaffelt**

Vrije Universiteit Brussel (BE)

**Martin Virte**

Vrije Universiteit Brussel (BE)

# Contents

<b>InP Quantum Dot Monolithic Mode-Locked Lasers for Ultrashort Pulse Generation at 735 nm</b>	
C. P. Allford, Z. Li, S. Shutts, A. F. Forrest, R. Alharbi, A. B. Krysa, M. A. Cataluna and P. M. Smowton	4
<b>Optical Gain and Absorption of 1.55 <math>\mu\text{m}</math> Emitting InAs Quantum Dot Lasers Directly Grown on (001) Silicon</b>	
C. P. Allford, Z. Li, S. Shutts, B. Shi, W. Luo, K. M. Lau and P. M. Smowton	6
<b>Effects of power-split ratio and phase delay on performance of self-mode-locked QDash lasers subject to asymmetric dual-loop optical feedback</b>	
H. Asghar, E. Sooudi and J. G. McInerney	8
<b>Photonic integrated circuit extended cavity passively mode-locked symmetric ring laser with dual absorber</b>	
D. Auth, M.-C. Lo, C. Weber, P. Fiala, P. Sauer, G. Carpintero and S. Breuer	10
<b>Self-consistent thermal-opto-electronic model for the dynamics in high-power semiconductor lasers</b>	
U. Bandelow, M. Radziunas, J. Fuhrmann, A. Zeghuzi, H.-J. Wünsche and H. Wenzel	12
<b>InP based integrated tunable laser systems for optical coherence tomography and strain sensing</b>	
E. Bente, S. Andreou, R. Pajković, J. Hazan and K. Williams	14
<b>Metamorphic heterostructures: new material concepts for telecom lasers and visible light-emitting diodes</b>	
S. Bogusevski, C. A. Broderick and E. P. O'Reilly	16
<b>High-frequency chaotic dynamics of laser diodes with long phase-conjugate feedback</b>	
G. Bouchez, D. Wolfersberger and M. Sciamanna	18
<b>High Power Surface Emitting Superluminescent LEDs</b>	
R. Cahill, J. Morales and B. Corbett	20
<b>Type II excitability in optical injected quantum dot lasers</b>	
M. Dillane, J. Roberson, D. Goulding, A. Hurtado and B. Kelleher	22
<b>Nonlinear laser dynamics induced by injection of a frequency comb</b>	
Y. Doumbia, T. Malica, D. Wolfersberger, K. Panajotov and M. Sciamanna	24
<b>The ESLW from 1983 to 2019: personal experiences and perspectives – Semiconductor emitters going from Telecom to Quantum</b>	
W. Elsässer	26
<b>Optical frequency comb quantum dash lasers subject to time-delayed optical self-injection</b>	
P. Fiala, D. Auth, C. Weber, Q. Gaimard, A. Ramdane and S. Breuer	28
<b>Third Order Dispersion in Optical Time Delayed Systems</b>	
C. Schelte, P. Camelin, G. Huyet, M. Marconi, M. Giudici, I. Sagnes, G. Beaudoin, A. Garnache, J. Javaloyes and S. Gurevich	30
<b>30 GHz and 45 Gbps with <math>\phi \sim 7.5 \mu\text{m}</math> VCSELs</b>	
N. Haghighi, P. Moser, M. Zorn and J. A. Lott	32
<b>Modelling the Effect of Dislocations in III-V Lasers on Si</b>	
C. Hantschmann, Z. Liu, M. C. Tang, A. J. Seeds, H. Y. Liu, I. H. White and R. V. Penty	34
<b>On-chip Photonic Delay-based Reservoir Computing</b>	
K. Harkhoe, G. Verschaffel, A. Katumba, P. Bienstman and G. Van der Sande	36
<b>Spectral Switches in Microwave Oscillation of Semiconductor Laser with Optoelectronic feedback</b>	
M. S. Islam, G. Coget, A. V. Kovalev, A. Locquet, E. A. Viktorov and D. S. Citrin	38

<b>Polarization dynamics of a VCSEL with thermally tuned birefringence</b> N. Jung, M. Lindemann, P. Stadler, T. Pusch, R. Michalzik, M. R. Hofmann and N. C. Gerhardt .....	40
<b>Tailoring the Linewidth of Quantum Dot Lasers via the Temperature</b> F. Köster, J. Duan, H. Huang, B. Dong, Z. Lu, P. J. Poole, F. Grillot and K. Lüdge .....	42
<b>Multimode Dynamics of Long-Cavity Fabry-Pérot Quantum-Dot Lasers</b> B. Lingnau, James O’Callaghan, B. Corbett and B. Kelleher .....	44
<b>Temperature Distribution Analysis of Multi-Section Slotted Semiconductor Lasers</b> R. McKenna, S. T. Naimi, S. Corbett, D. McCloskey and J. F. Donegan .....	46
<b>Semiconductor Fano lasers</b> Jesper Mørk, T. S. Rasmussen, Y. Yu, D. Bekele, E. Semenova, A. Sakanas and K. Yvind .....	48
<b>Optical coupling of quantum-dot micropillar lasers with perspective towards neuromorphic computing</b> Xavier Porte .....	49
<b>Neuromorphic photonic circuits with VCSEL-based artificial spiking neurons</b> J. Robertson, M. Hejda, J. Bueno, E. Wade and A. Hurtado .....	50
<b>Nanoscale light sources for neuromorphic nanophotonic circuits</b> B. Romeira, P. Moura, C. Maibohm, and J. B. Nieder .....	52
<b>Optical frequency comb generation via pulse excitation using step-recovery diodes in an optically-injected semiconductor laser</b> A. Rosado, E. P. Martin, A. Pérez-Serrano, J. M. G. Tijero, I. Esquivias and P. M. Anandarajah .....	53
<b>Tunable Kerr frequency combs and cavity solitons in a nonlinear time-delayed Gires-Tournois interferometer</b> C. Schelte, A. Pimenov, A. G. Vladimirov, J. Javaloyes and S. V. Gurevich .....	55
<b>Mode-Hop Suppression by Cavity-Length Engineering in Hybrid External Cavity Photonic Crystal Lasers</b> R. Sheehan, P. Singaravelu, S. Butler, G. Devarapu, S. Hegarty and L. O’Faoláin .....	57
<b>Frequency Locking Mechanisms enabled by Optical Frequency Comb Injection</b> K. Shortiss, B. Lingnau, F. Dubois, B. Kelleher and F. H. Peters .....	59
<b>Spatiotemporal extreme events in spatially extended semiconductor lasers</b> G. Tissoni .....	61

# InP Quantum Dot Monolithic Mode-Locked Lasers for Ultrashort Pulse Generation at 735 nm

C. P. Allford<sup>1\*</sup>, Z. Li<sup>1</sup>, S. Shutts<sup>1</sup>, A. F. Forrest<sup>2</sup>, R. Alharbi<sup>1,3</sup>, A. B. Krysa<sup>4</sup>, M. A. Cataluna<sup>2</sup> and P. M. Smowton<sup>1</sup>

<sup>1</sup>EPSRC Future Compound Semiconductor Manufacturing Hub, School of Physics & Astronomy, Cardiff University, Queen's Buildings, The Parade, Cardiff, CF23 3AA, United Kingdom.

<sup>2</sup>Institute of Photonics and Quantum Sciences, School of Engineering and Physical Sciences, Heriot-Watt University, Edinburgh Campus, Edinburgh, EH14 4AS, United Kingdom.

<sup>3</sup>Physics Department, King Abdulaziz University, Jeddah, Saudi Arabia.

<sup>4</sup>EPSRC National Centre for III-V Technologies, University of Sheffield, Sheffield, United Kingdom, S1 3JD.

\*allfordcp1@cardiff.ac.uk

**Abstract:** Monolithic InP/GaInP quantum dot passively mode-locked lasers are realised for the first time, emitting in the 730 nm waveband. Devices with total cavity length between 2 mm and 3.5 mm, with uncoated cleaved facets, and saturable absorber (SA) sections representing approximately 20% of the total cavity length have been found to Q-switch, mode-lock or both, depending on operating regime. The influence of bias conditions on the characteristics of lasers with a 3 mm cavity length have been explored, resulting in generation of pulses at 734.7 nm with pulse repetition rates of 12.55 GHz and pulse durations down to  $\approx 6$  ps.

## 1. Introduction

Semiconductor monolithic ultrashort pulse mode-locked lasers (MLLs) which emit in the visible to near infrared regions are promising candidates to provide low cost, efficient and small footprint alternatives to the Ti:Sapphire laser, specifically in biomedical imaging and fluorescence studies, and for 'lab-on-a-chip' integrated applications.

Due to the broad optical gain features exhibited by quantum dot (QD) materials, there is excellent potential to achieve ultrashort pulses [1] in these material systems. However, much of the work in similar wavelength ranges, has, to-date, been focused on quantum well (QW) materials [2], rather than QDs. Here we demonstrate mode-locking in simple two-section monolithic structures using InP QDs as the active region, in an epitaxial structure that can be extended to cover the 630-780 nm wavelength range [3, 4, 5]. We report on the first measurements of ultrashort pulses from InP QD mode-locked lasers and explore the range of bias conditions and cavity lengths over which mode-locking has been achieved.

## 2. Experimental Setup

The InP QD laser structures were grown by MOVPE on n-GaAs (100) substrates, orientated  $10^\circ$  off toward  $\langle 111 \rangle$ . Self-assembled InP QDs were covered by slightly tensile strained GaInP QWs and separated by AlGaInP barriers, with AlInP cladding lasers forming the remainder of the waveguide (Figure 1). Figure 2 shows a schematic diagram of simple two-section mode-locked lasers, where  $2 \mu\text{m}$  wide shallow-etched ridge waveguides were fabricated, followed by planarization using Benzocyclobutene (BCB). Two section P-type contacts were defined across the ridgetops after BCB back-etching, with a  $20 \mu\text{m}$  gap between the gain and saturable absorber (SA) sections. A wet etch was used to remove the highly conductive p-GaAs layer between the gain and SA contacts to improve electrical isolation. Lasers with total cavity lengths between 2.0 mm and 3.5 mm, with cleaved facets and saturable absorber sections representing approximately 20% of the total cavity length were examined. Broad-area oxide-stripe non-lasing segmented contact devices were also fabricated to measure the material optical gain and modal absorption spectra, via the segmented contact method.

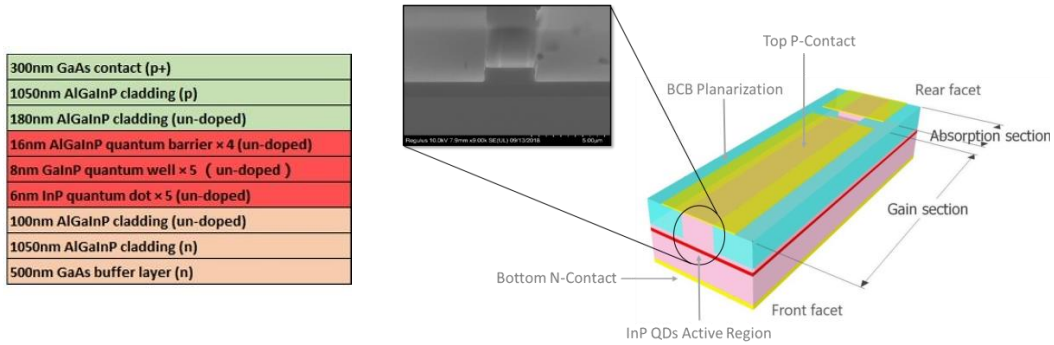


**Figure 1:** InP/GaInP DWELL laser structure. **Figure 2:** Diagram of passively mode-locked laser, with SEM image (inset)

The mode-locking properties of the lasers were measured under continuous-wave current conditions, with reverse DC bias applied across the saturable absorber. The heatsink temperature of the device was maintained at  $\approx 10$  °C. To examine the device behaviour under identical bias conditions, the front-facet emission was free-space coupled into an autocorrelator operating in non-collinear mode and a flip-mirror used to fibre-couple the emission into an optical spectrum analyser and a fast-photodetector connected to an electrical spectrum analyser.

### 3. Results and Discussion

The repetition rates for the 2.0 mm, 2.5 mm and 3.5 mm cavity length lasers operating in mode-locked regimes were found to be 18.89 GHz, 14.98 GHz and 10.74 GHz respectively, which follows the expected repetition rates from cavity round-trip calculations.

The mode-locking properties of lasers with a 3.0 mm total cavity length have been explored over a range of gain and saturable absorber bias conditions. Regions of Q-Switching, unstable mode-locking and stable mode-locking have been observed in both RF and pulse duration measurements, with optimal bias conditions for the 3.0 mm total cavity length devices found to be a gain current,  $I_{\text{gain}} = 80$  mA and saturable absorber reverse bias,  $V_{\text{SA}} = 2.74$  V. Figure 3 shows the RF signal measured under optimal bias conditions, demonstrating strong mode-locking with a signal strength  $\approx 50$  dB above the noise floor, and a strong second harmonic signal (inset). The repetition frequency for the 3.0 mm cavity length was found to be  $\approx 12.549$  GHz with a 3 dB linewidth of  $\approx 21.3$  KHz. The pulse duration under optimal bias conditions was measured to be  $\approx 6$  ps, using a Sech<sup>2</sup> fit, and is shown in Figure 4, with the lasing spectrum showing emission at 734.7 nm (inset). The average power emitted from the front facet of the laser under optimal conditions was found to exceed 1.74 mW, with a peak power greater than 23.11 mW.

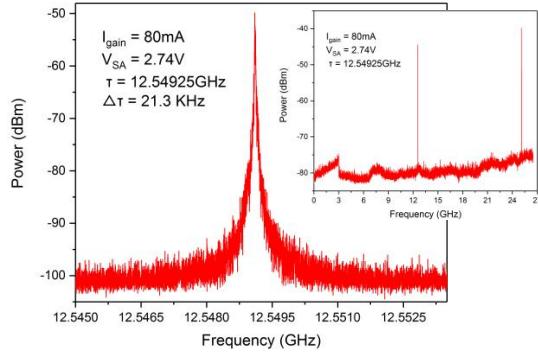


**Figure 3:** RF spectrum of 3 mm cavity length laser, with repetition frequency of 12.549 GHz and 3 dB bandwidth of 21.3 KHz. A wider frequency range is also shown (inset), with the fundamental frequency and second harmonic clearly visible.

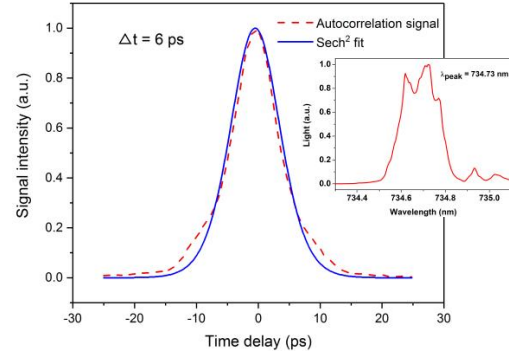


**Figure 4:** Autocorrelation signal (dashed) and Sech<sup>2</sup> fit (solid), resulting in a calculated pulse duration of  $\approx 6$  ps. The optical spectrum is also shown inset, with a lasing wavelength 734.7 nm and spectral bandwidth of  $\approx 110$  GHz (0.2 nm).

### 4. Conclusion

We present the first report of ultrashort pulse generation in monolithic InP/GaInP QD passively mode-locked lasers in the 730 nm waveband. The influence of bias conditions on the characteristics of lasers with a 3 mm cavity length have been explored and resulted in generation of pulses at 734.7 nm with pulse repetition rates of 12.55 GHz, with a 3 dB bandwidth of 21.3 KHz and pulse durations down to  $\approx 6$  ps under optimal bias conditions. InP QD mode-locked lasers operating in this regime have therefore been shown to be promising candidates for low cost, small footprint and efficient alternatives to the Ti:Sapphire laser.

This research is supported by the UK Engineering Physical Sciences Research Council (EPSRC) under grant number EP/P006973/1.

### 5. References

- [1] E. U. Rafailov, M. A. Cataluna and W. Sibbett, "Mode-locked quantum-dot lasers," *Nature Photonics*, vol. 1, pp. 395-401, (2007).
- [2] H. Wang, L. Kong, A. Forrest, D. Bajek, S. E. Haggett, X. Wang, B. Cui, J. Pan, Y. Ding and M. A. Cataluna, "Ultrashort pulse generation by semiconductor mode-locked lasers at 760 nm," *Optics Express*, vol. 22, no. 21, pp. 25940-25946, (2014).
- [3] P. M. Smowton, J. Lutti, G. M. Lewis, A. B. Krysa, J. S. Roberts and P. A. Houston, "InP-GaInP quantum-dot lasers emitting between 690-750 nm," *IEEE Journal of selected topics in quantum electronics*, vol. 11, no. 5, pp. 1035-1040, (2005).
- [4] S. Shutts, S. Elliott, P. Smowton and A. Krysa, "Exploring the wavelength range of InP/AlGaInP QDs and application to dual-state lasing," *Semiconductor Science and Technology*, vol. 30, no. 4, p. 044002, (2015).
- [5] I. Karomi, P. Smowton, S. Shutts, A. Krysa and R. Beanland, "InAsP quantum dot lasers grown by MOVPE," *Optics Express*, vol. 23, no. 21, pp. 27282-27291, (2015).

# Optical Gain and Absorption of 1.55 $\mu\text{m}$ Emitting InAs Quantum Dot Lasers Directly Grown on (001) Silicon

C. P. Allford<sup>1\*</sup>, Z. Li<sup>1</sup>, S. Shutts<sup>1</sup>, B. Shi<sup>2</sup>, W. Luo<sup>2</sup>, K. M. Lau<sup>2</sup> and P. M. Smowton<sup>1</sup>

<sup>1</sup>EPSRC Future Compound Semiconductor Manufacturing Hub, School of Physics & Astronomy, Cardiff University, Queen's Buildings, The Parade, Cardiff, CF23 3AA, United Kingdom.

<sup>2</sup> Department of Electronic and Computer Engineering, Hong Kong University of Science and Technology, Hong Kong. \*allfordcp1@cardiff.ac.uk

**Abstract:** Broad-area InAs quantum dot lasers and segmented contact devices have been fabricated using monolithically grown InAs/InAlGaAs/InP active structures on nano-patterned (001) silicon substrates. The device optoelectronic properties, optical gain and absorption have been studied and compared to structures with a nominally identical active region, grown on a native indium phosphide substrate.

## 1. Introduction

Quantum dot (QD) laser structures have been considered as promising candidates for the realization of monolithic integration of III-V laser active structures grown directly on (001) silicon, due to physical advantages such as less sensitivity to material defects and higher operation temperature, whilst providing broad optical gain bandwidth. Considerable progress has been made in recent years in achieving 1.3  $\mu\text{m}$  QD lasers on silicon [1, 2], which rely on epitaxial structures with InAs QDs incorporated into GaAs-based alloys ( $\approx 4\%$  lattice mismatch to silicon). For applications in future optical communication and sensing industries utilising silicon photonic integration technology there is increasing demand to push the lasing spectra of silicon based QD lasers into the 1.55  $\mu\text{m}$  band. To realise an efficient, compact QD laser for these applications, requires achieving high-quality growth of InAs QD active regions and the overall laser structure whilst incorporating InP-based materials. These have larger lattice mismatch,  $\approx 8\%$  with silicon, which inevitably introduces more material defects during growth. Only recently have both optically pumped and the more alluring electrically pumped silicon-based 1.55  $\mu\text{m}$  QD lasers been reported [3, 4]. However, a more delicate growth technique and refined laser structure design must be developed to enhance device performance to meet the requirements for practical use.

We report the first optical gain and absorption measurements of 1.55  $\mu\text{m}$  InAs QD laser structures grown on silicon (001) substrates and compare to a nominally identical laser structure grown on a native InP substrate. These results can be used to further understand and optimise the laser structure design and inform future material growth.

## 2. Experimental Setup

To achieve high quality growth and overcome the large lattice mismatch between Si and InP, a Si (001) substrate fully patterned with nano V-grooves is used. The Si (111) surfaces exposed by the nano V-groove pattern has been shown to be effective in trapping and terminating defects [4, 5, 6]. A GaAs buffer and InGaAs/InP superlattice layers were grown to filter threading dislocations and planarize the surface. The active region was formed by three layers of InAs QDs with InAlGaAs barriers and InP cladding layers (Figure 1a). Differential contrast imaging (DIC) of the as-grown wafer surface however reveals considerable surface morphology and defects remain (Figure 1b).

Broad-area co-planar stripe lasers and non-lasing segmented contact devices were fabricated using standard photolithography and inductively coupled plasma etching techniques. The mesa width was defined to be 100  $\mu\text{m}$  wide and etched  $\approx 3 \mu\text{m}$  to the InP n-contact layer. 50  $\mu\text{m}$  wide p-contact and n-contact metals were deposited to

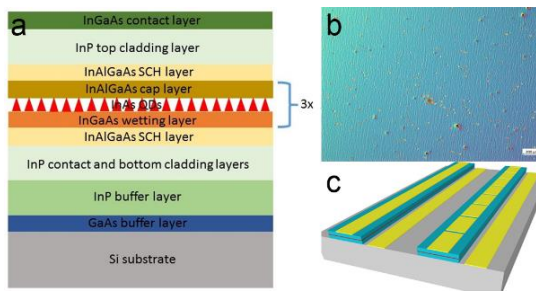


**Figure 1:** (a) Epitaxial structure of 1.55  $\mu\text{m}$  InAs QD laser growth on Si. (b) Wafer surface imaged in differential interference contrast mode (Si substrate). (c) Schematic diagram of broad-area lasers and segmented contact devices.

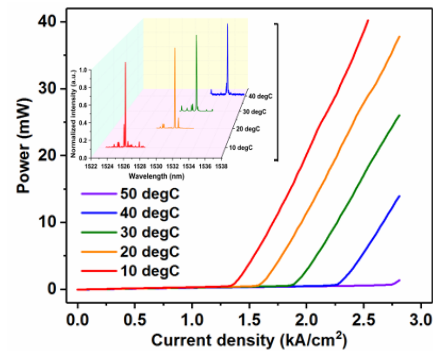


**Figure 2:** Power-Current curves of a 2.1 mm cavity length stripe laser measured at temperatures between 10  $^{\circ}\text{C}$  and 50  $^{\circ}\text{C}$ . Also shown (inset) is the lasing spectra between 10  $^{\circ}\text{C}$  and 40  $^{\circ}\text{C}$  exhibiting a red shift from 1526 nm to 1536 nm.

form top and bottom contact respectively. For the segmented contact devices each contact was defined to be  $292 \mu\text{m}$  in length with  $8 \mu\text{m}$  intercontact spacing. Lasing and non-lasing segmented contact devices with cleaved, uncoated facets were mounted on TO headers and wire-bonded.

### 3. Results and Discussion

Broad-area stripe lasers with a cavity length of  $2.1 \text{ mm}$  were driven using a pulsed current source with a  $1 \mu\text{s}$  pulse duration and a repetition rate of  $5 \text{ kHz}$  to avoid self-heating. The average power emission from a single facet was measured and converted to peak average power, accounting for emission from both facets of the device (Figure 2). Increasing the temperature from  $10^\circ\text{C}$  to  $50^\circ\text{C}$  increased the threshold current density from  $1.36 \text{ kA cm}^{-2}$  to  $2.8 \text{ kA cm}^{-2}$ . The lasing wavelength was measured at  $\approx 10\%$  above the device threshold current at each temperature (Figure 2, inset). The lasing wavelength peak exhibited  $\approx 10 \text{ nm}$  redshift from  $1525.3 \text{ nm}$  to  $1535.3 \text{ nm}$  due to the increase in temperature, whilst the laser linewidth broadened from  $7.1 \text{ GHz}$  to  $11.1 \text{ GHz}$ . To better understand the optical properties of the material, and directly compare to a nominally identical laser structure grown on a native InP substrate, the optical gain and absorption of each wafer was measured using the segmented contact method [7] at  $20^\circ\text{C}$  and  $40^\circ\text{C}$ . Figure 3 shows the optical gain and absorption spectra for the Si substrate sample as a function of injection current density, with a maximum measured net gain of  $\approx 14 \text{ cm}^{-1}$  at a current density of  $2.67 \text{ kA cm}^{-2}$ . A large internal optical loss,  $\alpha_i \approx 20 \text{ cm}^{-1}$  at  $20^\circ\text{C}$  was measured at longer wavelengths and a similar value was recorded for the sample grown in InP. Increasing the sample temperature to  $40^\circ\text{C}$  resulted in a significant increase in the value of  $\alpha_i$  for both samples, resulting in a decrease in the peak net gain (Figure 4), and thus the large increase in threshold current density with temperature observed in Figure 2. It should be noted that the similarities between the peak net gain against current density (Figure 4) for each sample indicate that the high threshold current densities observed in both is therefore likely due to the laser structure design, rather than any defects introduced due to the growth on Si substrate.

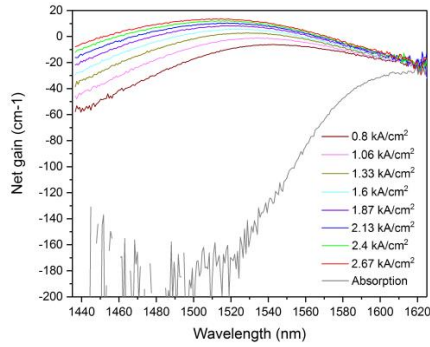


**Figure 3:** Optical gain and absorption spectra at  $20^\circ\text{C}$  for the laser structure grown on Si substrate.

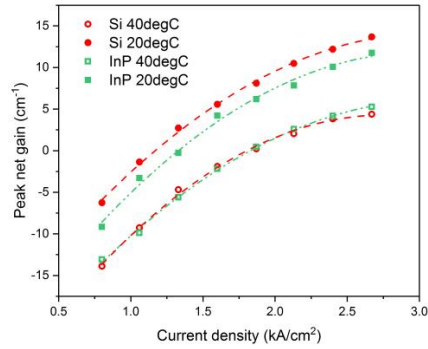


**Figure 4:** Peak net gain against current density for the laser structures grown on Si and InP substrates at  $20^\circ\text{C}$  and  $40^\circ\text{C}$ . Fits to the curves are shown as dashed/dot-dashed lines.

### 4. Conclusion

We present the first report of optical gain and absorption measurements of  $1.55 \mu\text{m}$  InAs QD laser structures grown on silicon (001) substrates. A comparison of the laser, optical gain and absorption characteristics to a nominally identical structure grown on a native InP substrate indicates the device performance is currently limited by the laser active structure design, rather than the introduction of defects due to growth on the silicon substrate. This research is supported by the UK Engineering Physical Sciences Research Council (EPSRC) under grant number EP/P006973/1.

### 5. References

- [1] A. Y. Liu, C. Zhang, J. Norman, A. Snyder, D. Lubyshev, J. M. Fastenau, A. W. K. Liu, A. C. Gossard and J. E. Bowers, "High performance continuous wave  $1.3 \mu\text{m}$  quantum dot lasers on silicon," *Applied Physics Letters*, vol. 104, p. 041104, (2014).
- [2] S. Chen, W. Li, J. Wu, M. Tang, S. Shutts, S. N. Elliott, A. Sobiesierski, A. J. Seeds, I. Ross, P. M. Smowton and H. Liu, "Electrically pumped continuous-wave III-V quantum dot lasers on silicon," *Nature Photonics*, vol. 10, p. 307, (2016).
- [3] B. Shi, S. Zhu, Q. Li, C. W. Tang, Y. Wan, E. L. Hu and K. M. Lau, " $1.55 \mu\text{m}$  room-temperature lasing from subwavelength quantum-dot microdisks directly grown on (001) Si," *Applied Physics Letters*, vol. 110, p. 121109, (2017).
- [4] S. Zhu, B. Shi, Q. Li and a. K. M. Lau, " $1.5 \mu\text{m}$  quantum-dot diode lasers directly grown on CMOS-standard (001) silicon," *Applied Physics Letters*, vol. 113, p. 221103, (2018).
- [5] Q. Li and K. M. Lau, "Epitaxial growth of highly mismatched III-V materials on (001) silicon for electronics and optoelectronics," *Progress in Crystal Growth and Characterization of Materials*, vol. 63, no. 4, pp. 105-120, (2017).
- [6] Z. Li, M. Wang, X. Fang, Y. Li, X. Zhou, H. Yu, P. Wang, W. Wang and J. Pan, "Monolithic integration of InGaAs/InP multiple quantum wells on SOI substrates for photonic devices," *Journal of Applied Physics*, vol. 123, p. 053102, 2018.
- [7] P. Blood, G. M. Lewis, P. M. Smowton, H. Summers, J. Thomson and J. Lutti, "Characterization of semiconductor laser gain media by the segmented contact method," *IEEE Journal of Selected Topics in Quantum Electronics*, vol. 9, pp. 1275-1282, (2003).

# Effects of power-split ratio and phase delay on performance of self-mode-locked QDash lasers subject to asymmetric dual-loop optical feedback

Haroon Asghar,<sup>1,2,\*</sup> Ehsan Sooudi,<sup>3</sup> and John Gerard McInerney<sup>3,4</sup>

<sup>1</sup>Atomic and Molecular Physics Laboratory, Quaid-i-Azam University, 45320 Islamabad, Pakistan

<sup>2</sup>National Center for Physics, Quaid-i-Azam University Campus, Islamabad 45320, Pakistan

<sup>3</sup>Department of Physics and Tyndall National Institute, University College Cork, Western Road, Cork T12 YN60, Ireland

<sup>4</sup>College of Optical Sciences, University of Arizona, Tucson AZ 85721, USA

\*Corresponding author: haroon.asghar92@gmail.com

**Abstract:** We demonstrate an asymmetric dual-loop, with inner cavity resonant and fine delay tuning of outer loop, gives the narrowest RF linewidth over wide range of delay. Under such conditions, symmetric dual-loops narrows the RF by ~4-84x, across the widest delay, compared to free-running.

## 1. Introduction

Semiconductor mode-locked quantum Dot/Dash/Well lasers with low timing jitter and high repetition rates are promising candidates for applications in coherent Tb/s optical communications [1]. In time critical applications, stabilization of semiconductor MLLs is highly desirable, as generation of optical pulses plays a crucial role in determining MLLs performance. A series of experimental studies [2-5] have been performed to improve timing jitter of self-mode-locked (SML) two-section quantum-dash (QDash) lasers using dual-loops optical feedback. In this work, we experimentally investigated the RF linewidth stabilization as a function of delay subject to power-split ratio and separate fine-tuning of dual optical delay phase based asymmetric (unequal arms of external loops) dual-loop optical feedback schemes.

## 2. Experimental setup and results

Devices under investigation are two-section InAs/InP quantum-dash self-mode-locked lasers (QDash MLL) with active layers composed of nine InAs quantum-dash monolayers grown by gas source molecular beam epitaxy, embedded within two barriers and separate confinement heterostructure (SCH) layers (dash-in-barrier structure) [6] emitting at ~ 1550 nm. The experimental setup is shown and discussed in [2].

We conducted an experimental analysis to improve timing stability of our SML QDash lasers using dual-loop optical feedback versus parameters including power-split ratio and separate fine-tuning of optical delay phase attached with both feedback loops (ODL-I and ODL-II). Two combinations of feedback ratios investigated in this study are presented in Table. 1.

**Table. 1:** Two chosen combinations of feedback ratio through either feedback loop or overall feedback strength into gain section

Loop-I	Loop-II	Minimum RF	Maximum RF
-23.29 dB(c)	-28.06 dB	1.3 kHz	94 kHz
-23.29 dB	-28.06 dB(c)	1.4 kHz	26 kHz

### I. RF linewidth versus full phase delay with the weaker cavity (ODL-II) set to an integer resonance, then fine-tune the stronger cavity (ODL-I (c))

In the following, we observed the variation in RF linewidth versus delay with different percentage of power-split ratio through two external feedback cavities based on asymmetric dual-loop optical feedback. In asymmetric dual-loop feedback, simultaneous optical feedback from two external cavities are applied to the gain section at -22 dB. The optical delay (ODL-II) was adjusted to full resonance and the length of optical delay line (ODL-I) was tuned from 0-84 ps, the maximum range available. In addition, feedback ratio through Loop-I and Loop-II was fixed to -23.29 and -28.06 dB using variable optical attenuators (Att-I and Att-II), respectively. The RF linewidth versus delay is shown in Fig. 1(a) (blue triangles). These results demonstrates that RF linewidth versus delay yields severe instabilities on widest range of delay tuning, when weaker cavity (ODL-II) set to an integer resonance then fine-tune the stronger cavity (ODL-I(c)). When both feedback cavities were fully resonant, the RF linewidth narrowing to as low as 1.3 kHz was noted.

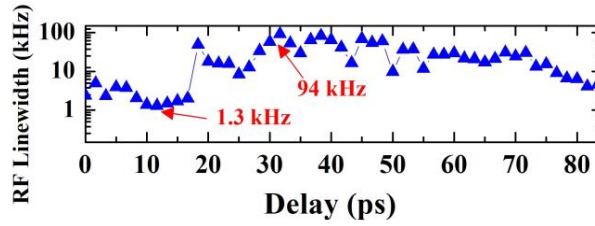


Fig. 1. Measured RF linewidth versus delay using asymmetric dual-loop optical feedback versus full phase delay with the weaker cavity (ODL-II) set to an integer resonance then fine-tune the stronger cavity (ODL-I (c)) subject to following feedback ratio through Loop-I(c):-23.29 dB and Loop-II: -28.06 dB

## II. RF linewidth versus full phase delay with stronger cavity (ODL-I) set to an integer resonance then fine-tune the weaker cavity (ODL-II (c))

For next combination of power-split, when phase delay attached with a strong cavity (ODL-I=-23.29 dB) is set to integer resonance then fine-tunes the weaker cavity (ODL-II (c)=-28.06 dB). This study revealed that optimized asymmetric dual-loop feedback extends the effective resonant feedback regime and maintains stable RF spectra, with narrow RF linewidth across the entire accessible delay range (shown in Fig. 2). Furthermore, under fully resonant conditions, RF linewidth narrows from 100 kHz free-running to 1.2 kHz for asymmetric dual-loops feedback.

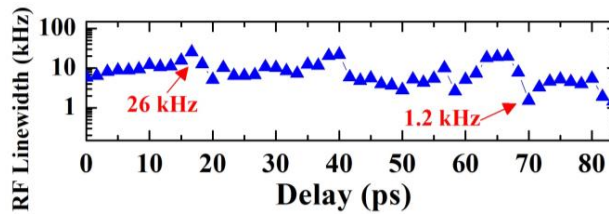


Fig. 2. Measured RF linewidth versus delay using asymmetric dual-loop optical feedback with stronger cavity (ODL-I) set to an integer resonance, then fine-tuning the weaker cavity (ODLII(c)) subject to following feedback ratio through Loop-I:-23.29 dB and Loop-II(c):-28.06 dB

## 3. Conclusion

These results demonstrates that different power-split ratio has significant influence on the RF linewidth of our SML QDash laser subject to symmetric and asymmetric dual-loops at integer resonance as well as on widest range of delay tuning. In addition, these measurements further reveals that stabilization of SML QDash lasers can be improved by controlling the parameters such as power-split ratio and optical delay phase tuning using symmetric and asymmetric dual-loop optical feedback. A study of feedback ratio controlled dual-loop feedback scheme further suggests that dual-loop optical feedback can be implemented for greater stabilization and improvement of ultrashort optical pulse dynamics.

## 4. Acknowledgment

The authors gratefully acknowledge financial support from Science Foundation Ireland (grant 12/IP/1658) and the European Office of Aerospace Research and Development (grant FA9550-14-1-0204).

## 5. References

- [1] A. Anthur, V. Panapakkam, R. Zhou, Q. Gaimard, K. Merghem, F. Lelarge, A. Ramdane, L. P. Barry, "Tbit/s optical interconnects based on low linewidth quantum-dash lasers and coherent detection," Conference on Lasers and Electro-Optics (CLEO), San Jose, CA, 1-2, (2016).
- [2] F. Lelarge, et al., "Recent advances on InAs/InP quantum dash based semiconductor lasers and optical amplifiers operating at 1.55 $\mu\text{m}$ ," IEEE J. Sel. Topics Quantum Electron., vol. 13, no. 1, pp. 111–124 (2007).
- [3] H. Asghar, W. Wei, P. Kumar, E. Sooudi, and J. G. McInerney, "Stabilization of self-mode-locked quantum dash lasers using symmetric dual optical feedback," Opt. Express., vol. 26, pp. 4581–4592 (2018).
- [4] H. Asghar, E. Sooudi, P. Kumar, W. Wei, and J. G. McInerney, "Optimum stabilization of self-mode-locked quantum dash lasers using dual optical feedback with improved tolerance against phase delay mismatch," Opt. Express., vol. 25, pp. 15796–15805 (2017).
- [5] H. Asghar and J. G. McInerney, "Asymmetric dual-loop feedback to suppress spurious tones and reduce timing jitter in self-mode-locked quantum dash lasers emitting at 1.55  $\mu\text{m}$ ," Opt. Lett. vol. 42, pp. 3714–3717 (2017).
- [6] H. Asghar, E. Sooudi, and J. G. McInerney, "Stabilization of self-mode-locked QDash lasers subject to simultaneous continuous-wave optical injection and optical feedback," Appl. Opt. vol. 57, pp. E45-E49 (2018).

# Photonic integrated circuit extended cavity passively mode-locked symmetric ring laser with dual absorber

D. Auth,<sup>1\*</sup> M.-C. Lo,<sup>2,3</sup> C. Weber,<sup>1</sup> P. Fiala,<sup>1</sup> P. Sauer,<sup>1</sup> G. Carpintero,<sup>2</sup> and S. Breuer<sup>1</sup>

<sup>1</sup> Institute of Applied Physics, Technische Universität Darmstadt, Schlossgartenstraße 7, 64289 Darmstadt, Germany

<sup>2</sup> Universidad Carlos III de Madrid, Av de la Universidad, 30. 28911 Leganés, Madrid, Spain

<sup>3</sup> University College London, London WC1E 7JE, UK

\*dominik.auth@physik.tu-darmstadt.de

**Abstract:** A photonic integrated circuit extended cavity passively mode-locked semiconductor ring laser with two saturable absorbers in a symmetric ring geometry fabricated using an InP generic integration technology platform is presented. The laser emits 1.4 ps short optical pulses with a time-bandwidth-product of 0.96 (Gaussian shaped pulses) at a fundamental repetition rate of 23.3 GHz. The laser exhibits a repetition rate line width of 80 kHz, corresponding to a pulse-to-pulse timing jitter of 31.7 fs. The emission is centered at 1570 nm and the maximum spectral bandwidth amounts to 10.2 nm (-3 dB) and 19.7 nm (-20 dB).

## 1. Introduction

Monolithic passively mode-locked semiconductor lasers are promising compact sources for generating coherent optical frequency combs and trains of ultra-short optical pulses for metrology, spectroscopy and millimeter wave/terahertz applications [1]. Compared to their Fabry–Pérot counterparts [2], mode-locked semiconductor ring lasers feature the intrinsic mirror symmetry with respect to the central saturable absorber and therefore allow for colliding-pulse mode-locking [3, 4]. By doubling the pulse-narrowing effect, colliding-pulse mode-locking is expected to decrease the pulse width and improve the pulse train stability [5, 6]. Recently, a passively mode-locked InP quantum well ring laser with a symmetric ring colliding-pulse mode-locking geometry on a photonic integrated circuit with 3 mm length and a single 40  $\mu\text{m}$  long absorber emitting at 1565 nm generated 1.9 ps short optical pulses at a repetition rate of 12 GHz with a repetition rate line width of 390 kHz (-10 dB), a repetition rate peak signal-to-noise ratio > 50 dB and spectral widths exceeding 40 nm (-20 dB), has been demonstrated [4].

In this contribution, we report the realization and experimental investigation of a semiconductor ring laser with extended cavity symmetric ring colliding-pulse mode-locking geometry employing two absorber sections and four gain sections, fabricated using an InP active-passive generic integration technology platform.

## 2. Photonic integrated circuit laser design & experimental set-up

The cavity design is point symmetric and schematically depicted in Fig. 1. It comprises four 300  $\mu\text{m}$  long semiconductor optical amplifiers (SOAs), two 30  $\mu\text{m}$  long saturable absorbers (SAs) and four electro-optic phase modulators (EOPMs). Both SOA and SA sections use the same active layer stack, based on InGaAsP/InP quantum well gain media. The passive straight and curved waveguides form the circulating extended cavity. Two 2x2 multimode interference (MMI) couplers provide the optical output from the cavity in both, clockwise (CW) and counter-clockwise (CCW), propagation directions through the output waveguides 1-4 at the anti-reflection coated emission facet at the right-hand side. The ring cavity length amounts to  $\approx 3.5$  mm, corresponding to a repetition rate of 23 GHz (refractive index of 3.7). The laser was fabricated within a multi-project wafer run through the Jeppix foundry coordinator at SMART Photonics with a predefined layer stack [7].

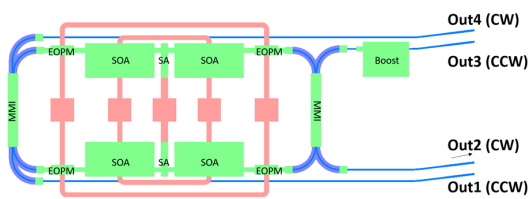


**Figure 1:** Sketch of the developed photonic integrated circuit laser design. Blue: Passive straight and curved waveguides. Green: Active components such as semiconductor optical amplifier (SOA)-based gain sections, absorber sections (SAs), booster amplifier (Boost), and phase modulators (EOPMs), and passive components such as multimode interference (MMI) couplers. Red: Metal routing.

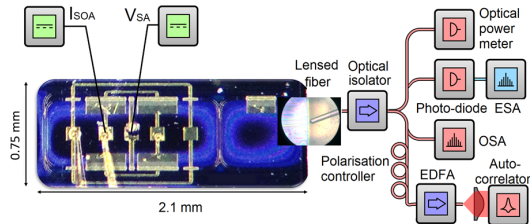


**Figure 2:** Optical microscope picture with dimensions and sketch of the experimental set-up. Two DC input signals ( $I_{\text{SOA}}$  and  $V_{\text{SA}}$ ) bias the active sections. Laser emission is in part amplified by an erbium-doped fiber amplifier (EDFA) and studied by the measurement instruments: electrical spectrum analyzer (ESA), optical spectrum analyzer (OSA), intensity auto-correlator.

The laser is biased through direct probing the metal contact pads with DC needles by an external low-noise DC current source and a DC voltage supply and is placed on a copper carrier which is temperature stabilized at 20°C. In the experiment, the light emitted from optical outputs Out 1 and Out 4 at the facet are coupled into a lensed fiber as shown in Fig. 2. Analysis of the laser emission is performed by an optical power meter and an optical spectrum analyzer (OSA) (spectral resolution 10 pm). The repetition rates and repetition rate line widths in the pulsed regime are analyzed with a high-speed photodiode (electrical bandwidth 45 GHz) followed by an electrical spectrum analyzer (ESA) (electrical bandwidth 50 GHz). After amplification by an extended C-band erbium-doped fiber amplifier (EDFA) and a polarization controller, the depicted pulses are characterized by a nonlinear intensity auto-correlator (AC).

### 3. Results and discussion

The light emission characteristics of the laser is investigated for reverse biases of  $V_{SA} = 0$  V up to  $V_{SA} = 3.1$  V for both propagating directions (CCW Out 1 and CW Out 4). The gain section injection current  $I_{SOA}$  is varied from 0 mA to 255 mA. The results for CCW and CW propagation indicate a threshold current of 55 mA at  $V_{SA} = 0$  V, which increases with increasing absorber reverse bias voltage up to 75 mA for  $V_{SA} = 3.1$  V. The highest fiber-coupled power (coupling efficiency  $\sim 30\%$ ) exceeds 0.5 mW for  $V_{SA} = 0$  V for the CW and CCW direction. For higher absorber reverse bias voltages optical powers up to 0.2 mW ( $V_{SA} = 2$  V) and 0.18 mW ( $V_{SA} = 3$  V) are coupled into the fiber. A passive mode-locking operation regime is obtained for gain injection currents above 130 mA and absorber reverse bias voltages above 2 V. In this regime radio-frequency (RF) signal-to-noise ratios for the repetition rate line between 20 dB and 30 dB are obtained. For all investigated biasing conditions in this regime, auto-correlation time traces indicate optical pulses that can be well fitted by well-matching Gaussian functions. Recorded pulse widths are well below 2.8 ps. In general, broader pulses are measured for lower reverse bias voltages, due to the weaker pulse shortening effect of the absorber, and for higher injection currents, as the absorber stronger saturates and low intensity parts of the pulse become less absorbed. For  $I_{SOA} = 150$  mA and  $V_{SA} = 3.1$  V, a repetition rate line width of 80 kHz (-3 dB, Lorentzian fit) corresponding to a pulse-to-pulse timing jitter ( $TJ_{pp}$ ) of 31.7 fs [8] at a repetition rate of 23.3 GHz is identified with a signal-to-noise ratio of 30 dB, shown in Fig. 4(a). A zoom into the repetition rate line depicts the Lorentzian fit (Fig. 4(b)). The shortest pulse width amounts to 1.41 ps and is obtained at  $I_{SOA} = 150$  mA and  $V_{SA} = 3.1$  V and is depicted in Fig. 4(c) accompanied by the lowest time-bandwidth-product of 0.96. This value indicates a small amount of chirp within the optical pulse. The broadest obtained optical spectrum is centered at 1575 nm with a bandwidth of 10.2 nm (-3 dB) and 19.7 nm (-20 dB) as shown in Fig. 4(d). About 52 modes are spaced equally by 0.19 nm within the -3 dB spectral bandwidth and 102 modes within the -20 dB bandwidth.

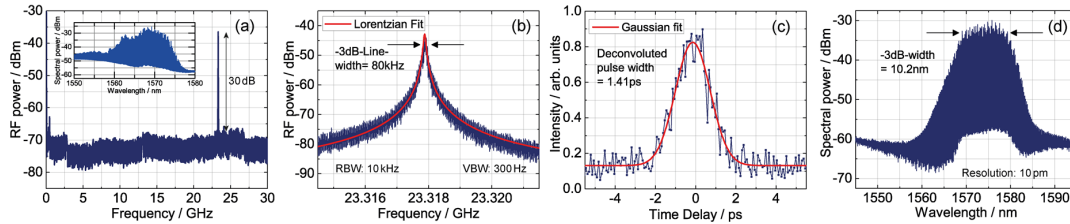


**Figure 3:** (a) Full-span RF spectrum for  $I_{SOA} = 150$  mA,  $V_{SA} = 3.1$  V. The inset shows the optical spectrum for the same bias conditions. (b) Zoom into (a) and Lorentzian fit. (c) Auto-correlation trace at  $I_{SOA} = 150$  mA and  $V_{SA} = 3.1$  V showing the shortest optical pulses obtained by this device. Scan range: 10 ps. (d) Optical spectrum at  $I_{SOA} = 215$  mA,  $V_{SA} = 2.0$  V showing the broadest optical comb obtained for this device.

### 4. Conclusion

In conclusion, we designed and experimentally studied a photonic integrated circuit mode-locked extended cavity ring laser with two absorbers in a point symmetric geometry, manufactured in an InP-based generic foundry. Phase-locked 10.3 nm broad optical spectra have been generated at a repetition rate of 23.3 GHz. The minimum repetition rate line width of 80 kHz corresponds to a pulse-to-pulse timing jitter of 31.7 fs. The shortest optical pulses were 1.4 ps accompanied by the lowest time-bandwidth-product of 0.96.

### 5. References

- [1] M. L. Davenport, S. Liu, and J. E. Bowers, *Photonics Research* **6**, 468 (2018)
- [2] M.-C. Lo, R. Guzmán, and G. Carpintero, *Optics Express* **26**, 18386 (2018)
- [3] J. P. Hohimer and G. A. Vawter, *Applied Physics Letters* **63**, 1598 (1993)
- [4] V. Moskalenko, J. Koelemeij, K. Williams, and E. Bente, *Optics Letters* **42**, 1428 (2017)
- [5] S. Yu, T. F. Krauss, and P. J. Laybourn, *Optical Engineering* **37**, 1164 (1998)
- [6] Y. Barbarin, E. A. J. M. Bente, M. J. R. Heck, Y. S. Oei, R. Nötzel, and M. K. Smit, *Optics Express* **14**, 9716 (2006)
- [7] K. Williams, E. Bente, D. Heiss, Y. Jiao, K. Ławniczuk, X. Leijens, J. van der Tol, and M. Smit, *Photonics Research* **3**, B60 (2015)
- [8] F. Kéfélian, S. O'Donoghue, M. T. Todaro, J. G. McInerney, and G. Huyet, *IEEE Photonics Technology Letters* **20**, 1405 (2008)

# Self-consistent thermal-opto-electronic model for the dynamics in high-power semiconductor lasers

U. Bandelow<sup>1\*</sup>, M. Radziunas<sup>1</sup>, J. Fuhrmann<sup>1</sup>, A. Zeghuzi<sup>2</sup>, H.-J. Wünsche<sup>1,2</sup>, and H. Wenzel<sup>2</sup>

*Weierstrass Institute (WIAS), Mohrenstrasse 39, 10117 Berlin, Germany.*

*Ferdinand-Braun-Institut, Leibniz Institut für Höchstfrequenztechnik, Gustav-Kirchhoff-Str. 4, 12489 Berlin, Germany.*

*\*Uwe.bandelow@wias-berlin.de*

**Abstract:** We present a model for the dynamics of high-power broad-area edge-emitting diode lasers that self-consistently couples heat transport (HT) to a dynamic electro-optical (EO) model for the active region. Due to the different time scales, we propose an iterative coupling scheme. The HT-solver calculates temperature- and thermally-induced refractive index distributions. The EO-solver exploits these distributions and provides field intensities, quasi-Fermi potentials, carrier densities, and bias current. Using these distributions for calculation of the heat sources that enter the HT-solver repeatedly, heating effects can be efficiently simulated.

## 1. Introduction

Due to their small size and high efficiency high-power broad-area semiconductor lasers (BALs), see Fig. 1(a), are important sources for high-performance laser systems. Single devices can emit tens of watts output, thereby generating large amounts of heat, which has significant impact on the laser operation. The most prominent effect is the formation of a self-heating-induced waveguide, which plays a crucial role for the emission characteristics. We calculate this by coupling a static heat transport (HT) model and a dynamic electro-optical (EO) model [1].

## 2. Electro-optical model

For the spatiotemporal dynamics in BALs, we use a 2+1 dimensional traveling wave (TW) model [1], that takes into account the optical field and the carrier dynamics within the quantum-well active zone of the laser, see Fig. 1(b). A set of effective model parameters represents the influence of the vertical device structure. The TW equations [1] account for the refractive index profile given by the device structure (etched trenches), absorption [2], material gain, and the induced refractive index. The latter depend on the local carrier density. Nonlinear gain compression [2] and dispersion are included as well as a thermally-induced contribution  $n_T$  to the index profile [5]. The dynamics of the carrier density within the (undoped) active region is described by a diffusion equation. These model equations can be numerically solved by the EO-solver BALaser [3] developed at WIAS. In a basic form this electro-optical model has been successfully applied for the simulation of Master-Oscillators coupled to Power Amplifiers (MOPA), where a significant impact of residual reflectivities on the dynamics of the optical field could be shown [6],[7]. For a more realistic description of carrier diffusion and injected current density within the active zone, we simultaneously include the carrier spreading problem by solving a Laplace equation for the quasi-Fermi potential of the holes in the p-doped region of the transverse cross-sections (black-framed region in Fig. 1(c)) [2],[4].

## 3. Thermal model and coupling of EO- and HT models

We take into account heating and its spreading along the device. Due to the strongly differing time scales and limited computing resources, we introduce two approximations. First, since characteristic distances differ by an order of magnitude, we neglect heat diffusion in  $z$  direction. This allows a reduction to a set of (2+1)-dimensional heat transport equations. Our second simplification is motivated by the huge difference in the time scales of optoelectronic and thermal processes: We ignore the temperature evolution within (several ns long) transients and exploit the time-averaged temperature instead, where the time-averaged heat source  $h$  generated by the previous transient EO simulation enters. For the numerical solution, we use the toolkit `pdelib` [8] developed at WIAS. Typical calculated heat distributions of a BAL emitting 13 W power are shown in Fig. 2(a). The EO- and HT-solvers are self-consistently coupled using an iterative procedure. From initial transient calculations ( $\geq 5$  ns) with the dynamic EO-solver, time-averaged distributions are obtained, that are used for construction of the (time-averaged) heat source. Finally, with that heat source the static HT-problem is solved. From the resulting temperature profile the thermally induced index distribution  $n_T$  is calculated, which is needed to proceed to the first step of this iterative procedure. Panels (b)-(d) of Fig. 2 illustrate how this iterative procedure works. Initially the temperature was fixed by the heat sink, resulting in the upper black curves in Fig. 2(b,c), showing a

relatively small far-field divergence (panel (c)). Panel (d) shows how the initial correction enhances the profile of  $n_T$ , resulting in further changes of near- and far-fields. These distributions converge after approximately seven iterations. Results on thermal lensing have been published recently [1] in comparison with experimental data.

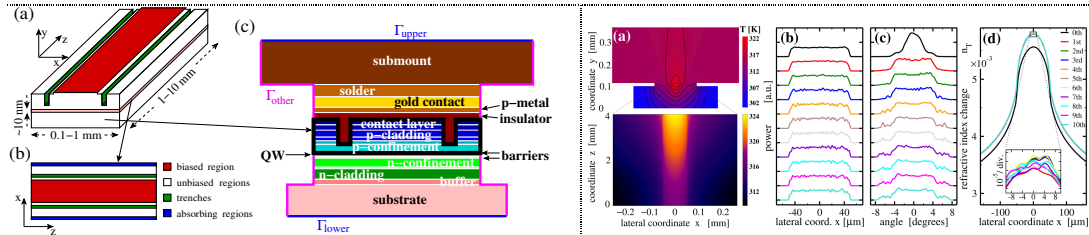


**Figure 1:** Schematic representation of an edge-emitting broad-area laser (a), top view on its active zone where the TW model is defined (b), and the transverse cross-section (c), where the thermal equations and the carrier flow equations (black-framed region) are solved.

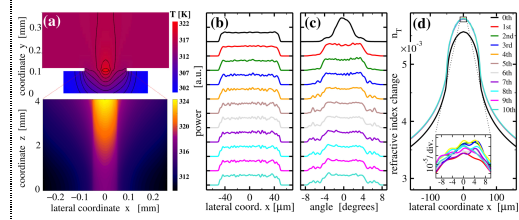


**Figure 2:** Simulation of a BAL with 13 W emission power (a): temperature distribution along a transverse cross-section (top) and the active layer (bottom). (b), (c), and (d) evolution of the time-averaged near-fields, far-fields, and thermally-induced refractive index change profiles at the front facet during the iterations. Initial step : solid black.

#### 4. Conclusion

We discussed an efficient inclusion of a heat transport model into a dynamic electro-optical model for BALs, that allows for a self-consistent estimation of heating effects, which is crucial for their emission characteristics.

#### 5. Acknowledgements

This work is supported by the German Federal Ministry of Education and Research contract 13N14005 as part of the EffiLAS/HotLas project and by the EUROSTARS Project E!10524 HIP-Lasers. U.B. acknowledges support by the Deutsche Forschungsgemeinschaft in the CRC 787 *Semiconductor Nanophotonics* (grant B4).

#### 6. References

- [1] A. Zeghuzi et al. “Time-dependent simulation of thermal lensing in high-power broad-area semiconductor lasers,” *IEEE J. Select. Topics Quantum Electron.*, vol. 25, no. 6, p. 1502310, 2019.
- [2] A. Zeghuzi et al. “Influence of nonlinear effects on the characteristics of pulsed high-power broad-area distributed Bragg reflector lasers,” *Opt. and Quantum Electron.*, vol. 50, p. 88, 2018.
- [3] BALaser, “A software tool for simulation of dynamics in broad area semiconductor lasers. <http://www.wias-berlin.de/software/balaser/>.”
- [4] M. Radziunas et al. “Efficient coupling of the inhomogeneous current spreading model to the dynamic electro-optical solver for broad-area edge-emitting semiconductor devices,” *Opt. Quantum Electron.*, vol. 49, no. 10, pp. 1–8, 2017.
- [5] S. Rauch et al. “Impact of longitudinal refractive index change on the near-field width of high-power broad-area diode lasers,” *Appl. Phys. Lett.*, vol. 110, no. 26, p. 263504, 2017.
- [6] M. Spremann et al. “Measurement and simulation of distributed-feedback tapered master-oscillators power-amplifiers,” *IEEE J. Quantum Electron.*, vol. 45, no. 6, pp. 609–616, 2009.
- [7] M. Radziunas et al. “Mode transitions in distributed-feedback tapered master-oscillator power-amplifier: theory and experiments,” *Opt. Quantum Electron.*, vol. 40, pp. 1103–1109, 2009.
- [8] J. Fuhrmann and T. Streckenbach, “pdelib: A finite volume and finite element method for PDEs. <http://pdelib.org>.”

# InP based integrated tunable laser systems for optical coherence tomography and strain sensing

E. Bente<sup>1\*</sup>, S. Andreou<sup>1</sup>, R. Pajković<sup>1</sup>, J. Hazan<sup>1</sup>, K. Williams<sup>1</sup>

<sup>1</sup>Photonic Integration Group, Electrical Engineering Department, Eindhoven University of Technology, P.O. Box 513,

5600MB Eindhoven, Netherlands

\*e.a.j.m.bente@tue.nl

**Abstract:** Photonic integration technology on InP allows for the realization of tunable laser for a number of applications. In particular this is enabled by the availability of voltage controlled phase modulators in InP based technology. In this paper we will discuss tunable integrated semiconductor laser systems for two applications, optical coherence tomography and strain sensing, where the use of these modulators plays an important role.

## 1 Introduction

Tunable lasers operating around 1550 nm and 1300 nm are of interest to tele- and data-communication as well as other applications. For each application, specific performance parameters are required which can vary significantly and which make that specific laser circuits need to be designed for each application. Lasers meeting widely varying requirements can be realised using a single photonics integration technology platform. Photonic integration technology on Indium Phosphide allows for the monolithic integration of amplifiers, passive waveguide structures and electro-optic phase modulators. Thus such a technology which is now commercially available [1], has important advantages. A particular advantage of this InP platform is the availability of voltage controlled phase modulators which can have an electronic bandwidth of several GHz and which consume and dissipate much less power than current-injection based devices [2], [3]. These phase modulators enable the realisation of intra-cavity control elements, i.e. tunable filters. Such filters offer the prospect of having minimal thermal effects which minimises their settling time to the order of a nanosecond or even less. The tuning properties of a laser will thus become much less dependent on tuning speed. In this paper we will present lasers and their design and operating consideration for two applications. The first concerns a tunable laser for optical coherence tomography. The second application concerns actively stabilized tunable lasers for application in strain sensors based on  $\pi$ -shifted fibre Bragg gratings. In this application the use of voltage controlled phase modulators has two advantages. Firstly it avoids the increase in noise associated with the introduction of tunable devices based on current injection (e.g. in distributed Bragg gratings). Secondly the effects of heating which affects the refractive index in the waveguide in the opposite direction are avoided.

## 2. Widely tunable laser for optical coherence tomography

Scanning Source Optical Coherence Tomography (SS-OCT) is an imaging modality which requires a fast scanning laser source. We are working on a semiconductor laser system that can be suitable for SS-OCT. It is a further development of a tunable laser based on a ring cavity containing an SOA, output coupler and three asymmetric Mach-Zehnder interferometers (AMZI) in series to control the lasing wavelength and make the laser operate in a single longitudinal mode [4]. The goal is to have the laser make anywhere from a few hundred up to a few thousand scan-steps over its tuning range which can be over 70 nm in the 1500 nm range. The voltage controlled phase modulators in the AMZIs enable a fast switching between the settings of the filters. In this paper some modelling of the laser results and experiments related to wavelength switching will be presented. The lasers show switching speeds between two wavelengths can vary quite widely to over 100ns. An example of calculated wavelength switching behavior is presented in Figure 1. The results show that efficient suppression of the initial wavelength after the switching of the filter plays an important role. Further issues with cross-talk between different phase modulators, light intensity dependent dark current in the phase modulator [5] and options for realizing such a laser in the 1300 nm wavelength range are discussed.

## 3. Stabilized tunable lasers for fiber strain sensing

Fiber Bragg gratings with a  $\pi$  phase in the middle have a reflection spectrum that consists of a band that has a width that is of the order of a nanometer, with a narrow spectral dip in the middle that is 40 – 100 MHz wide depending on the design. The optical frequency of this spectral dip changes with strain and temperature on the fiber. Small changes in strain and temperature changes can be observed when monitoring this optical frequency by locking a tunable laser to this resonance and measuring the laser output frequency. This laser frequency measurement can be done (down to the level of tens of kHz) by beating the laser output with another laser locked to a reference cavity. In this paper we present a number of results of frequency locking of integrated semiconductor lasers using feedback on an intra-cavity phase modulator acting as a frequency control port. This

circumvents a common complication of applying electrical feedback to a laser using current into an optical amplifier where thermal effects and carrier density effects determine the laser frequency but with opposite effect. We have successfully stabilized integrated tunable lasers [6], demonstrating linewidths down to 1 kHz using measurement of the power spectral density of the frequency noise as well as self-heterodyne measurements. An example of a 5 kHz linewidth measurement from a DBR laser with an additional intra-cavity ring resonator filter is presented in Figure 2.

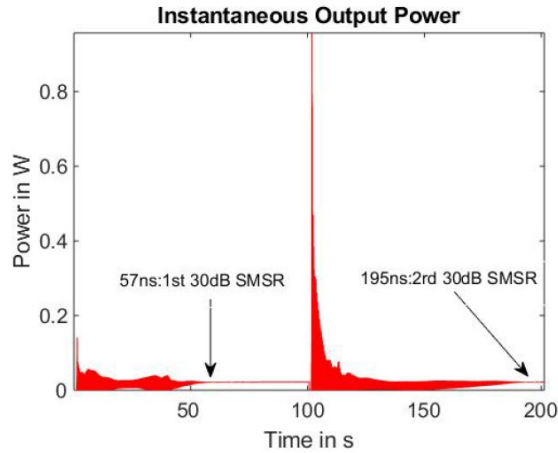


**Figure 1:** Calculated output of a tunable laser being switched on and then switched at  $t = 100$  ns from 1501.12 nm to 1532.25 nm. The time at which 30dB SMSR is achieved is indicated.

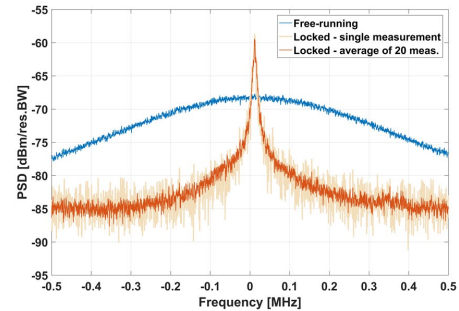


**Figure 2:** Traces from a self-heterodyne measurement of the output of a DBR laser with intra-cavity ring filter [7]: free running (blue curve) and stabilized to a reference etalon (red and orange curves). The 3dB linewidth is 5 kHz.

#### 4. References

- [1] L. M. Augustin *et al.*, "InP-Based Generic Foundry Platform for Photonic Integrated Circuits," *IEEE J. Sel. Top. Quantum Electron.*, vol. 24, no. 1, pp. 1–10, Jan. 2018.
- [2] W. Yao, *Towards a high-capacity multi-channel transmitter in generic photonic integration technology*. Technische Universiteit Eindhoven, 2017.
- [3] S. Andreou, K. A. Williams, and E. A. J. M. Bente, "Steady-State Analysis of the Effects of Residual Amplitude Modulation of InP-Based Integrated Phase Modulators in Pound–Drever–Hall Frequency Stabilization," *IEEE Photonics J.*, vol. 11, no. 3, pp. 1–14, Jun. 2019.
- [4] S. Latkowski *et al.*, "Novel Widely Tunable Monolithically Integrated Laser Source," *IEEE Photonics J.*, vol. 7, no. 6, pp. 1–9, Dec. 2015.
- [5] R. Pajković, Y. Tian, S. Latkowski, K. A. Williams, and E. A. J. M. Bente, "Tuning of a widely tunable monolithically integrated InP laser for optical coherence tomography," in *Novel In-Plane Semiconductor Lasers XVIII*, San Francisco, United States, 2019, p. 37.
- [6] S. Andreou, K. A. Williams, and E. A. J. M. Bente, "Monolithically integrated InP-based DBR lasers with an intra-cavity ring resonator," *Opt. Express*, vol. 27, no. 19, p. 26281, Sep. 2019.
- [7] S. Andreou, K. A. Williams, and E. Bente, "Radio-Frequency Signal Generation Using Actively Frequency Stabilised Monolithically Integrated InP-Based Lasers," in *Proceedings ICTON 2019*, Angers, France, 2019, p. 4.

# Metamorphic heterostructures: new material concepts for telecom lasers and visible light-emitting diodes

Silviu Bogusevski<sup>1,2,\*</sup>, Christopher A. Broderick<sup>1,2</sup>, and Eoin P. O'Reilly<sup>1,2</sup>

<sup>1</sup>*Tyndall National Institute, University College Cork, Lee Maltings, Dyke Parade, Cork T12 R5CP, Ireland*

<sup>2</sup>*Department of Physics, University College Cork, Cork T12 YN60, Ireland*

*\*s.bogusevski@umail.ucc.ie*

## Abstract

We present a theoretical investigation of GaAs-based metamorphic quantum wells (QWs) for applications in telecom lasers and in amber/red light-emitting diodes (LEDs). We demonstrate that InGaAs metamorphic buffer layers allows access to 1.3 – 1.55  $\mu\text{m}$  emission wavelengths in (Al)InGaAs structures, or visible wavelengths in Al(Ga)InP structures. We identify and quantify trends in the properties and performance in these wavelength ranges, and identify optimised structures for practical applications. For telecom laser structures we demonstrate threshold current densities and differential gain which compare favourably with optimised InP-based devices. For amber/red LED structures we illustrate the potential to suppress losses associated with carrier leakage.

## 1 Introduction

Metamorphic growth of semiconductor materials in which a virtual substrate with a desired lattice constant is obtained by growing a lattice-mismatched metamorphic buffer layer (MBL) on a conventional substrate, such as InP or GaAs is attracting increasing interest due to its potential to facilitate the development of improved optoelectronic technologies. For example, by growing a relaxed InGaAs MBL on a GaAs substrate, heterostructures can be grown having lattice constants intermediate between those of GaAs and InP, providing enhanced scope for band structure engineering and hence the design of semiconductor lasers and LEDs. We undertake a theoretical analysis of GaAs-based 1.3 and 1.55  $\mu\text{m}$  metamorphic QW lasers, and 610 nm metamorphic QW-LEDs, and predict in both cases improvements in performance that can be achieved compared to conventional heterostructures.

## 2 Theoretical model

Our analysis based on an 8-band  $\mathbf{k}\cdot\mathbf{p}$  Hamiltonian describing the  $\Gamma$ -point conduction and valence band edge states, including the effects of spin-orbit coupling, strain and band mixing on the band structure of the AlInGa(As,P) QWs grown on InGaAs MBLs. Numerical calculations of the QW electronic properties proceed via a reciprocal space (plane wave) approach, with the multi-band envelope functions used directly to compute spontaneous emission and optical gain spectra under electrical injection [1]. For the 610 nm Al(Ga)InP structure we additionally include the impact of energetically close X-point conduction states via a strain-dependent effective mass model [2].

## 3 Results and discussion

Firstly, we identify the ranges of alloy compositions compatible with growth of direct-gap AlInGaAs and AlInGaP alloys as suitable barrier materials. This demonstrates that on an InGaAs MBL allows (i) increased barrier band gap, and (ii) larger conduction band offset, providing enhanced electronic and optical confinement in GaAs-based multi-QW structures. Secondly, via systematic analysis we determine the combinations of alloy composition, strain and QW thickness providing peak optical gain at 1.3 and 1.55  $\mu\text{m}$ , and optimum spontaneous emission at 610 nm. We find, e.g., that InGaAs/(Al)InGaAs QWs grown on InGaAs MBLs having compressive strains  $\lesssim 2\%$  can reach emission wavelengths  $\sim 1.3 \mu\text{m}$  [1, 3]. We also demonstrate the possibility to grow 610 nm direct-gap AlInP QWs on InGaAs MBLs without the requirement to incorporate Ga, which is expected to suppress CuPt alloy ordering and reduce defect density, thereby facilitating high quality epitaxial growth [4].

Turning our attention to the electronic and optical properties of these heterostructures, we focus on (i) compressively strained 1.3 – 1.55  $\mu\text{m}$  InGaAs QWs having (Al)InGaAs barriers, and (ii) compressively strained 610

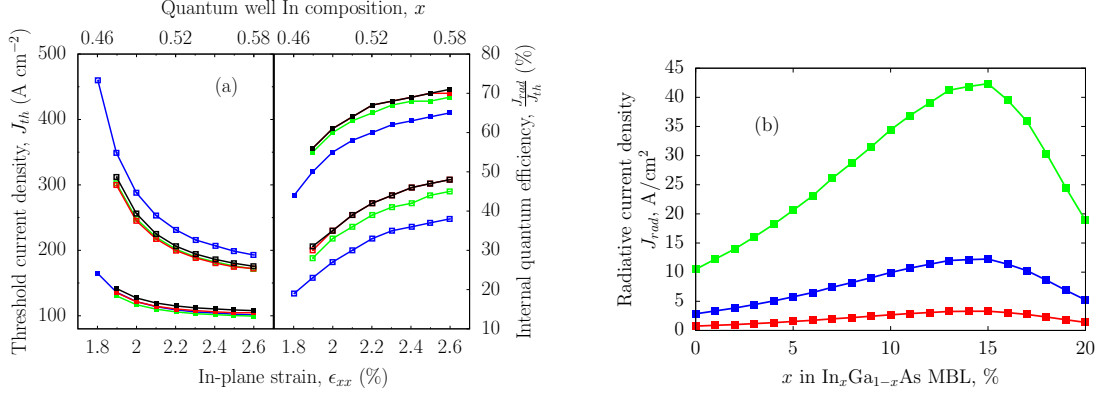


Figure 1: (a) Calculated variation of the threshold current density (left panel) and internal quantum efficiency (right panel) with in-plane strain and QW In composition at  $T = 300$  K (solid lines, closed squares) and  $360$  K (dashed lines, open squares), in compressively strained  $1.3 \mu\text{m}$  InGaAs/AlInGaAs metamorphic QWs. The QWs have unstrained  $\text{Al}_y\text{In}_{0.2}\text{Ga}_{0.8-y}\text{As}$  barriers with  $y = 0, 6, 12$  or  $15\%$  (blue, green, red and black squares/lines, respectively). (b) Calculated variation of the radiative current density with MBL In composition, for injected sheet carrier densities  $n_{2D} = 0.5, 1.0$  and  $2.0 \times 10^{12} \text{ cm}^{-2}$  (red, green and blue squares/lines), in compressively strained AlInP/AlGaInP QWs designed to emit at  $610 \text{ nm}$  at  $T = 300 \text{ K}$ .

nm AlInP QWs having quaternary AlIn(Ga)P, with the barriers in both (i) and (ii) being lattice-matched to the InGaAs MBL. Having identified structures with the desired emission wavelengths, we compute the optical properties as functions of the QW strain and thickness to identify key trends in the expected device performance. For metamorphic  $1.3$  and  $1.55 \mu\text{m}$  (Al)InGaAs laser structures (cf. Fig. 1(a)) we find reduced threshold current density, comparable internal quantum (radiative) efficiency and enhanced differential gain at threshold compared to those calculated previously for optimised InP-based multi-QW structures [1, 3]. Our calculations further illustrate that the barrier Al composition can be varied to optimise the trade-off between the carrier and optical confinement, with these effects becoming more important in determining the device performance with increasing temperature.

For  $610 \text{ nm}$  Al(Ga)InP QW-LEDs we find that metamorphic growth on InGaAs MBLs delivers significantly improved electron confinement. This, combined with the aforementioned benefits of minimising GaP incorporation, is expected to enable (i) reduce thermal carrier leakage from the QWs during electrically pumped operation at and above room temperature, and (ii) mitigate the reduction in radiative efficiency associated with scattering of thermally distributed electrons into (delocalised) X-point states in the barrier layers, and (iii) reduce the carrier density required to achieve a given radiative recombination rate compared to that in an equivalent structure grown on GaAs (cf. Fig. 1(b)).

## 4 Conclusion

We have undertaken a theoretical investigation and optimisation of the properties and performance of GaAs-based metamorphic  $1.3 - 1.55 \mu\text{m}$  (Al)InGaAs QW lasers and  $610 \text{ nm}$  Al(Ga)InP QW-LEDs. Our theoretical analysis has identified key trends in the performance of these novel GaAs-based heterostructures, confirmed their strong potential for practical applications, and provided design parameters for optimised device structures.

## References

- [1] S. Bogusevski, C. A. Broderick, and E. P. O'Reilly. Theory and optimization of  $1.3 \mu\text{m}$  metamorphic quantum well lasers. *IEEE J. Quantum Electron.*, 52:2500111, 2015.
- [2] S. Bogusevski, A. Pescaglini, E. Pelluchi, and E. P. O'Reilly. AlGaInP quantum well based  $610 \text{ nm}$  metamorphic LEDs as efficient red light emitters. *Proc. Numerical Simulation of Optoelectronic Devices*, 2017.
- [3] C. A. Broderick, S. Bogusevski, and E. P. O'Reilly. Theory and optimization of  $1.3$  and  $1.55 \mu\text{m}$  (Al)InGaAs metamorphic quantum well lasers. *Proc. Numerical Simulation of Optoelectronic Devices*, 2016.
- [4] A. Pescaglini, A. Gocalinska, S. Bogusevski, S. T. Moroni, G. Juska, E. E. Mura, J. Justice, B. Corbett, E. P. O'Reilly, and E. Pelluchi. Three-dimensional self-assembled columnar arrays of AlInP quantum wires for polarized micrometer-sized amber light-emitting diodes. *ACS Photonics*, 5:1318, 2018.

# High-frequency chaotic dynamics of laser diodes with long phase-conjugate feedback

G. Bouchez,<sup>1,2\*</sup> D. Wolfersberger,<sup>1,2</sup> M. Sciamanna<sup>1,2</sup>

<sup>1</sup>Chaire Photonique, LMOPS, CentraleSupélec, Université Paris-Saclay, Metz, France

<sup>2</sup>Université de Lorraine, CentraleSupélec, LMOPS, Chaire Photonique, F-57070 Metz

\*guillaume.bouchez@centralesupelec.fr

**Abstract:** We analyze the chaos generated by a laser diode submitted to phase-conjugate feedback. Its chaos bandwidth, effective chaos bandwidth and spectral flatness are characterized for different values of feedback strength. We report an increase of the bandwidth and of the flatness when increasing the feedback strength. Although the external cavity is 1.5-meter long, we obtain remarkably high frequency dynamics. In particular, a maximum chaos bandwidth of 30.4 GHz and effective bandwidth of 21.07 GHz are reported for an intermediate value of feedback strength.

## 1. Introduction

When submitted to optical feedback, laser diodes are able to generate a great variety of nonlinear dynamics, such as temporal chaos. Such signal is useful for various telecommunication or metrology applications [1]. We use here the phase-conjugate feedback (PCF) to unlock ultra-fast high frequency chaos. Such a system is known to generate the so-called external cavity modes (ECM), where the output power oscillates periodically at a multiple of the frequency of the round-trip time of the cavity, hence with a possibly very high frequency [2]. These high frequency solutions have been shown also to significantly enhance the bandwidth when these ECMs bifurcate to chaos [3]. We extend here our study of the chaos bandwidth, defined as the upper frequency of the power spectrum that contains 80% of the signal energy, and also analyze the effective chaos bandwidth, defined as the sum-up of the discrete components of the spectrum that contains 80% of the signal energy [4], and the spectral flatness, here defined as the ratio of the geometric and arithmetic means of the power spectral density. Of particular interest for us is the case of a very long delayed feedback which has not been analyzed before.

## 2. Laser system

The set-up of the system is presented figure 1. Our laser diode is a commercial Fabry-Pérot laser diode, emitting at 852 nm and whose threshold current is equal to 14.9 mA. Its operating current is set to 80 mA and the frequency of relaxation oscillations ( $f_{RO}$ ) is 5.2 GHz. A beam-splitting plate (BS) deviates 18% of the output beam into a fiber through a coupler. An isolator (ISO) prevents reflections from the fiber into the laser. The fiber is connected to a 38 GHz-bandwidth photodiode, associated with a 40 GHz oscilloscope.

This system uses a degenerate four-wave mixing in a photorefractive Rh-doped BaTiO<sub>3</sub> mirror to generate the backward phase-conjugate beam. Such a mirror is also called self-pump phase-conjugate mirror (SPPCM). A lens focalized the laser beam at the entrance of the crystal. The beam-splitting plate deviates 18% of the feedback into a powermeter (PM), thus enabling the measure of the feedback strength. Due to the time-dependent fluctuations of the PCF mirror reflectivity, the radio-frequency spectrum is studied by calculating the Fourier transform of the measured power over short times. Several 450 ns-long times series are recorded for different feedback strengths.

The length of the external cavity is 1.535 m, associated with a round-trip time of 10.3 ns and a frequency  $f_{EC}=97.09$  MHz. Such a long delay when used in conventional optical feedback is generally incompatible with high-frequency dynamics. However, we expect the high-frequency dynamics generated by PCF to be relatively immune to increasing time-delay [5].

## 3. Results and discussion

We report on figure 2 the evolution of the chaos bandwidth, effective bandwidth and spectral flatness. External cavity modes oscillating at 9.8 to 10.86 GHz (101<sup>th</sup> to 112<sup>th</sup> harmonics of  $f_{EC}$ ) appears at feedback strength values around 3-4%. As described in our recent study [4], the chaos bandwidth (blue stars on top of figure 2) first increases with the feedback strength and then reaches high values when the feedback strength is greater than 2.5% and saturates for larger feedback strength. The chaos bandwidth reaches 30.2 GHz for a feedback strength of 3.6%. This chaos bandwidth is nearly equal to 80% of the photodiode bandwidth (30.4 GHz). In this case, the frequency of the relaxation of oscillations has completely disappeared from the spectrum.

The effective bandwidth (red crosses on top of figure 2) has the same behavior but its values are always inferior to the chaos bandwidth, which is consistent with other studies [3]. The maximum is obtained for the time series that also maximizes chaos bandwidth, at feedback strength equal to 3.6%, and rises to 21.1 GHz.

The spectral flatness (figure 2 bottom) shows the same evolution. For low feedback values, most of the frequencies are located around the relaxation oscillation frequency and the flatness is very bad. As higher frequencies are unlocked when the feedback strength exceeds 3%, the flatness then increases. Quasi-steady states at low feedback strength and ECMs generate also quite flat spectra, since most of the frequency components are equal to the electronic noise of the measurement system. Due to some parasitic resonances of the oscilloscope at some very discrete frequencies we estimate the flatness of an electronic white noise to about 0.82. For the same optimal time series than previously (3.6 GHz), the spectral flatness rises to 0.77 which is then close to the best achievable value experimentally for a white noise.

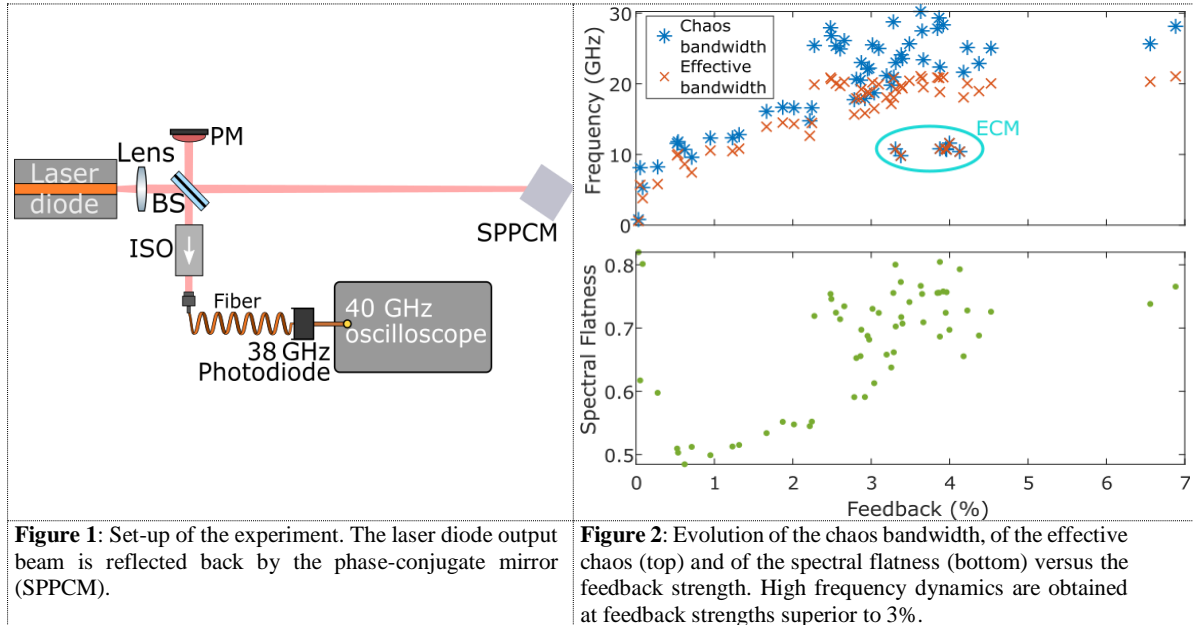


**Figure 1:** Set-up of the experiment. The laser diode output beam is reflected back by the phase-conjugate mirror (SPPCM).

**Figure 2:** Evolution of the chaos bandwidth, of the effective chaos (top) and of the spectral flatness (bottom) versus the feedback strength. High frequency dynamics are obtained at feedback strengths superior to 3%.

For the particular time series that presents the optimal performances, the spectrum reveals large frequency bumps of chaos around 30 GHz. The time series shows nanosecond-scale intermittency between a periodic ECM solution and a very complex chaotic state. This phenomenon has been observed for other time series.

#### 4. Conclusion

In this talk, we study the self-pulsing and chaotic states of a laser diode with phase-conjugate feedback. In spite of the long delay - which in other feedback configurations would lead to slow dynamics - we report on very fast self-pulsing states at a frequency well beyond  $f_{RO}$  and up to 100 times the external cavity frequency, but also on large-band and flat optical chaos with a bandwidth around 30GHz. Such performance is remarkable for a single feedback system i.e. without additional coupling or injection.

#### 5. References

- [1] M. Sciamanna and K. A. Shore, "Physics and applications of laser diode chaos," *Nat. Photonics* vol. 9, pp. 151-162 (2015)
- [2] A. Karsaklian Dal Bosco, D. Wolfersberger and M. Sciamanna, "Superharmonic self-pulsations from a time-delayed phase-conjugate optical system," *Appl. Phys. Lett.* vol. 105, p. 081101 (2014)
- [3] G. Bouchez, C.-H. Uy, B. Macias, D. Wolfersberger and M. Sciamanna, "Wideband chaos from a laser diode with phase-conjugate feedback," *Optics Letters* vol. 44, no. 4, pp. 975-978 (2019)
- [4] F. Y. Lin, Y. Chao and T. Wu, "Effective Bandwidths of Broadband Chaotic Signals," *IEEE J. Quantum Elec.*, vol. 48, no. 8, pp. 1010-1014 (2012)
- [5] É. Mercier, C.-H. Uy, L. Weicker, M. Virte, D. Wolfersberger and M. Sciamanna, "Self-determining high-frequency oscillation from an external-cavity laser diode," *Phys. Rev. A*, vol. 94, no. 6, p. 061803 (2016)

# High Power Surface Emitting Superluminescent LEDs

R. Cahill,\* J. Morales, B. Corbett

<sup>1</sup>Tyndall National Institute, University College Cork, Lee Maltings, Dyke Parade, Cork, Ireland

\*rory.cahill@tyndall.ie

**Abstract:** A high power blue superluminescent light-emitting diode emitting normal to the substrate is demonstrated. The device uses a structure in which a monolithically integrated turning mirror reflects the light at both ends of the in-plane waveguide downward through the transparent bulk GaN substrate. Record optical peak powers of  $>2$  W are achieved under pulsed operation. The combination of turning mirrors with an antireflection coating limits feedback in the waveguide resulting in a broad smooth spectrum centered at 416nm with a FWHM of 6 nm.

## 1. Introduction

Superluminescent light-emitting diodes (SLEDs) combine different elements of laser diode and LED performance. A ridge waveguide structure is used to confine the light in the same way as a LD. Reflections at the facets are limited to reduce feedback in the cavity and prevent the formation of Fabry-Perot modes. The gain mechanism then is amplified spontaneous emission (ASE). The result is a high power, directional light source with a broad, smooth emission spectrum. These characteristics have made SLEDs subject to intensive research over the past decades[1-3]. The first SLEDs were introduced in the GaAs material system in 1973 [4] using an absorbing rear facet to suppress the formation of FP modes. All edge emitting SLEDs eventually break down to lasing at high currents due to parasitic feedback which limits the quality of the spectral emission. The first blue emitting SLEDs were reported in 2009 [1]. Since then a wide range of strategies such as roughened facets [3], passive absorbing regions[5] and bent waveguide structures have been employed in attempts to reduce feedback in the waveguide. The first CW operation of GaN SLEDs have been recently reported[6], record optical peak powers of 474mW under pulsed operation [7], spectral bandwidths  $> 10$  nm (70meV) [8] and external quantum efficiencies (EQE) of  $\sim 20\%$  in CW operation. The unique characteristics of beamed power and low temporal coherence at short wavelengths make GaN based SLEDs ideal candidates for applications such as pico-projection, high resolution optical coherence tomography, micro-display applications and smart solid state lighting. They have also been suggested as sources for visible light communication due to reported high modulation bandwidth[9]. Here we present our substrate emitting SLEDs, using a novel turning mirror structure to divert light travelling in the plane of the waveguide downward through the transparent substrate by total internal reflection. The surface emitting design provides significant advantages such as the potential for on-wafer testing prior to packaging which could reduce production costs.

## 2. Model description, experimental setup

SLEDs were fabricated on freestanding n-type GaN substrates with the epitaxial layers grown by metal organic vapour phase epitaxy (MOVPE). The structure was a standard laser waveguide with two InGaN quantum wells (QWs) between p and n type AlGaIn cladding layers. A  $3 \mu\text{m}$  wide by 1 mm ridge was dry etched to confine the light in the lateral direction. Two  $45^\circ$  turning mirrors were then etched, one at either end of the waveguide. The transparent GaN substrate was polished to minimize the scattering of the beam. A  $\text{SiO}_2$  anti-reflection (AR) coating was applied to the substrate surface of the wafer to improve light extraction and further reduce feedback.

## 3. Results and discussion

The light-current-voltage characteristics of the device were measured under pulsed operation with a pulse length of 220 ns and a 1% duty cycle. The threshold for superluminescent operation is at 300 mA ( $\sim 10 \text{ kA cm}^{-2}$ ). Above this current a super-linear increase in optical power with current is observed. The operating voltage of the device is between 6 V and 7 V. The maximum optical peak power (both facets) was measured to be 2.2 W at 1.5 A driving current. This corresponds to an EQE of 49%. The electroluminescence spectrum of the device was also measured at different driving currents. The emergence of the ASE peak can be seen at 400 mA. The spectrum remains broad and smooth with no evidence of parasitic lasing up to the maximum drive current.

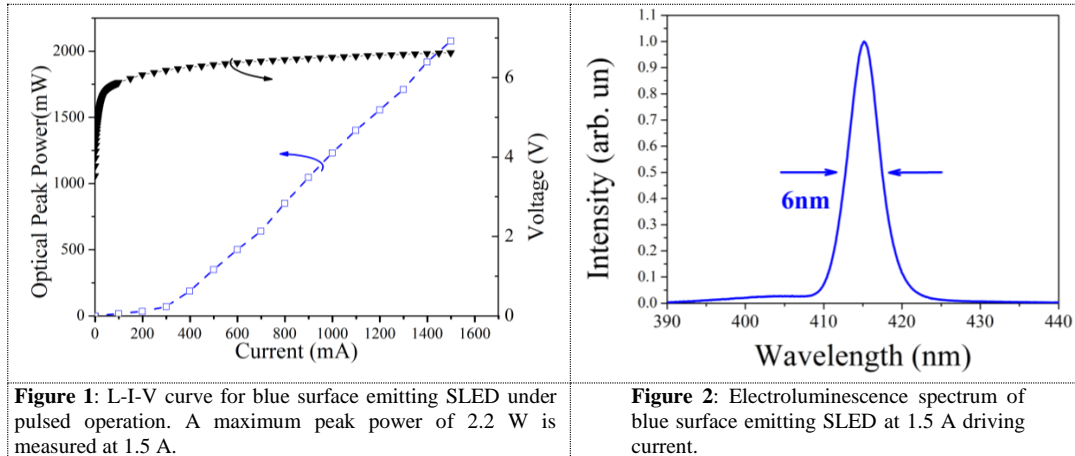


**Figure 1:** L-I-V curve for blue surface emitting SLED under pulsed operation. A maximum peak power of 2.2 W is measured at 1.5 A.

**Figure 2:** Electroluminescence spectrum of blue surface emitting SLED at 1.5 A driving current.

#### 4. Conclusion

A high power surface emitting SLED emitting in the blue is demonstrated. A maximum optical peak power of 2.2 W under pulsed operation is reported. The turning mirror design combined with an AR coating is effective in preventing parasitic lasing allowing for a broad smooth emission spectrum with a FWHM of 6 nm.

#### 5. Acknowledgement

The authors would like to acknowledge funding from Enterprise Ireland and the European Structural and Investment Funds 2014-2020 program.

#### 6. References

1. Feltin, E., et al., *Broadband blue superluminescent light-emitting diodes based on GaN*. Applied Physics Letters, 2009. **95**(8): p. 081107.
2. Kafar, A., et al., *Cavity suppression in nitride based superluminescent diodes*. Journal of Applied Physics, 2012. **111**(8): p. 083106.
3. Matthew, T.H., et al., *m -Plane GaN-Based Blue Superluminescent Diodes Fabricated Using Selective Chemical Wet Etching*. Applied Physics Express, 2009. **2**(12): p. 121004.
4. Tien-Pei, L., C. Burrus, and B. Miller, *A stripe-geometry double-heterostructure amplified-spontaneous-emission (superluminescent) diode*. IEEE Journal of Quantum Electronics, 1973. **9**(8): p. 820-828.
5. Kafar, A., et al., *InAlGaIn superluminescent diodes fabricated on patterned substrates: an alternative semiconductor broadband emitter*. Photonics Research, 2017. **5**(2): p. A30-A34.
6. Marco, R., et al., *High Power Blue-Violet Superluminescent Light Emitting Diodes with InGaIn Quantum Wells*. Applied Physics Express, 2010. **3**(6): p. 061002.
7. Alatawi, A.A., et al., *High-power blue superluminescent diode for high CRI lighting and high-speed visible light communication*. Optics Express, 2018. **26**(20): p. 26355-26364.
8. Goldberg, G.R., et al., *Gallium Nitride Superluminescent Light Emitting Diodes for Optical Coherence Tomography Applications*. IEEE Journal of Selected Topics in Quantum Electronics, 2017. **23**(6): p. 1-11.
9. Shen, C., et al. *Semipolar InGaIn-based superluminescent diodes for solid-state lighting and visible light communications*. in *SPIE OPTO*. 2017. SPIE.

# Type II excitability in optical injected quantum dot lasers

Michael Dillane<sup>1,2\*</sup>, Joshua Roberson<sup>5</sup>, David Goulding<sup>2,3,4</sup>, Antonio Hurtado<sup>5</sup>, Bryan Kelleher<sup>1,2</sup>

<sup>1</sup>Department of Physics, University College Cork, Ireland

<sup>2</sup>Tyndall National Institute, University College Cork, Lee Maltings, Dyke Parade, Cork, Ireland

<sup>3</sup>Centre for Advanced Photonics and Process Analysis, Cork Institute of Technology, Cork, Ireland

<sup>4</sup>Department of Mathematics, Cork Institute of Technology, Cork, Ireland

<sup>5</sup>Institute of Photonics, SUPA Department of Physics, University of Strathclyde, TIC Centre, 99 George Street, Glasgow G1 1RD, UK 1142, New Zealand

\*michael.dillane@tyndall.ie

**Abstract:** Type II excitability is observed in an optically injected quantum dot laser in a unidirectional master-slave configuration. At high injection strengths, excitable square pulses are observed. The quantum dot model predicts a bistability in this region, however the bistability is broken by optothermal coupling resulting in a deterministic cycle. Depending on the photon lifetime this cycle can be born from a subcritical or supercritical Hopf bifurcation. Experimental phase measurements show a bounded phase, further evidence of a Hopf bifurcation. Crucially these pulses can be deterministic triggered which is vital for real world applications.

## 1 Introduction

Excitability is one of the most interesting topics in nonlinear dynamics. Recently there have been efforts to utilise semiconductor devices and their associated non-linear dynamics in photonic neural networks. One of the main advantages of such a network over their electronic counterparts is that the speed of light is orders of magnitude faster than electricity. The work put forward here tackles the fundamental understanding of excitability, the dynamical phenomenon at the heart of neural communication.

While multiple semiconductor device configurations have been shown to produce excitable pulses, we will focus on quantum dot lasers and specifically optically injected quantum dot lasers. Typically, in a master slave setup with low injection strength, Type I excitability is seen [1]. However, we show here that by increasing the injection strength so the injected light is of the same order of the output light, Type II optothermal excitability can be observed [2]. The same experimental setup was used to acquire both Type I and Type II excitability and simply by varying the control parameters - injection strength and detuning, - we can move between these two types of excitability. In [2] histograms of the interpulse times of the square pulses showed exponential distributions [2] demonstrating their stochastic nature. Here we expand on that work and show that the square pulses can be deterministically triggered, a necessity for most real world applications.

## 2. Experimental

At moderately high injection strengths and for very large negative detuning the system is unlocked. As the magnitude of the detuning is decreased the slave becomes phase locked to the master via a Hopf bifurcation as in the standard injection system. However, by further decreasing the magnitude of the detuning, square wave trains are obtained. These are random at first and become periodic as the detuning is further decreased. Continuing to decrease the detuning, the trains eventually resemble a periodic square dropout train, followed by randomly spaced square dropouts and finally the device becomes phase locked again.

To examine the excitable nature of the pulses, an external perturbation was applied to the injected light via a phase modulator driven by a pulse generator. Fast rise and fall times, approximating instantaneous perturbations are necessary to trigger the excitable responses; slow perturbations would result in the phase of the slave simply “following” the phase of the master. Further, there should exist a threshold perturbation strength for the excitable pulses. Figure 1 shows the efficiency curve for different perturbation strengths demonstrating a clear threshold of approximately 2.4 V. Importantly at 3 V there is 100% efficiency.

The width of the square pulses are in the order of microseconds, while the rise time of the pulses is on the order of nanoseconds. The fast-slow nature of the system suggests that this is Type II excitability, which typically arises via Hopf bifurcations. To gain further insight, the phase of the squares pulses was investigated. It was found that the phase is bounded, a typical outcome of Hopf bifurcations in the optically injected laser system [3]. Physically we interpret the phenomenon as arising from an optothermal coupling. Each square consists of a fast excitation followed by a slow deterministic drift of the detuning and finally a fast return to the steady state.

By measuring the frequency evolution of the output during the slow part of the squares such a slow but deterministic drift was indeed obtained.

### 3. Theory

It has been shown that because the relaxation oscillation damping of quantum dot lasers is so high one can get excellent qualitative agreement of the dynamical regimes using a Class A laser model. This model again proved to be sufficient to recreate square wave excitability as shown in [2]. A bifurcation analysis shows that the pulses are born via a Supercritical Hopf bifurcation with an associated Canard explosion, where there is a rapid increase in the amplitude of a cycle over a small parameter range as shown in Figure 2.

Recently however, using a quantum dot specific model, we have found that depending on the photon lifetime, the cycle can be born from a supercritical or subcritical Hopf bifurcation. The supercritical Hopf in this case is similar to the one discussed with the Class A model and again features a canard explosion. For the case of the subcritical Hopf bifurcation however, a bistability arises between a constant steady state solution and a square wave cycle. Close to the bistable region noise can stimulate a square pulse.

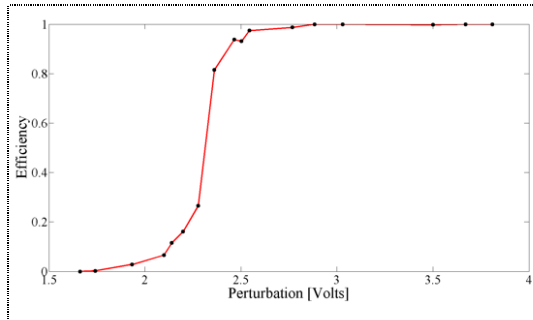


**Figure 1:** Efficiency curve for deterministically triggered square pulses. Electric pulses were applied to a phase modulator, modulating the light injected into the slave. The threshold is approximately 2.4 V. Perturbations above 3 V yield 100% efficiency.

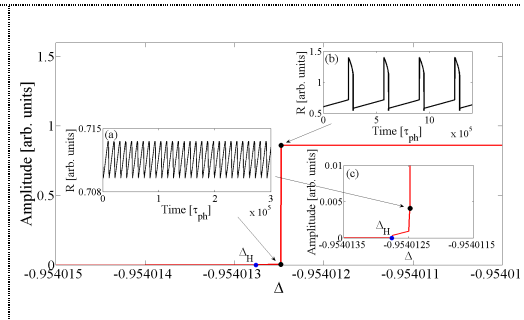


**Figure 2:** A supercritical Hopf bifurcation and the resulting Canard Explosion. (a) shows the small amplitude oscillations, (b) the large amplitude oscillations, in this case, periodic square train. (c) shows a zoom so it's easy to see how small the parameter range is.  $\Delta$  is the detuning.

### 4. Conclusion

We have shown that optically injected quantum dot lasers capable of producing Type I and Type II excitability and may even yield a canard explosion. Both square pulses and square drop outs are observed, with possible applications as excitatory and inhibitory pulses. The ability to deterministically trigger these square pulses brings the system one step closer to photonic neuron applications.

### 5. References

- [1] D. Goulding, S. P. Hegarty, O. Rasskazov, S. Melnik, M. Hartnett, G. Greene, J. G. McInerney, D. Rachinskii, and G. Huyet, Phys. Rev. Lett. 98, 153903 (2007).
- [2] M. Dillane, B. Tykalewicz, D. Goulding, B. Garbin, S. Barland, and B. Kelleher, "Square wave excitability in quantum dot lasers under optical injection," Opt. Lett. 44, 347-350 (2019).
- [3] B. Kelleher, D. Goulding, B.B. Pascual, S.P. Hegarty, "Bounded phase phenomena in the optcially injected laser," G. Huyet, Phys. Rev. E 85, 046212 (2012).

# Nonlinear laser dynamics induced by injection of a frequency comb

Y.Doumbia,<sup>1,2\*</sup> T. Malica,<sup>1,2</sup> D. Wolferberger,<sup>1,2</sup> K. Panajotov,<sup>3,4</sup> M. Sciamanna<sup>1,2</sup>

<sup>1</sup> Chaire Photonique, LMOPS, CentraleSup\_elec, Universit\_e Paris-Saclay, Metz, France

<sup>2</sup> Universit\_e de Lorraine, CentraleSup\_elec, LMOPS, Metz, France

<sup>3</sup> Brussels Photonics Group (B-PHOT), Vrije Universiteit Brussel, Brussels, Belgium

<sup>4</sup> Institute of Solid State Physics, Bulgarian Academy of Sciences, Sofia, Bulgaria

\*yaya.doumbia@centralesupelec.fr

**Abstract:** We analyze the nonlinear dynamics of a semiconductor laser with optical injection from a frequency comb. we identify and select several dynamics including (i) injection locking, (ii) unlocked time-periodic dynamics, and (iii) unlocked chaotic dynamics.

## 1 Introduction

The injection locking properties of semiconductor lasers have been analyzed since more than forty years :first, as a way to control the coherence properties of the injected laser, but more recently, as a technique to tailor specific nonlinear dynamics including optical chaos [1], time-periodic self-pulsation [2], and also dissipative solitons in large aperture laser diodes [3]. These nonlinear dynamics found applications in various fields such as: the physical security based on optical chaos, optical sensing, and radio-over fiber communications. Much less studied is the dynamics of a single mode laser diode injected by a multimode laser diode. This configuration has raised recent interest within the context of optical frequency combs.

In this Letter, we make an in-depth analysis of single mode semiconductor laser dynamics induced by optical injection of a frequency comb by varying both the injection parameters and the comb properties. The number of the resulting comb modes can be tailored by varying the injection parameters and the initial comb properties (number of modes and the comb spacing).

## 2. Model description, experimental setup

The laser system is modelled with equations from Ref. [4] adapted to injection from a comb. The electrical field in the slave laser cavity after injection is defined as [4]:

$$\frac{dE_s(t)}{dt} = \left\{ i\omega(N) + \frac{1}{2} \left[ G(N) - \frac{1}{\tau_p} \right] \right\} E_s(t) + E_M(t), \quad (1)$$

Where  $E_s(t)$  and  $E_M(t)$  are respectively the complex field of the slave and the master laser. Here,  $i$  is the imaginary number,  $N$  is the carrier density,  $\omega(N)$  and  $G(N)$  are respectively the angular optical frequency and the differential gain of the slave laser and  $\tau_p$  is the photon lifetime. The complex electrical field of the injected comb and slave laser can be written as:

$$E_M(t) = K \sum_j E_j(t) e^{(2\pi\nu_j t - \phi)}, \quad (2)$$

$$E_s(t) = E(t) \sum_j e^{(2\pi\nu_s t - \phi(t))}, \quad (3)$$

Where  $K$  is the coupling efficiency coefficient,  $E_j(t)$  and  $E(t)$  are the amplitudes of the  $j$ -th comb-line and of the slave laser.  $\nu_j$  and  $\nu_s$  are the frequencies of the  $j$ -th combs-line and of the slave laser.  $j$  is equal to zero for the central comb mode  $\Delta\nu_j = \nu_j - \nu_s$  is the detuning between the slave laser and  $j$ -th comb mode.  $\phi$  and  $\phi(t)$  are respectively the initial phase of each comb-line and the phase of the slave laser. To simplify the calculations, we set the initial phase of each comb-line to 0 and we suppose that the comb modes have the same amplitudes,  $E_{inj}$ . By doing the same calculation as in [4], the amplitude, phase and the carrier density rate equations can be rewritten as:

$$\frac{dE_s(t)}{dt} = \frac{1}{2} G_N(N(t) - N_{th}) - K E_{inj} \sum_j \cos(2\pi\Delta\nu_j t - \phi(t)) \quad (4)$$

$$\frac{d\phi(t)}{dt} = \frac{1}{2} \alpha G_N(N(t) - N_{th}) - K \frac{E_{inj}}{E(t)} \sum_j \sin(2\pi\Delta\nu_j t - \phi(t)) \quad (5)$$

$$\frac{dN(t)}{dt} = R_p - \frac{N(t)}{\tau_s} - G_N(N(t) - N_{th}) E(t)^2 - \frac{E(t)^2}{\tau_p}. \quad (6)$$

In these equations,  $N_{th}$  is the threshold carrier density,  $\alpha$  is the linewidth enhancement,  $R_p$  is the pump rate and  $\tau_p$  is the carrier density lifetime. We consider  $K=0$  from 0.8. In the following, we shall use  $\kappa$  for the injection

strength with  $\kappa = K \frac{E_{inj}}{E_0}$  where  $E_0$  is the field amplitude of the slave laser without optical injection.

### 3. Results and discussion

We shall discuss the emergence of complex dynamics from the injection locked solution. Figure 1 for example shows a detailed mapping of the parameter region corresponding to time-periodic dynamics in the plane of the injection parameters. The region shaded in blue correspond to the time-periodic dynamics of the slave laser output. Time-periodic dynamics could either correspond to injection locking - in which case the slave laser output power oscillates periodically at the frequency corresponding to the injected comb mode spacing - or to an unlocked dynamic that corresponds to a new comb solution and which we call "comb x" in the mapping. The region shaded in red correspond the non-periodic dynamics of the slave laser which we identify as chaotic dynamics bifurcating from injection locked solution. We are not interested here by the peculiar chaotic properties of the slave laser dynamics but, by the parameter range in which the slave laser shows an optical comb dynamics and the corresponding comb properties. Interestingly, the unlocked comb dynamics of the slave laser extends to a much broader range of injection parameters than the injection locking solution. Figures 1 (a) and 1 (b) correspond to 3-comb modes and 7-comb modes injection respectively. The region around zero detuning is the injection locking region. We identify as many injection locking regions as the number of the comb modes; labelled 'IL' in the mapping. In both cases, we observe two regions of unlocked time-periodic dynamics (see regions labelled 'comb1' and comb2 in the mapping). The areas corresponding to the new comb solution extend both with the injection strength and with the detuning. We also notice that when increasing the master laser number of comb modes, i.e., comparing Figure 1 (b) to Figure 1 (a), the areas corresponding to the new comb solution extend more to the negative detuning as the injection strength increases. It is also worth noting that the comb1 region connect to the injection locking region, hence, suggesting that this new comb solution indeed bifurcates from the injection locking solution.

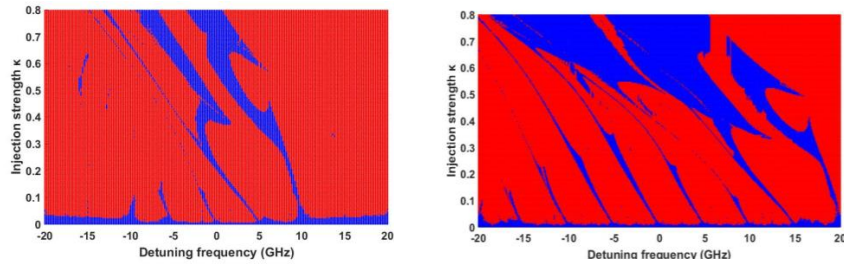


**Figure :** Numerical mapping of semiconductor laser subject to optical injection with frequency comb for  
Left: 3 comb modes and Right: 7 comb modes Comb spacing = 5 GHz.

### 4. Conclusion

In summary, we show that it is possible to generate a broadened frequency comb using injection locking technique. Increasing the injection strength, the slave laser gets locked, chaotic dynamics is observed. Most importantly, new comb solutions take place in the unlocked time-periodic dynamics. The pulse width of the mode-locked slave laser dynamics is controlled by injection parameters.

### 5. References

- [1] Marc Sciamanna and K Alan Shore. Physics and applications of laser diode chaos. Nature photonics, Vol. 9 no. 3, pp.151-162 (2015).
- [2] Lukasz Olejniczak, Krassimir Panajotov, Hugo Thienpont, and Marc Sciamanna. Self-pulsations and excitability in optically injected quantum-dot lasers: Impact of the excited states and spontaneous emission noise. Physical Review A, vol.82 no.2 pp.023807-023815, (2010).
- [3] Mathias Marconi, Julien Javaloyes, St\_ephane Barland, Salvador Balle, and Massimo Giudici. Vectorial dissipative solitons in vertical-cavity surface-emitting lasers with delays. Nature Photonics, vol.9 no.7 pp-450-462, (2015).
- [4] Finn Mogensen, Henning Olesen, and Gunnar Jacobsen. Locking conditions and stability properties for a semiconductor laser with external light injection. IEEE Journal of Quantum Electronics, vol.21 no.7 pp.784-793, (1985).

# The ESLW from 1983 to 2019: personal experiences and perspectives - Semiconductor emitters going from Telecom to Quantum

Wolfgang Elsässer

*Institute of Applied Physics, Technische Universität Darmstadt,  
Schlossgartenstrasse 7, 64289 Darmstadt (Germany)  
\*email: Elsaesser@physik.tu-darmstadt.de*

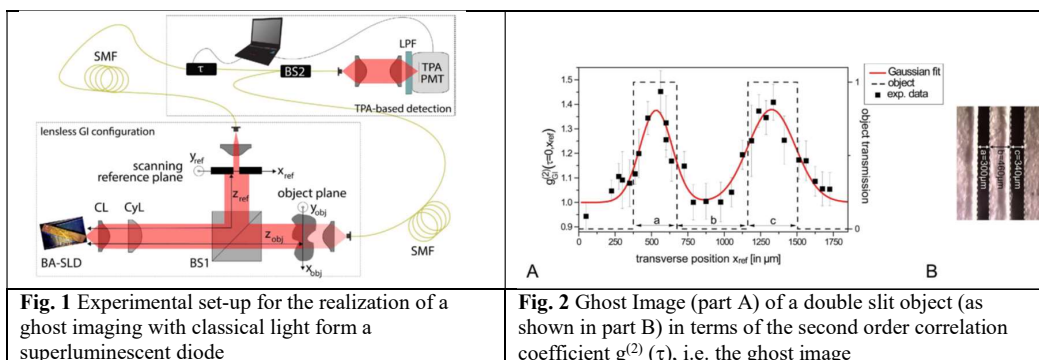
**Abstract:** The talk will start with a look back on the topics of the ESLW in the past, always accompanied by topics of ECOC and ISLC- Then, particular emphasis will be given of the quantum aspects of optoelectronic emitters. In the spirit of the Hanbury-Brown Twiss experiment from 1956, well before the first ELSW, photon correlations will be discussed as the beginning of quantum optics. already before the advent of the first laser. On this basis, we shall demonstrate that semiconductor-based superluminescent diodes emitting broad-band amplified spontaneous emission light are ideal photon bunching emitters with a second order correlation coefficient  $g^{(2)} = 2$ . We then exploit these photon bunching properties of optoelectronic emitters for ghost metrology applications as ghost imaging and ghost spectroscopy based on the spatial and spectral correlations of these classically correlated photons. We conclude by discussing further perspectives and possibilities of photon bunching for ghost metrology applications as e.g. ghost polarimetry.

## 1. Introduction

Ghost imaging (GI) is by far not a “spooky action” but rather a photon correlation imaging modality based on the fundamentals of quantum optics, either realized with entangled photons in the quantum GI version or with bunched photons from classical thermal sources. In contrast to conventional imaging systems, GI exploits intensity correlations of light to retrieve an image of an object. Ghost Imaging (GI) or photon-correlation imaging is one of the recent topics of quantum optics. After the first demonstration in 1995 with entangled photon [1] also classical GI [2,3] has been demonstrated with light emitted by rather complex, bulky thermal light sources. The name GI results from the fact that the image is formed by light which has never interacted with the object. Hereby, the total intensity of the transmitted or reflected light of an illuminated object and the spatially resolved intensity of a highly (position)-correlated reference beam which itself has never interacted with the object, are detected. The information of both intensities alone is not enough to form an image of the object. However, correlating the two intensities in terms of the intensity autocorrelation or second order correlation yields an image, the ghost image.

## 2. Ghost metrology: ghost imaging and ghost spectroscopy - concepts, results and discussions

Here, the presentation will start with the quantum aspects of optoelectronic emitters by discussing the experimental results of investigations of the second order coherence of extremely compact ultra-miniaturized superluminescent diode (SLD), i.e. demonstrating fundamental photon bunching of these Amplified Spontaneous Emission (ASE) emitting devices. We then proceed to the basics of ghost modalities by illustrating the key elements of GI with classical correlated light emitted by superluminescent diodes with the set-up schematically shown in Fig.1 and demonstrate ghost imaging results of a macroscopic double slit transmission object as depicted in Fig. 2.



Thus, we introduce to the field of ghost modalities a novel light source [4], being spectrally broad-band in 1<sup>st</sup> order coherence, in 2<sup>nd</sup> order coherence exhibiting Hanbury-Brown & Twiss photon bunching with a correlation coefficient of two and being spatially incoherent due to the dynamic mode filamentation of the broad-area waveguide structure.

We then extend the field of ghost modalities in analogy to this classical spatial GI principle with classical light to ghost spectroscopy. We propose and realize a first ghost spectroscopy (GS) experiment with classical light by exploiting spectral correlations of light emitted by a broad-band semiconductor-based superluminescent diode (SLD) and demonstrate the applicability of this ghost modality in a real-world proof-of-principle experiment by measuring a ghost absorption spectrum  $\alpha(\lambda)$  of the characteristic absorption features of chloroform at 1214nm, i.e. a ghost spectrum [5,6]. Figure 3 shows the schematic realization of this set-up and Fig. 4 shows the proof-of-principle demonstration experiment with the ghost absorption spectrum of chloroform.

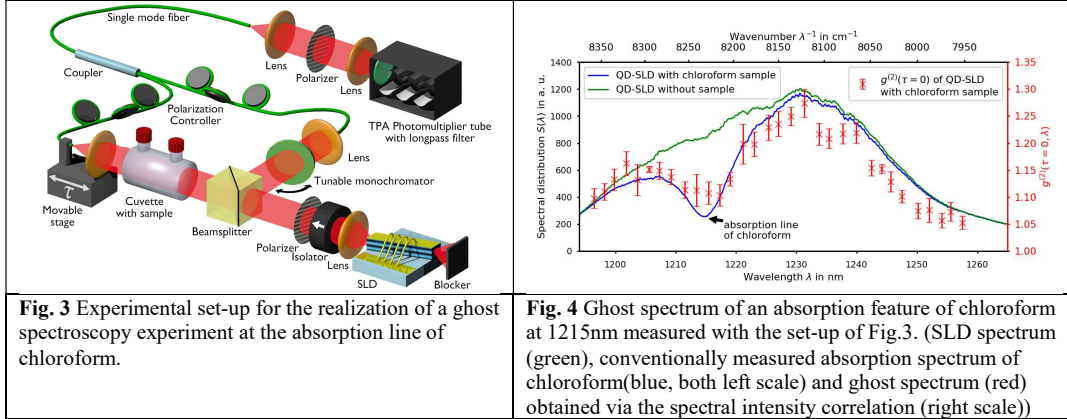


**Fig. 3** Experimental set-up for the realization of a ghost spectroscopy experiment at the absorption line of chloroform.

**Fig. 4** Ghost spectrum of an absorption feature of chloroform at 1215nm measured with the set-up of Fig.3. (SLD spectrum (green), conventionally measured absorption spectrum of chloroform(blue, both left scale) and ghost spectrum (red) obtained via the spectral intensity correlation (right scale))

### 3. Conclusions

This is the first time, that ghost spectroscopy has been realized with a broad-band semiconductor-based light source by exploiting the spectral correlations of a broad-band thermal semiconductor light source. Finally, we shall discuss further perspectives and possibilities of photon bunching in amplified spontaneous emission light suggesting the realization of ghost polarimetry (GP) by exploiting polarization correlations [7]. We are convinced that this amplified emission source concept and the pursued and exploited analogy between ghost imaging and ghost spectroscopy will further fertilize the field, thus allowing to develop a deeper understanding of the experimental scheme and even leading to other ghost metrology protocols.

### 4. References

- [1] T. B. Pittmann, Y. H. Shih, D. V. Strekalov and A. V. Sergienko, Phys. Rev. A **52**, R3429(R) (1995).
- [2] R. S. Bennink, S. J. Bentley and R. W. Boyd, Phys. Rev. Lett. **89**, 113601 (2002).
- [3] F. Ferri, D. Magatti, A. Gatti, M. Bache, B. E. and L. A. Lugiato, Phys. Rev. Lett. **94**, 183602 (2005).
- [4] S. Hartmann and W. Elsässer, Sci. Rep. **7**, 41866 (2017)
- [5] P. Janassek, S. Blumenstein, and W. Elsässer, Phys. Rev. Appl. **9**, 021001 (2018)
- [6] P. Janassek, S. Blumenstein, and W. Elsässer, Optics and Photonics News **29**, 41 (2018)
- [7] P. Janassek, S. Blumenstein, and W. Elsässer, Opt. Lett. **43**, 883 (2018)

### Acknowledgements

I acknowledge the contributions of Patrick Janassek and Sébastien Blumenstein who made this presentation only possible by their research. This work has been supported by the Deutsche Forschungsgemeinschaft (DFG). We gratefully acknowledge the excellent technological realization of the SLDs by M. Krakowski (III-V labs) and I. Krestnikov (Innolume) within the framework of the EU project “FAST-DOT”.

# Optical frequency comb quantum dash lasers subject to time-delayed optical self-injection

P. Fiala,<sup>1</sup> D. Auth,<sup>1\*</sup> C. Weber,<sup>1</sup> Q. Gaimard,<sup>2</sup> A. Ramdane,<sup>2</sup> and S. Breuer<sup>1</sup>

<sup>1</sup> Institute of Applied Physics, Technische Universität Darmstadt, Schlossgartenstraße 7, 64289 Darmstadt, Germany

<sup>2</sup> CNRS / Centre de Nanosciences et Nanotechnologies, 10 Boulevard Thomas Gobert, 91120 Palaiseau, France  
\*dominik.auth@physik.tu-darmstadt.de

**Abstract:** Inter-mode beat frequency tuning and phase noise reduction of a self mode-locked optical frequency comb semiconductor quantum dash laser emitting at 1550 nm by optical self-injection with delay lengths ranging from 6 m to 73 m is investigated. Tuning of the beat note frequency up to 22.5 MHz and inter-mode beat line width reduction from 110 kHz to 5.4 kHz are reported. Experimental inter-mode beat deviations and phase noise reduction show a quantitative agreement with simulation results obtained by a simple stochastic model.

## 1 Introduction

Monolithic semiconductor laser based optical frequency combs with center carrier wavelengths in the near- to mid-infrared spectral range are of immanent interest in high data rate optical communication or dual comb spectroscopy. As particular compact coherent multi-frequency super-channel sources in long-range optical communication, self mode-locked (SML) InAs/InP semiconductor quantum dash (QDh) lasers generate broadband optical frequency combs at center carrier wavelengths around 1550 nm [1]. Control of the inter-mode beat frequency (IBF) and reduction of the IBF line width can be achieved by optical self-injection and has been successfully demonstrated for quantum dot passively mode-locked (PML) lasers [2], quantum well PML lasers [3], quantum dot SML lasers [4], and QDh SML lasers [5-7]. An IBF line width reduction to 1 kHz of a 20 GHz two-section SML QDh laser with open absorber applying a dual-loop optical self-injection configuration has been demonstrated recently [5].

In this contribution, we validate that maximum attainable IBF tuning ranges and IBF line width reductions of a single-section self mode-locked QDh laser by optical self-injection follow the predictions of a stochastic time domain model, initially developed and confirmed in recent studies for PML quantum dot lasers [2], PML quantum well lasers [3], and SML quantum dot lasers [4] subject to optical self-injection.

## 2. Frequency comb laser & experimental set-up

The 2 mm long InAs/InP QDh laser was grown by gas source molecular beam epitaxy on (110) InP substrates by self-organized Stransky-Krastanov growth mode. Details can be found in [8]. A schematic of the experimental optical self-injection set-up is depicted in Fig. 1. The laser light is fiber-coupled by a lensed single-mode optical fiber yielding an estimated coupling efficiency of 30 %. A fiber beam splitter directs 50 % of the light towards the optical self-injection arm with lengths up to 73 m while 50 % are directed towards the emission analysis equipment via a 42 dB optical fiber isolator. A retro-reflecting broad-band mirror mounted on a motorized high-precision linear translation stage in a free-space part of the external self-injection cavity allows to fine-tune the microscopic optical fine-delay up to  $L_{mic} = 15$  mm corresponding to a time delay of 100 ps.

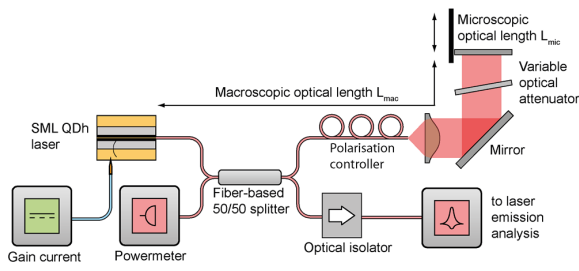


**Figure 1:** Schematic depiction of the single cavity optical self-injection set-up with multiple macroscopic delay lengths from 6.6 m to 73.8 m and automatized microscopic delay tuning over 15 mm.

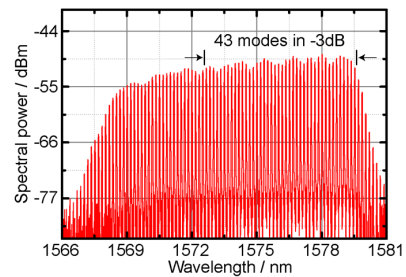


**Figure 2:** Optical spectrum of the solitary 2 mm long SML QDh laser including 43 modes within the -3 dB spectral width.

## 3. Stochastic model description

To predict and validate the experimentally studied dependencies of IBF tuning and IBF line width reduction on the fine-delay, a stochastic time domain model is adapted which considers a mode-locked semiconductor laser as a free-running oscillator exhibiting timing deviations within each round trip, induced by amplified

spontaneous emission [2]. After each round-trip, the timing deviation is accumulated leading to a Wiener process or a random walk. The timing deviation  $T(n+1)$  from an ideal reference clock of the  $n+1$  pulse for optical self-injection hence follows:

$$T(n+1) = [T(n) + \sigma_{ptp}\Gamma(n) + \gamma W(T(n) - T(n - n_d))T(n - n_d)] / [1 + \gamma W(T(n) - T(n - n_d))]$$

where  $\sigma_{ptp}$  is the pulse-to-pulse timing jitter which is accessed by measuring the fundamental IBF line width in the radio-frequency spectrum [9],  $\gamma$  is the timing interaction strength and  $n_d$  is the discretized time delay of the optical self-injection in terms of number of pulses.  $\Gamma(n)$  is a Gaussian distributed random number with a standard deviation of 1.  $W(T(n) - T(n - n_d))$  is a weighting interaction function.

#### 4. Results and discussion

The SML QDh laser  $IBF_0$  amounts to 20.16 GHz with an IBF line width of 110 kHz for a gain current of 200 mA. The corresponding timing phase noise (TPN) power spectral density (PSD) of the radio-frequency beat note for solitary laser operation is depicted in Fig. 3 (red) yielding a  $1/f^2$  dependency. The TPN PSD spectrum for an optical cavity delay length of 73.8 m is shown in Fig. 3 in blue. A reduction to 5.4 kHz is achieved by optical self-injection constituting an improvement by a factor of 20. Simulation results (Fig. 3, green) are in good agreement with the experimental findings. Using shorter optical self-injection lengths leads to larger tuning ranges [4]. For achieving a larger tuning range an optical self-injection length of 6.6 m is considered comparable to the length used in [4]. IBF tuning across 22.5 MHz is obtained (Fig. 4, blue). Simulation results (Fig. 4, green) are in excellent agreement with the experimental findings for this shorter cavity length.

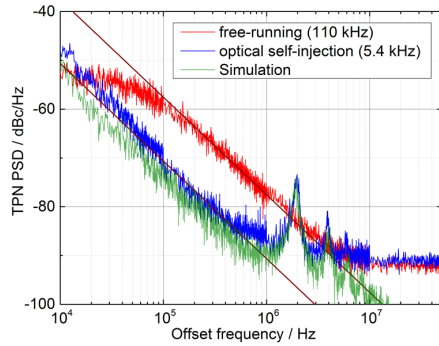


**Figure 3:** TPN PSD spectra for the free-running (red) QDh laser and for an optical self-injection length of 73.8 m (experiment: blue, simulation: green).

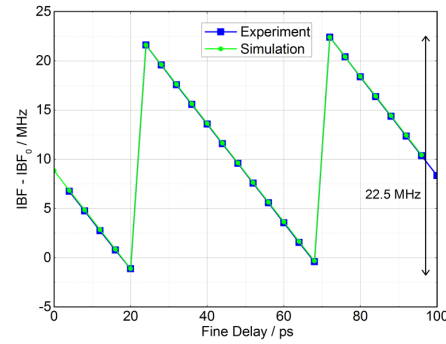


**Figure 4:** Experimental (blue) and modelling (green) results for the IBF in dependence on the fine delay spanning an IBF tuning range of 22.5 MHz.

#### 5. Conclusion

In conclusion, optical self-injection stabilization of a 2 mm long single-section SML frequency comb semiconductor QDh laser is demonstrated. IBF line width reduction to 5.4 kHz is demonstrated for an external cavity length of 73.8 m, which is an improvement by factor 20 in comparison to the solitary laser. IBF tuning across 22.5 MHz is demonstrated for an optical self-injection length of 6.6 m. The experimental results are in excellent agreement with a stochastic model suggesting that single section QDh lasers subject to time-delay control obey the same characteristics as recently demonstrated for PML semiconductor quantum dot and quantum well lasers.

#### 6. References

- [1] R. Rosales et al., "High performance mode locking characteristics of single section quantum dash lasers," *Opt. Express* **20**(8), 8649-8657 (2012)
- [2] L. Drzewietzki et al., "Timing jitter reduction of passively mode-locked semiconductor lasers by self- and external-injection: Numerical description and experiments," *Opt. Express* **21**(13), 16142-16161 (2013)
- [3] D. Auth et al., "Repetition rate control of optical self-injected passively mode-locked quantum-well lasers: experiment and simulation," *Electron. Lett.* **54**(6), 374-376 (2018)
- [4] S. Stutz et al., "Dynamic intermode beat frequency control of an optical frequency comb single section quantum dot laser by dual-cavity optical self-injection," *IEEE Photonics J.* (2019), accepted for publication (DOI: 10.1109/JPHOT.2019.2932452)
- [5] H. Asghar et al., "Stabilization of self-mode-locked quantum dash lasers by symmetric dual-loop optical feedback," *Opt. Express* **26**(4), 4581-4592 (2018)
- [6] Y. Mao et al., "Ultra-low timing jitter of quantum dash semiconductor comb lasers with self-injection feedback locking," *IEEE J. Sel. Top. Quantum Electron.* **25**(6), 1-7 (2019)
- [7] C. Weber et al., "Quantum dash frequency comb laser stabilization by optical self-injection provided by an all-fiber based delay-controlled passive external cavity," *Electron. Lett.* (2019), accepted for publication (DOI: 10.1049/el.2019.2016)
- [8] F. Lelarge et al., "Recent advances on inas/inp quantum dash based semiconductor lasers and optical amplifiers operating at 1.55 $\mu$ m," *IEEE J. Sel. Top. Quantum Electron.* **13**(1), 111-124 (2007)
- [9] F. Kefelian et al., "Rf linewidth in monolithic passively mode-locked semiconductor laser," *IEEE Photonics Technol. Lett.* **20**, 1405-1407 (2008)

# Third Order Dispersion in Optical Time Delayed Systems

C. Schelte<sup>(1,5)</sup>, P. Camelin<sup>(2)</sup>, G. Huyet<sup>(2)</sup>, M. Marconi<sup>(2)</sup>, M. Giudici<sup>(2)</sup>, I. Sagnes<sup>(3)</sup>,  
G. Beaudoin<sup>(3)</sup>, A. Garnache<sup>(4)</sup>, J. Javaloyes<sup>(1)</sup>, S. Gurevich<sup>(5)</sup>

<sup>(1)</sup> *Departament de Física, Universitat de les Illes Balears, C/ Valldemossa km 7.5, 07122 Mallorca, Spain*

<sup>(2)</sup> *Université Côte d'Azur, CNRS, Institut de Physique de Nice, F-06560 Valbonne, France*

<sup>(3)</sup> *Centre de Nanosciences et de Nanotechnologies, C2N UMR 9001, CNRS, Université Paris Sud, Université Paris-Saclay, 91120 Palaiseau, France.*

<sup>(4)</sup> *Institut d'Electronique et des Systèmes, UMR5214, Centre National de la Recherche Scientifique, University of Montpellier, 34000 Montpellier, France*

<sup>(5)</sup> *Institute for Theoretical Physics, University of Münster, Wilhelm-Klemm-Str. 9, 48149 Münster, Germany*

**Abstract:** Time-delayed dynamical systems (DDSs) are widely used in situations where distant nonlinear nodes exchange information that propagates at a finite speed. However, they are considered devoid of dispersive effects, which are known to play a leading role in wave dynamics. Here, we show how dispersion may appear naturally in DDSs and apply our general results to study the influence of third order dispersion in a system composed of coupled optical microcavities. In particular, we show how dispersion-induced pulse satellites emerge and destabilize the mode-locking regime.

Time-delayed dynamical systems (DDSs) describe a large number of phenomena in nature and they exhibit a wealth of dynamical regimes such as e.g., localized structures (LSs) [1], fronts or chimera states. A fertile perspective lies in their interpretation as spatially extended *diffusive* systems which holds in the limit of long delays [2]. A strong limitation of DDSs for this aim comes from the difficulty of taking into consideration chromatic dispersion. As such, DDSs description of wave propagation is limited to low dispersive media and/or narrow-spectrum signals. Nevertheless, chromatic dispersion plays a leading role in many phenomena occurring during wave evolution [3]. Beyond second order dispersion (SOD), third order dispersion (TOD) is the lowest order non-trivial parity symmetry breaking effect, which leads to convective instabilities [4] and drifts.

In this work we show that SOD and TOD appear naturally when modeling a large class of optical DDSs including Vertical External-Cavity Surface-Emitting Lasers (VECSELS), Mode-Locked Integrated External-Cavity Surface Emitting Laser (MIXSELS), laser resonators with intracavity Gires-Tournois etalons, and, more generally, distantly-coupled laser cavities. To illustrate our general result, we focus on a mode-locked VECSEL and we theoretically predict how TOD destabilizes mode-locked pulses [5]. In particular, the passive mode-locking of VECSELS is based upon the dynamics of coupled micro-cavities. We show that the high reflectivity of the bottom mirror in these micro-cavities, combined with strong delayed feedback, induces TOD which generate a peculiar waveform: An infinite sequence of decaying satellites accumulate in front of the pulse leading edge. We show that the unbalanced micro-cavities act as resonant Gires-Tournois interferometers that are a source of third order dispersion inducing the satellites. We predict a new kind of instability for the pulse train in which a satellite may become unstable and grow into a fully developed pulse

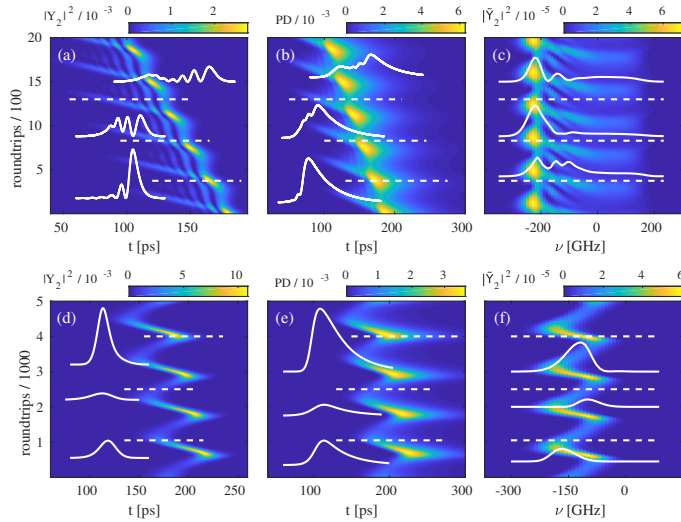


**Fig. 1.** (a,d) Space-time diagrams for the intensity of a passively mode-locked VECSEL. (b,e) Low pass filtered time trace @ 10 GHz in order to emulate finite Photodetector bandwidth. (c,f) Single shot optical spectrum. (a,b,c) and (d,e,f) correspond to two different parameters set, and the satellites pulsating on the front of the pulse can take different shapes as a function of the effective amount of TOD.

which, due to the induced gain depletion, eventually kills the pulse from which it originates, leading to a low frequency quasi-periodic dynamics. Experimental evidences are provided showing good agreement with model predictions.

**References:**

- [1] M. Marconi, et al., "*How Lasing Localized Structures Evolve out of Passive Mode Locking*", Phys. Rev. Lett. **112** (2014), pp. 223901.
- [2] G. Giacomelli et al., "*Relationship between Delayed and Spatially Extended Dynamical Systems*", Phys. Rev. Lett. **76** (1996), pp. 2686
- [3] A. Pimenov et al. "*Dispersive Time-Delay Dynamical Systems*", Phys. Rev. Lett. **118** (2017), pp. 193901.
- [4] F. Leo et al., "*Nonlinear Symmetry Breaking Induced by TOD in Optical Fiber Cavities*", Phys. Rev. Lett. **110** (2013), pp. 104103.
- [5] C. Schelte et al., "*Third Order Dispersion in Time-Delayed Systems*", Phys. Rev. Lett. **123** (2019), pp. 043902.

# 30 GHz and 45 Gbps with $\phi \sim 7.5 \mu\text{m}$ VCSELs

N. Haghighi,<sup>1\*</sup> P. Moser,<sup>1</sup> M. Zorn,<sup>2</sup> and J. A. Lott<sup>1</sup>

<sup>1</sup>Institute of Solid-State Physics and Center of Nanophotonics, Technische Universität Berlin, Hardenberg-Strasse 36, D-10623 Berlin, Federal Republic of Germany

<sup>2</sup>JENOPTIK Optical Systems GmbH, Max-Planck-Strasse 2, D-12489 Berlin, Federal Republic of Germany  
\*nasibeh.haghighi@tu-berlin.de

**Abstract:** Vertical-cavity surface-emitting lasers (VCSELs) emitting at 980 nm with a reduced number of top distributed Bragg reflector periods for higher than typical optical output power and with moderately large oxide aperture diameters of 7.5  $\mu\text{m}$  exhibit a record small-signal modulation bandwidth of 30 GHz and operate error free at 45 Gbps in back-to-back data transmission tests at room temperature.

## 1. Motivation and experiment

Emerging consumer applications for vertical-cavity surface-emitting lasers (VCSELs) include sensing and energy-efficient, free-space optical (FSO) communication. For line-of-sight FSO data transfer over short distances of 1s to 100s of meters we desire very low cost, compact, and eye safe laser sources capable of sending data at 10 Gbps at present to well over 50 Gbps in the near future at optical powers of  $\sim$ 1s to 100s of milliwatts. We investigate the performance of state-of-the-art VCSELs [1]-[3] for short-reach FSO applications by characterizing the static and high frequency performance of single 980 nm VCSELs.

We use a simplified, oxide aperture, multiple InGaAs quantum well VCSEL epitaxial design grown by metal-organic vapor phase epitaxy on 3-inch diameter GaAs substrates as described in [1] and [4]. The top AlGaAs distributed Bragg reflector coupling mirror has a power reflectance of  $R \sim 0.99$  (compared to the more typical  $R \sim 0.994$  to 0.996) to increase the optical output power at the expense of lower damping and a shorter cavity photon lifetime. We process quarter-wafer pieces into double-mesa VCSELs that are planarized using photosensitive BCB (bisbenzocyclohexene) and that are configured with top surface ground-signal-ground (GSG) high frequency metal pads for standard on-wafer probing at room temperature (RT) without heat sinking.

## 2. Results

In Fig. 1 we show the static LIV (light optical output power-current-voltage) characteristics of a VCSEL with an oxide aperture diameter ( $\phi$ ) of 7.5  $\mu\text{m}$ . The threshold current is 0.38 mA, the threshold voltage is 1.59 V, and the peak optical output power at LI rollover is 9.49 mW at a bias current of  $I = 13.05$  mA. The maximum LI differential slope is 0.97 W/A, while the maximum wall plug efficiency is 36.8% at  $I = 1.8$  mA. In Fig. 2 we show the emission spectra at  $I = 7$  mA. The multiple mode emission has a center wavelength of 986.05 nm with a spectral width of 0.87 nm. Next in Fig. 3 we show the small-signal modulation frequency response at  $I = 7$  mA where we achieve a -3 dB bandwidth ( $f_{3dB}$ ) of  $\sim$ 30.2 GHz. In Fig. 4 we plot  $f_{3dB}$  versus  $I$ , and the LI curve from Fig. 1. We measure the  $|S_{21}|$  frequency response using both a cleaved-end OM3 multiple mode optical fiber (MMF) and an OM3 MMF terminated with a lens with a focal length of 150  $\mu\text{m}$  and a spot size of 30  $\mu\text{m}$ . The maximum  $f_{3dB}$  is about 30 GHz. Finally, in Fig. 5 we show bit error ratio (BER) test data at 20 and 45 Gbps and the example corresponding optical eyes. We achieve a BER  $< 1E-12$  at a record 45 Gbps with  $I = 10$  mA.

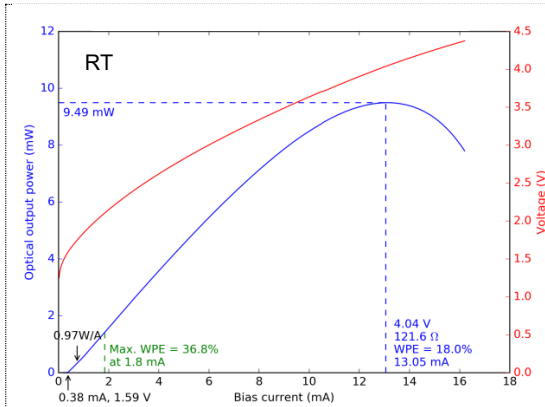


**Figure 1:** LIV characteristic of a  $\phi \sim 7.5 \mu\text{m}$  980 nm VCSEL at room temperature (RT).

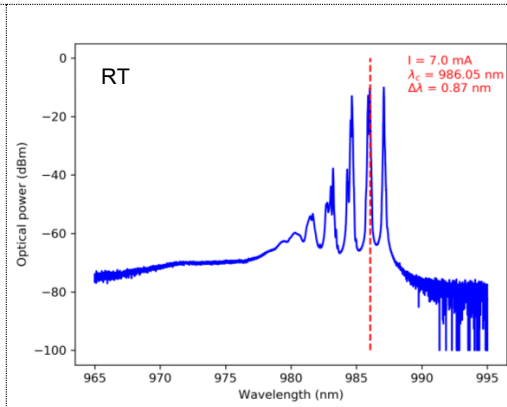


**Figure 2:** Emission spectrum of a  $\phi \sim 7.5 \mu\text{m}$  980 nm VCSEL at a CW bias current of 7 mA.

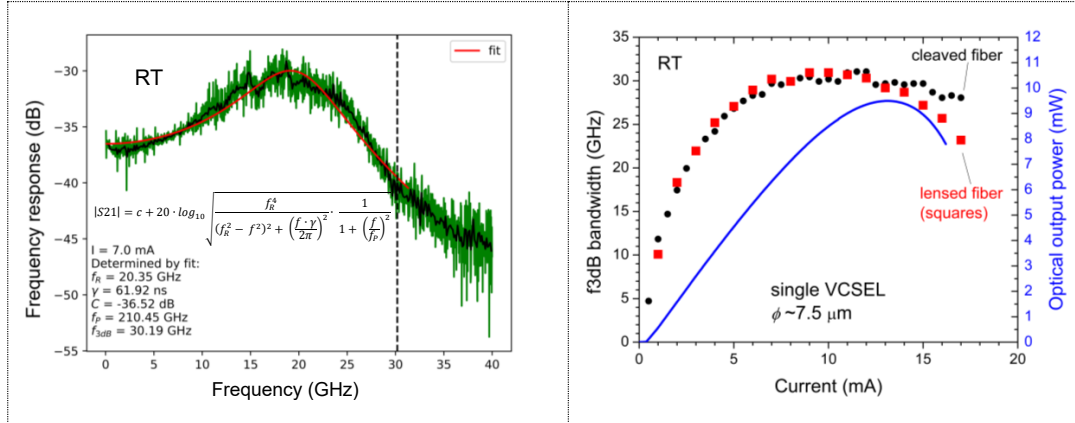


**Figure 3:** Small-signal modulation frequency response [S21] of a  $\phi \sim 7.5 \mu\text{m}$  980 nm VCSEL at RT (green, raw data corrected for the photodiode response; black, smoothed green data; red, curve fit). The VCSEL is biased at 7 mA.

**Figure 4:** Optical output power (right y-axis) versus CW bias current (I), and -3 dB bandwidth frequency versus I (left y-axis) at RT. The light emission is collected by a lensed or cleaved-end optical fiber.

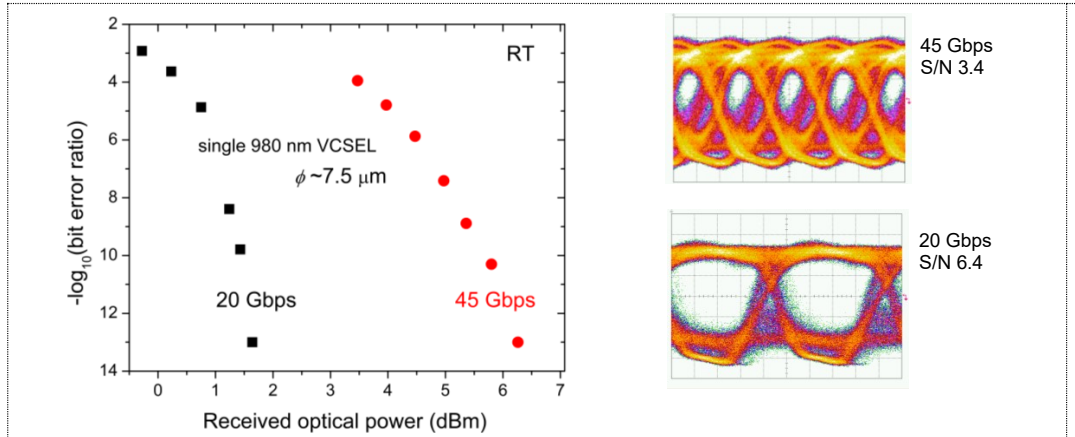


**Figure 5:** Bit error ratio (BER) versus received optical power for back-to-back (across  $\sim 1$  m of OMI optical fiber) data transmission at bit rates of 20 and 45 Gbps at RT (left), and inverted optical eyes at the lowest BERs (right), for standard NRZ (2-level pulse amplitude modulation) with a pseudorandom binary sequence of word length  $2^7-1$ .

### 3. Conclusion

For emerging ubiquitous sensing and communication applications that require both moderate to high optical output power and moderate to high error free data transmission rates, we believe comparative studies of the performance of single VCSELs versus the performance of small VCSEL arrays for the given applications will lead to better designs for both laser configurations.

### 4. References

- [1] N. Haghighi, P. Moser, and J. A. Lott, "Power, bandwidth, and efficiency of single VCSELs and small VCSEL arrays," *IEEE Journal of Selected Topics in Quantum Electronics*, vol. 25, no. 6, pp. 1700615 1-15 (November/December 2019).
- [2] N. Haghighi, *et al.*, "23 GHz bandwidth and 25 mW peak optical output power with 980 nm oxide aperture VCSELs," MC2.4, *Proc. IEEE Photonics Conference*, Reston, Virginia, USA (30 September-04 October 2018).
- [3] N. Haghighi, *et al.*, "55 Gbps error free data transmission with 980 nm VCSELs across 100 m of multiple-mode optical fiber," TuE3-3, *Proc. 24th OptoElectronic and Communications Conference (OECC)*, Fukuoka, Japan (07-11 July 2019).
- [4] J. A. Lott, *et al.*, "High bandwidth simplicity VCSELs," paper 6, *Proc. International Conference on Photonics (ICP)*, Langkawi, Malaysia (09-11 April 2018).

# Modelling the Effect of Dislocations in III-V Lasers on Si

C. Hantschmann<sup>1\*</sup>, Z. Liu<sup>2</sup>, M.C. Tang<sup>2</sup>, A.J. Seeds<sup>2</sup>, H.Y. Liu<sup>2</sup>, I.H. White<sup>1,3</sup>, and R.V. Penty<sup>1</sup>

<sup>1</sup>Centre for Photonic Systems, Department of Engineering, University of Cambridge, 9 JJ Thomson Ave, Cambridge CB3 0FA, UK

<sup>2</sup>Department of Electronic and Electrical Engineering, University College London, WC1E 7JE, UK

<sup>3</sup>University of Bath, Bath BA2 7AY, UK

\*cb893@cam.ac.uk

**Abstract:** We present an approach to modelling III-V lasers on Si based on a rate equation travelling-wave model with sub-micrometer resolution, which allows spatially resolved inclusion of dislocations. The simulations offer new insights into the physical mechanisms responsible for the threshold increase and slope reduction observed at high dislocation densities. In particular, we investigate the effects of carrier diffusion with respect to carrier loss and the local gain reduction and their role in quantum well and quantum dot structures.

## 1. Introduction

The monolithic integration of III-V lasers on Si is of interest due to the prospect of merging high optical gain materials with Si photonics. After numerous attempts of growing GaAs quantum well (QW) lasers on Si, InAs/GaAs quantum dots (QDs) have established themselves as the gain medium of choice due to their higher tolerance to dislocations resulting from the high lattice mismatch between the Si substrate and the III-V material. Yet despite considerable advances in the optimization of defect filter layers, none of the groups growing high-quality QD lasers on Si have succeeded in demonstrating a Si-based QW laser [1], [2]. Here we present an approach to simulating such devices on Si using a rate equation travelling-wave model with high spatial resolution enabling the inclusion of individual dislocations. The objective of this work is to identify key mechanisms responsible for the performance drop typically observed at dislocation densities  $\geq 10^6 \text{ cm}^{-2}$  with a special focus on the limitations QW structures experience.

## 2. Numerical model and implementation of dislocations

The rate equation travelling-wave model includes two levels representing the QWs and the barrier layers (BLs) for QW devices and two additional levels for the QD ground state and first excited state. The forward and reverse electric field travelling-wave equations allow one-dimensional spatial resolution along the longitudinal direction. Details can be found in [3] and [4]. Since a model using effective laser parameters, for instance an overall reduced nonradiative lifetime accounting for dislocations in the active region, is not entirely able to describe the physics of III-V lasers on Si accurately, the spatial step size  $\Delta z$  is reduced to the sub-micrometer level:  $\Delta z = 500 \text{ nm}$  offers a good trade-off between physical accuracy and computational feasibility. It should be noted that transverse effects are neglected, which is why a maximum laser width of  $2 \mu\text{m}$  is chosen for all simulations to ensure single transverse mode operation.

Dislocations are placed on a regular grid along the laser cavity, modelled as sections with ultrafast carrier loss to represent fast carrier capture into these defect states. The exact dislocation carrier capture time  $\tau_{dis}$  is not known, so a  $\sim$  picosecond capture time comparable with the one into QDs is assumed. Since the radius of an actual dislocation core is only a few tens of nanometers, varying  $\tau_{dis}$  is a means of compensating for larger  $\Delta z$ , which overestimate the dislocation size slightly. For  $\Delta z = 500 \text{ nm}$ ,  $\tau_{dis} = 10 \text{ ps}$  is chosen here. Fig. 1(a) shows the QW carrier density obtained for a dislocation density  $\rho_{dis} = 10^6 \text{ cm}^{-2}$ , equating to ten dislocations in a  $2 \times 500 \mu\text{m}^2$  laser. It can be seen that carrier loss occurs not only directly at dislocations, but also in their vicinity, where the

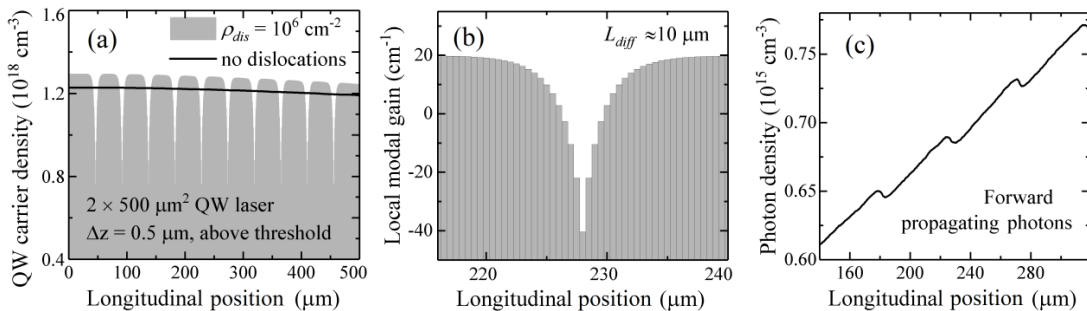


**Figure 1:** (a) QW carrier density versus the longitudinal position in the presence of ten dislocations in comparison with the carrier density level without dislocations. (b) Inset of the corresponding local gain profile around a dislocation. (c) Impact of regions with reduced gain on the amplification of the forward travelling photon density.

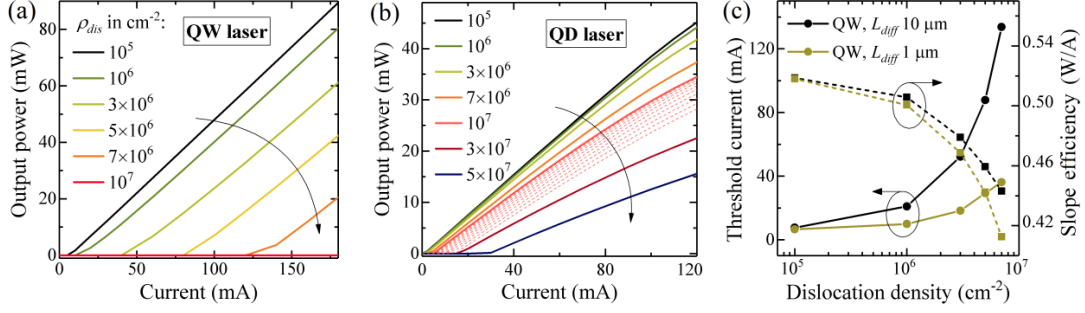


**Figure 2:** Simulated  $LI$  curves of a  $2 \times 500 \mu\text{m}^2$  (a) QW and (b) QD laser (HR-coated rear facets) for various  $\rho_{dis}$ . The dashed curves at  $10^7 \text{ cm}^{-2}$  in (b) indicate the performance variation if 0% (identical with solid curve) to 100% of all dislocations hit a QD. (c) QW threshold current and slope efficiency versus  $\rho_{dis}$  for different  $L_{diff}$ .

diffusion term  $-D\nabla^2 N_{QW}$  allows carriers to migrate into those defects. Since the carrier density in these regions drops below the threshold value, the carrier density in dislocation-free regions must be increased in order to attain the required cavity threshold gain. This is reflected in the gain profile around a dislocation, as shown in Fig. 1(b). Due to the logarithmic nature of the QW gain function, carrier-depleted regions are highly absorptive. Accordingly, the increase in photon density experiences a slight drop in these regions, as depicted in Fig. 1(c).

### 3. Key findings and discussion

Figs. 2(a) and (b) show results of simulated QW and QD  $LI$  curves respectively at different  $\rho_{dis}$ , confirming the experimentally observed trends of increased threshold currents and, in the case of QDs, a reduced slope. While the carrier lifetime reduction is a well-known mechanism for shifting the threshold towards higher currents, the simulations with spatially resolved dislocations show that this effect becomes particularly pronounced with rising  $\rho_{dis}$ , where diffusion-assisted carrier loss in defect-free regions becomes more and more likely. The reduced  $LI$  slope originates in the local gain reduction and thus reduction in the build-up of the photon density along the cavity, as shown in Figs. 1(b) and (c). Although very short ( $\sim$ ps) nonradiative BL and WL lifetimes result effectively in a reduced current injection efficiency and thus also contribute to a smaller slope, the impact of the local gain drop is an effect we are not able to observe when modelling Si-based lasers using effective parameters.

While there are no systematic studies for QW lasers on Si concerning the dependence of the  $LI$  slope on  $\rho_{dis}$ , it can clearly be seen that the modelled QW laser suffers from a larger threshold increase than its QD counterpart. The key reason for this is that carrier diffusion into defects is greatly enhanced for QWs. The QWs in a dot-in-a-well active region, in contrast, have naturally a small diffusion length due to the rapid carrier capture into QDs, where the carriers are laterally confined. This is reflected in our simulations and is additionally confirmed by modelling QW structures at different  $L_{diff}$ . As shown in Fig. 2(c), the QW threshold current increase with  $\rho_{dis}$  is substantially reduced at  $L_{diff} = 1 \mu\text{m}$ , because the number of carriers affected by diffusion-assisted carrier loss is reduced as well. The simulations indicate, however, also that this comes at the expense of a slight slope reduction, as carrier loss in a more concentrated region seems to introduce a sharper drop in the local gain.

### 4. Conclusion

By using a rate equation travelling-wave model with high spatial resolution, we have theoretically analysed how individual dislocations affect the performance of GaAs-based III-V lasers grown on Si. Our simulations show in detail how diffusion-assisted carrier loss into dislocations and the corresponding reduction in local gain impact the  $LI$  performance and confirm experimentally observed trends. In explaining how the performance of III-V QW lasers on Si is being limited by diffusion-assisted excess carrier loss, we hope to open new pathways to be explored in order to make both monolithic QD and QW lasers accessible to future Si photonics applications.

### 5. References

- [1] A.Y. Liu, S. Srinivasan, J. Norman, A. C. Gossard, and J. E. Bowers, "Quantum dot lasers for silicon photonics," *Photonics Res.*, vol. 3, no. 5, pp. B1-B9 (2015).
- [2] Z. Liu, C. Hantschmann, M. Tang, Y. Lu, J.-S. Park, M. Liao, et al., "Origin of defect tolerance in InAs/GaAs quantum dot lasers grown on silicon," *J. Lightw. Technol.*, published online (2019).
- [3] C. Hantschmann, P. P. Vasil'ev, A. Wonfor, S. Chen, M. Liao, A.J. Seeds, et al., "Understanding the bandwidth limitations in monolithic  $1.3 \mu\text{m}$  InAs/GaAs quantum dot lasers on silicon," *J. Lightw. Technol.*, vol. 37, no. 3, pp. 959-955 (2018).
- [4] K.A. Williams, M.G. Thompson, and I.H. White, "Long-wavelength monolithic mode-locked diode lasers," *New J. Phys.*, vol. 6, no. 1, pp. 179 (2004).

# On-chip Photonic Delay-based Reservoir Computing

K. Harkhoe<sup>1\*</sup>, G. Verschaffelt<sup>1</sup>, A. Katumba<sup>2</sup>, P. Bienstman<sup>2</sup>, J. Pauwels<sup>1,3</sup>, S. Massar<sup>3</sup>, G. Van der Sande<sup>1</sup>

<sup>1</sup> Applied Physics Research Group, Vrije Universiteit Brussel, Pleinlaan 2, 1050 Brussel, Belgium

<sup>2</sup> Photonics Research Group, Department of Information Technology, Ghent University-IMEC, Technologiepark Zwijnaarde 126, 9052 Ghent, Belgium

<sup>3</sup> Laboratoire d'Information Quantique, Université libre de Bruxelles, 1050 Brussel, Belgium

\*kharkhoe@vub.be

**Abstract:** We study the performance of a reservoir computing system based on a semiconductor laser with delayed optical feedback fully integrated on an InP-based photonic chip fabricated on the Jeppix platform using standard building blocks. We benchmark the reservoir using a timeseries forecasting task and study the memory capacity of the reservoir. This on-chip reservoir computing system reaches processing speeds of 0.9GSa/s with comparable performances as obtained by other non-integrated RC setups based on delayed feedback. We propose several postprocessing schemes to improve the performance of the RC setup.

## 1 Introduction

The concept of reservoir computing (RC), a paradigm within neuromorphic computing, offers a framework to exploit the transient dynamics within a recurrent neural network for performing useful computation. It has been demonstrated to have state-of-the-art performance for a range of tasks that are notoriously hard to solve by algorithmic approaches, e.g., speech and pattern recognition and nonlinear control. RC rekindled neuromorphic computing activities in photonics [1]. Today, multiple photonic RC systems show great promise for providing a practical yet powerful hardware substrate for neuromorphic computing. Not all reservoirs are neural networks, i.e. based on discrete nonlinear optical nodes (neurons). Any high dimensional nonlinear dynamical system can be exploited for RC. The concept of delay line-based RC, using only a single nonlinear node with delayed feedback, was introduced some years ago by Appeltant et al. [2] as a means of minimizing the expected hardware complexity in photonic systems. Several performant optical systems [1] followed quickly, one of which based on a semiconductor laser with external optical feedback [3].

## 2. Model description, experimental setup

Delay-based RC offers a simple technological route to implement photonic neuromorphic computation. In contrast with neural networks, the neurons or nodes in delay-based RC are time-multiplexed, meaning that a single node will nonlinearly transform the input data to a high dimensional temporal state space. In our setup this single node is a semiconductor laser subjected to delayed feedback, with the delay time being the limiting factor towards reaching high computation speeds. As most optical setups end up to be bulky employing long fiber loops or free-space optics, the processing speeds are limited in the range of kSa/s to tens of MSa/s.

In this work, we focus on external cavities which are far shorter than what has been realized before in experiment. We present a reservoir computing setup based on a semiconductor laser with an 10.8cm delay line, both integrated on an active/passive InP photonic chip built on the Jeppix platform [4]. The single mode laser operates around 1550nm with a side mode suppression of larger than 20dB. Figure 1 shows a schematic of the chip, consisting of the laser, two spirals for the delay line, two semiconductor optical amplifiers (SOA1 and SOA2) integrated in the delay line to compensate for the losses as well as tune the feedback strength and lastly a Distributed Bragg Reflector (DBR) mirror to complete the feedback loop. The laser consists of an active section sandwiched between two DBR mirrors, comprising the laser cavity and enabling the tuning of the lasing wavelength. The in- and output waveguides are connected to the chip facet under an angle of 7 degrees to avoid reflections from the side coupled fibers.

The data is multiplied with a mask that has small features of duration  $\theta$ , which is known as the node spacing. The node spacing is chosen such that delay time  $\tau$  equals  $N\theta$ , where  $N$  is the number of nodes. The

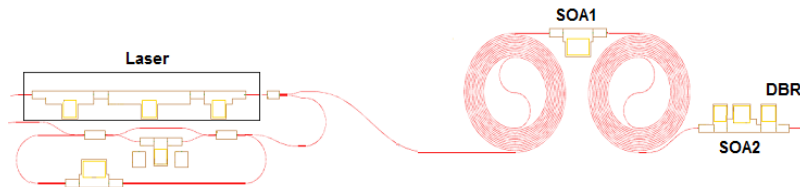


**Figure 1:** Schematics of the integrated photonic chip used in the experiments. A Distributed Bragg Reflector (DBR) laser connected to two consecutive spirals, comprising the delay line. The semiconductor optical amplifiers (SOA) compensate for the losses in the delay line and the DBR on the far right completes the feedback loop. The elements under the laser box are not used in our experiments.

masked data is sent to an arbitrary waveform generator and consequently modulated onto the output of an external tunable laser. The modulated optical signal is coupled into the laser on the chip. The output of the laser is captured with an oscilloscope at 40GSa/s. After which the postprocessing is performed on the computer to obtain the performance. Next to the standard postprocessing scheme with a single-node-value (SNV) per mask-imposed node, we introduced two other schemes: 1) two output nodes per mask-imposed node (double-node-value, DNV) and a postprocessing scheme very similar to DNV, but with nodes from two delay line lengths (double-delay-line, DDL).

The performance is tested by one-step-ahead prediction of a timeseries from the Santa Fe timeseries competition [2]. A three-level mask with 23 nodes separated by 50ps is used, which corresponds to a speed of 0.87GSa/s. The performance is indicated by the Normalized Mean Square Error (NMSE). The NMSE is calculated by an 80-20% split of the data set for training and testing, and the best out of 5-fold cross validation is chosen as the performance of a set.

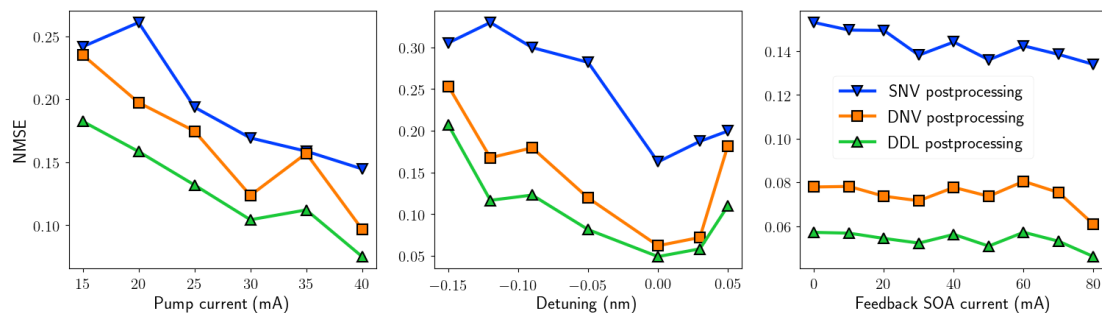
### 3. Results and discussion

We performed experimental sweeps to relate the performance with system parameters in order to find an optimal performant regime. The left plot in figure 2 illustrates how the performance relates to the pump current of the reservoir laser. At higher pump strength the performance improves significantly. In the middle plot we put the injection wavelength is scanned. The lowest NMSE or the best performance is observed at 1549.96nm, at the point where injection locking is achieved. In the right plot we look at the effect of feedback strength. Along the x-axis we have the sum of the currents applied to the two SOAs. We see that the performance generally improves as feedback increases, with some outliers that we attribute to change of feedback phase.

The best experimental NMSEs reached here, is an NMSE of 0.13. Which is in the same range as 0.12 reached by Larger et. al. [5] with an optoelectronic setup with 400 virtual nodes at a processing speed of 48kSa/s. Brunner et al. [3] achieved a prediction error as low as 10.6%, at a speed of 13MSa/s by employing a fiberloop. With our integrated setup we achieve a massive speedup, up to 0.87 GSa/s.

### 4. Conclusion

We demonstrate an integrated photonic delay-based RC setup, which achieves similar performances as previous optoelectronic or discrete component photonic setups. The integrated approach also leads to higher computational speeds due to the shorter node separations, relying on the phase dynamics. The linear/nonlinear memory capacity of the reservoir has also been looked into, but not mentioned in this abstract.



### 5. Related & future work

To further improve performance, we are investigating distributed nonlinear effects in photonic RC schemes. Currently, we employ a delay-based setup implemented in optical fibers, where the Kerr nonlinear effect of the waveguiding material is excited throughout the system's spatial extent. We use this setup to show the advantageous consequences in terms of system complexity and computational capacity for robust and possibly all-optical RC systems.

### 6. References

- [1] G. Van der Sande, et al., "Advances in photonic reservoir computing," in *Nanophotonics* 6(3), 561-576, 2017
- [2] L. Appeltant et al., "Information Processing using a single dynamical node as complex system," in *Nature Communications* 2, 468, 2017
- [3] D. Brunner, et al., "Parallel photonic information processing at gigabyte per second data rates using transient states," in *Nature Communications* 4, 1364, 2013
- [4] X. Leijtens, "Jeppix: the platform for indium phosphide-based photonics," in *IET optoelectronics* 5, 202-206, 2011
- [5] L. Larger, et al., "Photonics information processing beyond Turing: an optoelectronic implementation of reservoir computing," in *Optics Express* 20(3), 3241-3249, 2012

# Spectral Switches in Microwave Oscillation of Semiconductor Laser with Optoelectronic feedback

M. S. Islam,<sup>1,2</sup> G. Coget,<sup>2</sup> A. V. Kovalev,<sup>3</sup> A. Locquet,<sup>1,2,\*</sup> E. A. Viktorov,<sup>3</sup> D. S. Citrin<sup>1,2</sup>

<sup>1</sup>Georgia Tech-CNRS UMI 2958, Georgia Tech Lorraine, 2 Rue Marconi, F-57070 Metz, France.

<sup>2</sup>School of Electrical and Computer Engineering, Georgia Institute of Technology, Atlanta, Georgia 30332-0250, USA.

<sup>3</sup>ITMO University, Birzhovaya Liniya 14, 199034 St. Petersburg, Russia.

\*alocquet@georgiatech-metz.fr

**Abstract:** A semiconductor laser diode subject to optoelectronic feedback is found to exhibit discrete step-wise changes in the relaxation-oscillation frequency when the feedback level is gradually ramped up. The step-wise spectral changes between two limit cycles appear either as an abrupt shift or a progressive transition via a mediating quasiperiodic state. The switches are associated with subcritical Hopf bifurcation between two coexisting attractors as evidenced by the theoretical analysis. Further experimental inquiry demonstrates the presence of hysteresis when the feedback level is ramped down.

## 1. Introduction

Switching events in the relaxation-oscillation frequency ( $f_{RO}$ ) of a semiconductor laser diode (LD) subject to optical feedback is fairly well investigated and associated with subcritical Hopf bifurcation between the attractors around the same external-cavity mode (ECM) [1-4]. Unfortunately, for optoelectronic feedback (where a part of photodetected output is fed-back into the LD injection terminals) similar events are comparatively sparsely explored [5-7]. Although in either case the switches are related with the feedback loop delay ( $\tau$ ) frequency ( $f_{\tau} = \tau^{-1}$ ), the experimental observation and underlying physics in the latter case differs significantly as no ECM exist in optoelectronic feedback. In this report, we analyze the experimental observation of a LD subject to negative optoelectronic feedback with delayed differential equations and a remarkable agreement is found between the two.

## 2. Experimental setup and model description

The LD driven from a regulated current source emits light that is collimated and focused on a photodetector (PD). The photodetected output is amplified in stages and fed-back to the injection terminal using a bias-tee (BT). The feedback level  $\eta$  is controlled optically using a linear polarizer (LP) placed before the PD. The loop delay frequency is experimentally estimated to be 101 MHz whereas the lower cutoff frequency of the loop is set by one of the amplifiers which is 50 MHz. The LD threshold is  $J_{th}=33$  mA and the laser has been operated at  $J \approx 2J_{th}$  all through the experiment.

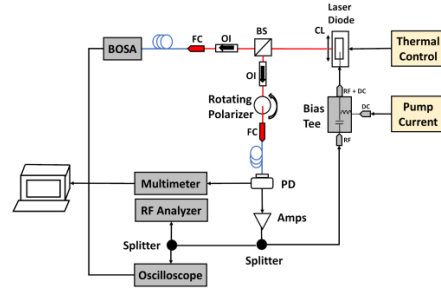


**Figure 1:** Experimental setup. CL: collimating lens, OI: optical isolator, LP: linear polarizer, PD: photodetector, Amps: amplifiers.

We employ a rate-equation model for the LD with optoelectronic filtered feedback based on that in [8]; it consists of the delayed differential equation of normalized electric field intensity  $J(t)$ .

## 3. Results and discussion

Figure 2(a) and (c) presents the experimental bifurcation diagram (BD), and (b) and (d) the RF spectra obtained as a function of  $\eta$  ramping (a), (b) up and (c), (d) and down. The BDs are plotted from the histogram of the local extrema obtained from the photodetected optical intensity  $J(t)$  at each  $\eta$ , whereas the color mapping of the RF spectra illustrates the evolution of  $f_{RO}$ . When  $\eta$  is ramped up, discrete changes in RF frequency corresponding to switching between limit cycles (LCs) occur at  $\eta = 0.52, 0.82,$  and  $0.87$ . The switching events appear at  $\eta = 0.55, 62,$  and  $0.73$  in reverse order when feedback level is ramped down.

Although, the jumps between two LCs are apparent from the discrete changes in the BDs, the RF spectra indicate two qualitatively different types of jumps. To begin with Fig. 2(b), the first jump appears abruptly as a switching from LC1 (6.165 GHz) to LC2 (6.067 GHz) at  $\eta = 0.52$ . The LC2 persists until  $\eta \sim 0.80$ , where another dynamical regime is reached, with the same main RF frequency as in LC2, but numerous strong sidebands

appear in the RF spectrum, corresponding to quasiperiodic (QP) behavior (QP1) as reported in [7]. Thereafter, at  $\eta \sim 0.82$ , we observe a jump to a different LC (LC3) with dominant RF frequency 5.649 GHz. We refer to this jump as a progressive switching event, as the transition does not occur directly between LC regimes. After the jump, for even larger  $\eta$ , LC3 gives way to another mediating QP state (QP2) and finally, for  $\eta \sim 0.87$ , LC4 with RF frequency 5.442 GHz is observed. Ramping  $\eta$  down, Fig. 2(d) displays two abrupt jumps at  $\eta = 0.55$  and  $0.73$  and one progressive jump at  $\eta = 62$ .

We follow the bifurcation sequence with increasing  $\eta$  obtained analytically as shown in Fig. 3. Similar to the experiment, the CW state undergoes a supercritical Hopf bifurcation resulting in a small amplitude stable limit cycle LC1. The cycle grows in amplitude as  $\eta$  increases, and undergoes an abrupt transition to a limit cycle LC2 having a lower frequency. LC1 and LC2 are found to be separated by the feed-back frequency  $f_t$  as was experimentally observed. Thereafter, LC2 develops into a quasiperiodic state QP1 through a supercritical bifurcation, and eventually collapses to the limit cycle LC3. Therefore, QP1 is mediating transition from LC2 and LC3 which is found to be separated by  $\sim 5f_t$ , again very similar to the experiment. Finally, LC3 abruptly switches by  $\sim 2f_t$  to the limit cycle LC4.

#### 4. Conclusion

Two different type of switches between the limit cycles are experimentally observed and analytically discussed in this report. While the progressive jumps are non-integer multiples of the loop delay frequency, the abrupt jumps are found to be equal to either integer or non-integer multiples of the same.

#### 5. References

- [1] J. Mørk, J. Mark, and B. Tromborg, "Route to chaos and competition between relaxation oscillations for a semiconductor laser with optical feedback," *Physical Review Letters*, vol. 65, no. 16, pp. 1999-2002 (1990).
- [2] J. Mørk, B. Tromborg, and J. Mark, "Chaos in semiconductor lasers with optical feedback: theory and experiment," *IEEE Journal of Quantum Electronics*, vol. 28, no. 1, pp. 93-108 (1992).
- [3] A. Ritter and H. Haug, "Theory of the bistable limit cycle behavior of laser diodes induced by weak optical feedback," *IEEE Journal of Quantum Electronics*, vol. 29, no. 4, pp. 1064-1070 (1993).
- [4] D. Pieroux, T. Erneux, T. Luzyanina, and K. Engelborghs, "Interacting pairs of periodic solutions lead to tori in lasers subject to delayed feedback," *Physical Review E*, vol. 63, no. 3, pp. 036211 (2001).
- [5] G. Giacomelli, M. Calzavara, and F. Arecchi, "Instabilities in a semiconductor laser with delayed optoelectronic feedback," *Optics Communications*, vol. 74, no. 1-2, pp. 97-101 (1989).
- [6] C.-H. Lee and S.-Y. Shin, "Self-pulsing, spectral bistability, and chaos in a semiconductor laser diode with optoelectronic feedback," *Applied Physics Letters*, vol. 62, no. 9, pp. 922-924 (1993).
- [7] S. Tang and J. Liu, "Chaotic pulsing and quasi-periodic route to chaos in a semiconductor laser with delayed opto-electronic feedback," *IEEE Journal of Quantum Electronics*, vol. 37, no. 3, pp. 329-336 (2001).
- [8] T. Erneux and P. Glorieux, "Laser Dynamics," (Cambridge University Press, Cambridge, 2010).

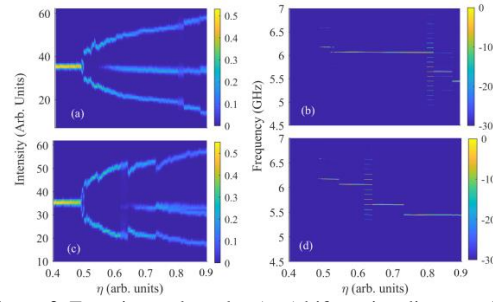


**Figure 2:** Experimental results: (a, c) bifurcation diagram of the extrema (b, d) peak relaxation oscillation frequency when  $\eta$  is ramped up (a, b) and when  $\eta$  is ramped down (c, d).

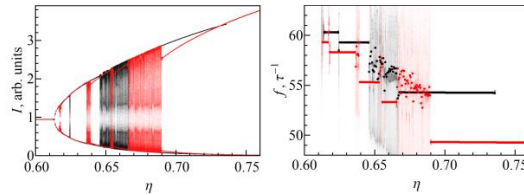


**Figure 3:** Numerical bifurcation diagram obtained by solving the delay differential equation as in Ref. [8] when  $\eta$  is increased (black) and decreased (red). Left panel shows the extrema of intensity, and right panel demonstrates the frequency defined as the inverse of time intervals between two adjacent intensity maxima, where bold dots stand for the average value.

# Polarization dynamics of a VCSEL with thermally tuned birefringence

N. Jung<sup>1\*</sup>, M. Lindemann<sup>1</sup>, P. Stadler<sup>1</sup>, T. Pusch<sup>2</sup>, R. Michalzik<sup>2</sup>, M. R. Hofmann<sup>1</sup>, N. C. Gerhardt<sup>1</sup>

<sup>1</sup>Photonics and Terahertz Technology, Ruhr-University Bochum, 44780 Bochum, Germany

<sup>2</sup>Institute of Functional Nanosystems, Ulm University, 89081 Ulm, Germany

\*Natalie.Jung-b3q@ruhr-uni-bochum.de

**Abstract:** Here we investigate the polarization properties in a VCSEL with thermally tuned birefringence. We measure the Stokes parameters with a Stokes-Polarimeter setup and analyze them depending on the pump and heating current using Fourier transform analysis.

## 1. Introduction

A continuing demand for higher communication bandwidth is the motivation to develop new and innovative optical communication systems [1]. Three-quarters of the total data volume of data centers consist of internal short-haul transmissions [2]. For those short-haul optical connections, current driven and intensity modulated vertical-cavity surface-emitting lasers (VCSELs) are used. The current state of research has reached a maximum modulation bandwidth of around 36GHz [3]. New concepts for bandwidths above 100GHz are needed. Spin-VCSELs, which utilize the spin and polarization instead of current and intensity, are a promising solution to overcome the limitations from their conventional counterparts. Birefringence in spin-VCSELs has a strong influence on the polarization dynamics. Due to birefringence, the orthogonally polarized field components in the resonator experience different refractive indices and therefore emit at different frequencies. The resulting spectral distance of the two orthogonally polarized modes, is called birefringence-induced mode splitting. The mode splitting can be changed by the elasto-optic effect. Recently, polarization dynamics of more than 200GHz have been shown in spin-VCSELs with a birefringence induced by indirect bending [4]. For future applications, solutions directly implemented on the chip are preferred. One approach is to electrically tune the birefringence. For this purpose, an additional heating current is driven through the VCSEL, which results in a maximum birefringence splitting of 79GHz [5].

## 2. Sample description, experimental setup

For our experiments a VCSEL with a keyhole-shaped mesa, fabricated from a standard wafer material for 850nm oxide-confined AlGaAs VCSEL grown by Philips Photonics, was used [5]. Additionally, to the current for laser operation, a heating current is forced into the semiconductor ridge, with which an asymmetric heating gradient can be generated.

A key property of the light emitted by VCSELs is polarization. The polarization state of the emitted light can be effectively characterized by the Stokes parameters. They are measured with a standard Stokes-Polarimeter setup consisting of a rotatable quarter-wave plate, a fixed linear polarizer and a photodetector. The Stokes parameters can then be determined using a Fourier transform analysis [6].

## 3. Results and discussion

Figure 1 shows the normalized Stokes parameters depending on different pump and heating currents. The pump current was varied between the threshold of 0.4mA and 2mA in 0.1mA steps. The heating current was varied between 10mA and 30mA in 0.1mA steps. Higher heating currents are omitted to prevent sample damage. To reduce temperature fluctuations, a waiting time of 10s for the pump current and 30s for the heating current was set.

The VCSEL emits predominantly linearly polarized light, as  $S_3$  equals zero (Fig. 1(d)). Its orientation can change during operation, which is called polarization switching (PS). Various parameters, such as temperature and pump current [7] but also the thermally induced birefringence have an influence on the polarization switching. Operating points at which PS occurs are called PS points. If the pump current exceeds 0.9mA, PS points are indicated by a sign change of the Stokes parameters for linear polarization  $S_1$ .

A proportional relation between  $S_0$  and  $S_1$  can only be examined for a pump current  $<0.9$ mA. A further increase of the pump current results in a horseshoe shaped increase of the total intensity  $S_0$  and a simultaneous decrease of the linear polarization  $S_1$ . The spikes in  $S_2$  (Fig. 1(c)) occur at those points where the PS points in  $S_1$  can be observed.

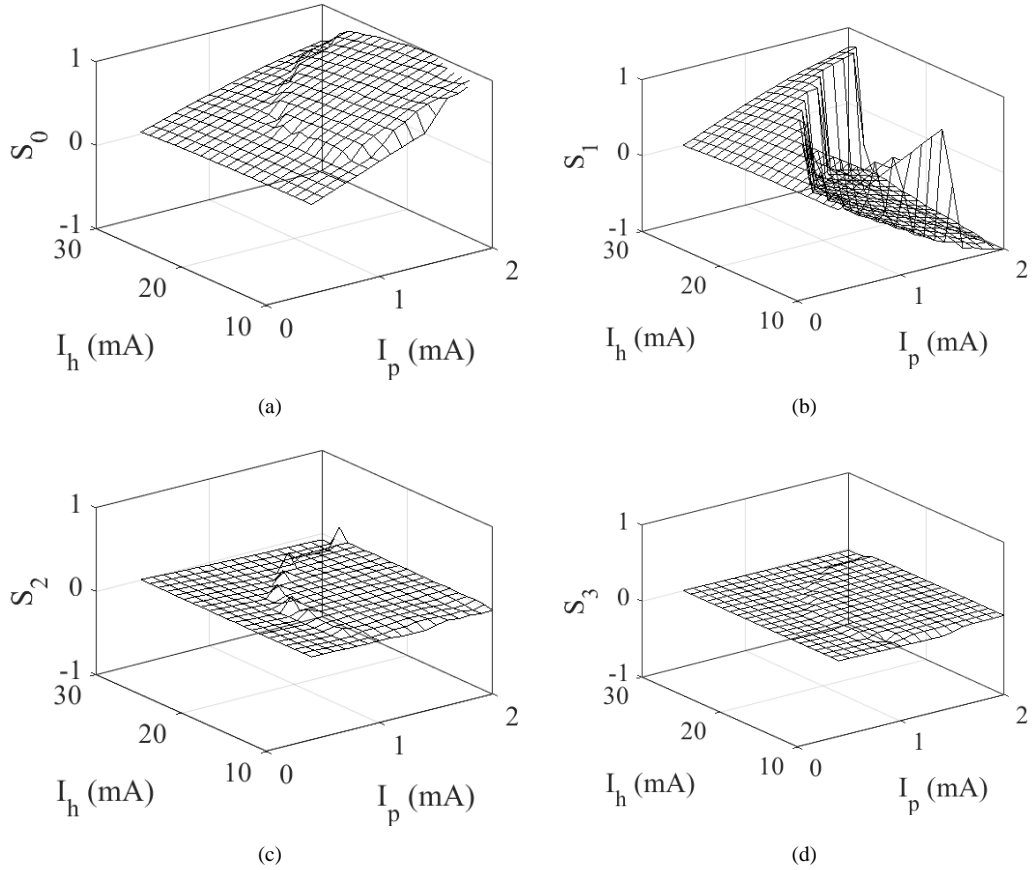


**Figure 1:** Stokes parameter (a)  $S_0$ , (b)  $S_1$ , (c)  $S_2$  and (d)  $S_3$  depending on the pump and heating current in a spin-VCSEL with thermally tuned birefringence.

#### 4. Conclusion

Here, we investigated the polarization state of a VCSEL with thermally induced birefringence. We showed that the polarization switching points depend on the pump as well as the heating current. We were able to identify a set of parameters in which the polarization switching in those samples occur. In future studies, we analyze the ultrafast polarization oscillation dynamics in those different regimes.

#### 5. References

- [1] J. Hecht, "The Bandwidth Bottleneck", *Nature*, vol. 536, no. 7615, pp. 139-142 (2016).
- [2] C. Kachris, and I. Tomkos, "Power consumption evaluation of all-optical data center networks", *Cluster Computing*, vol. 16, no. 3, pp. 611-623 (2013).
- [3] A. Liu, P. Wolf, J. A. Lott, and D. Bimberg, "Vertical-cavity surface-emitting lasers for data communication and sensing", *Photonics Research*, vol. 7, no. 2, pp. 121-136 (2019).
- [4] M. Lindemann, G. Xu, T. Pusch, R. Michalzik, M. R. Hofmann, I. Žutić, and N. C. Gerhardt, "Ultrafast spin-lasers", *Nature*, vol. 568, no. 7751, pp. 212-215 (2019).
- [5] T. Pusch, S. Scherübl, M. Lindemann, N. C. Gerhardt, M. R. Hofmann and R. Michalzik, "Thermally induced birefringence in VCSELs : approaching the limits", *Proceedings of SPIE*, vol. 10682, no. 1068219 (2018).
- [6] H. G. Berry, G. Gabrielse, and A. E. Livingston, "Measurement of the Stokes parameters of light", *Applied Optics*, vol. 16, no. 12, pp. 3200-3205 (1977).
- [7] R. Michalzik (Ed.), "VCSELs : Fundamentals, technology and applications of vertical-cavity surface-emitting lasers", *Springer* (2013).

# Tailoring the Linewidth of Quantum Dot Lasers via the Temperature

F. Köster,<sup>1\*</sup> J. Duan<sup>2</sup>, H. Huang<sup>2</sup>, B. Dong<sup>2</sup>, Z. Lu<sup>3</sup>, P. J. Poole<sup>3</sup>, F. Grillot<sup>2</sup>, K. Lüdge<sup>1</sup>

<sup>1</sup>*Institut for Theoretical Physics, Technische Universität Berlin*

<sup>2</sup>*Télécom Paris, Institut Polytechnique de Paris, France*

<sup>3</sup>*Advanced Electronics and Photonics Research Center, National Research Council Canada, Ottawa, ON, Canada*

\*E-Mail: felix.koester@tu-berlin.de

**Abstract:** We investigate the influence of temperature on the linewidth of an InP quantum dot (QD) laser experimentally and through theoretical modeling. The full width half maximum (FWHM) of the peak in the optical spectrum of the laser emission rebroadens at higher injection levels which is even more pronounced at higher temperatures. We qualitatively reproduce the experimentally observed data with a QD laser rate equation model that includes excited state (ES) and ground state (GS) charge carrier dynamics as well as the detailed balance of in- and out scattering rates. We can show that the temperature-induced increase of the out-scattering processes is the dominating effect for the temperature sensitivity of the linewidth.

## 1 Introduction

For a QD laser the description of the  $\alpha$ -factor is complex and also determined by the charge carrier dynamics of the non-resonant carriers. They contribute to the refractive index of the laser [1] and thus effectively change the  $\alpha$ -factor. It comes from the fact that the carriers populate the 2D reservoir as well as non-active QDs instead of being directly injected into the active laser level. Resulting from this, the  $\alpha$ -factor is as mentioned non-constant in QD lasers, depends on the point of operation and can also be a dynamic, and thus time varying, quantity. Following from this also the linewidth changes with the injection current [2–6], which leads for higher currents to a re-broadening of the linewidth. Previous work [4,7] was successful in modeling this effect by a reduced minimalist approach, however without capturing the influence of the temperature. In this presentation, we investigate the effect of temperature on the linewidth re-broadening in an InP QD laser by including the temperature dependent detailed balance between in- and out charge scattering rates.

## 2. Model description, experimental setup

The QD distributed feedback (DFB) laser studied here has a stripe width of 3  $\mu\text{m}$  and a cavity length of 1 mm. The QD active region contains 5 stacked layers of InAs QDs with 30 nm  $\text{In}_{0.816}\text{Ga}_{0.184}\text{As}_{0.392}\text{P}_{0.608}$  (1.15Q) barriers which was grown by chemical beam epitaxy (CBE) on a (001) oriented n-type InP substrate. Carrier and optical confinement was achieved by embedding the active region in a 350 nm thick 1.15Q waveguiding core.

In order to measure the spectral linewidth of the laser, self-heterodyne fiber interferometer [8] was used, where one part of the laser emission is sent to a 100 MHz frequency-shifted acousto-optic modulator (AOM) and another part propagates through a 25 km fiber coil. To match the polarization between two parts, a polarization controller is also used. At the output of the interferometer the resulting beat note, centered at the AOM frequency, is recorded by an electrical spectrum analyzer through a high-speed photodiode.

For the model of the QD-laser we consider the electrically pumped reservoir  $N(t)$ , which is filled to its quasi Fermi level  $E_F(N)$ , the two occupation probabilities of the ES and GS within the QD  $\rho_{ES}$  and  $\rho_{GS}$ , and the complex electric field  $E(t) = A(t)e^{-i(\omega_L t + \Phi(t))}$ , where  $\omega_L$  is the rotating frame of the laser frequency and  $A(t)$  is the slowly varying amplitude within. The equations are given by

$$\begin{aligned}\dot{N} &= \eta J - \frac{N}{\tau_1} - 4N_{QD}R_{ES}^{cap} - 2N_{QD}R_{GS}^{cap} \\ \dot{\rho}_{ES} &= -\frac{\rho_{ES}}{\tau_{ES}} + R_{ES}^{cap} - \frac{1}{2}R^{rel} \\ \dot{\rho}_{GS} &= -\frac{\rho_{GS}}{\tau_{GS}} + R_{GS}^{cap} + R^{rel} \\ \dot{A} &= g_0(2\rho_{GS} - 1)A - \kappa A + D_{noise}\xi_A \\ \dot{\Phi} &= -g_0(2\rho_{GS} - 1)\alpha_0 - \delta\Omega N + \frac{D_{noise}}{A}\xi_\Phi\end{aligned}$$

Here the total scattering contributions  $R_{ES/GS}^{cap}$  and  $R^{rel}$  are defined as follow

$$R_{ES/GS}^{cap} = S_{ES/GS}^{cap,in} [1 - \rho_{ES/GS} - f_{ES/GS} \cdot \rho_{ES/GS}]$$

$$R^{rel} = S^{rel,in} [(1 - \rho_{GS})\rho_{ES} - \hat{f} \cdot \rho_{GS}(1 - \rho_{ES})]$$

and contain the detailed balance temperature dependent in-and out scattering processes and thus depend on the carrier temperature.  $S_{ES/GS}^{cap,in}$   $S^{rel,in}$  are here the scattering rates between the reservoir, the GS and the ES and  $f_{ES/GS}$   $\hat{f}$  are the corresponding temperature dependent Boltzmann factors.

### 3. Results and discussion

The measured and simulated linewidths as a function of the pump current  $J$  for three different temperatures (293K, 303K and 313K) are depicted in Fig. 1. For all temperatures, a typical linewidth re-broadening is visible [7] even though for 293K the re-broadening effect is hardly visible because the applied currents are not high enough. In [7] the re-broadening was explained by the influence of the gain compression effects. Note, that in this model the gain compression results from the carrier dynamics within the complex gain model rather than being a phenomenological parameter. Comparing the different temperatures the influence of the thermal kinetic energy of the charge carriers leads to a higher linewidth in general and a steeper slope of the re-broadening. The linewidth for 313K for example is higher for all  $J$  and the re-broadening effect starts at lower bias currents  $J$  with an enhanced slope. Looking at the simulation results in Fig. 1(b) this behavior is captured qualitatively very good.

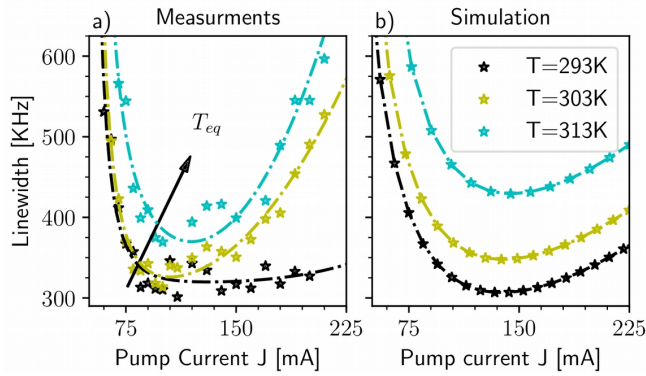


Fig 1: Linewidth of an InP QD laser as a function of the injection current  $J$  for experimental (a) and simulated (b) data. Different colors correspond to different temperatures (293K, 303K and 313K).

### 4. Conclusion

We show that the temperature has a strong impact on the emission of a QD laser as it increases the

linewidth and enlarges the re-broadening effect. It can be nicely described with a microscopically motivated model which includes the charge carrier dynamics. We have pointed out that the correct description of in- and out-scattering processes via the temperature dependent detailed balance relation is a crucial ingredient. Experimental data obtained on an InP based QD laser agree with results and support our conclusion that for the temperature sensitivity of the linewidth, the complex carrier dynamics have to be considered.

### 5. References

- [1] M. Osinski and J. Buus, IEEE J. Quantum Electron. **23**, 9–29, 1987.
- [2] B. Lingnau, K. Lüdge, W. W. Chow, and E. Schöll, Phys. Rev. E **86**, 065201(R), 2012.
- [3] B. Lingnau, W. W. Chow, and K. Lüdge, Opt. Express **22**, 4867–4879, 2014.
- [4] S. Melnik, G. Huyet, and A. V. Uskov, Opt. Express **14**, 2950–2955, 2006.
- [5] M. Gioannini, A. Sevega, and I. Montrosset, Opt. Quantum Electron. **38**, 381–394, 2006.
- [6] F. Grillot, B. Dagens, J.-G. Provost, H. Su, and L. F. Lester, IEEE Journal of Quantum Electronics **44**, 946–951, 2008.
- [7] C. Redlich, B. Lingnau, H. Huang, R. Raghunathan, K. Schires, P. J. Poole, F. Grillot, and K. Lüdge, IEEE J. Sel. Top. Quantum Electron. **23**, 1901110, 2017.
- [8] J. Duan, H. Huang, Z.G. Lu, P.J. Poole, C. Wang, and F. Grillot, Appl. Phys. Lett. **112**, 121102, 2018.

# Multimode Dynamics of Long-Cavity Fabry-Pérot Quantum-Dot Lasers

B. Lingnau,<sup>1,2\*</sup> James O'Callaghan<sup>2</sup>, B. Corbett<sup>2</sup>, B. Kelleher<sup>1,2</sup>

<sup>1</sup>Department of Physics, University College Cork, Ireland

<sup>2</sup>Tyndall National Institute, Cork, Ireland

\*benjamin.lingnau@ucc.ie

**Abstract:** We investigate the multimode dynamics of long Fabry-Pérot (FP) cavity quantum-dot (QD) lasers in simulations and experiment. Due to strong spatial hole burning (SHB) in the active medium, QD lasers show pronounced multimode dynamics. We characterise the multimode dynamics of the free-running laser as well as under external optical injection, and analyse the behaviour of the SHB in the charge-carrier distribution in the different setups. In the injected laser, we focus on the transition between the locking regions of neighbouring FP modes, which could not be described using traditional multimode rate-equation models, and highlight the differences compared to optically injected single-mode lasers.

## 1. Introduction

Multimode semiconductor lasers have received relatively little attention in the context of laser dynamics in the past, owing to the dynamical complexity introduced by the interplay of a large number of laser modes [1]. This dynamical complexity emerges when the laser is free-running but can also influence the dynamics in typical setups such as optical injection. Quantum-dot (QD) lasers show pronounced multimode dynamics due to their strong spatial hole burning (SHB) [2]. A thorough investigation of the multimode dynamics in QD lasers is thus required.

Conventional multimode rate equation models usually rely on the a-priori separation of the laser field into different modes. Such models cannot describe the direct interaction between neighbouring modes when their dynamics occurs on similar frequencies as the mode spacing. We therefore derive a multimode laser model which describes the electric field dynamics in a single variable, comprising all laser modes. We use this model to characterise the multimode dynamics of a long-cavity Fabry-Pérot (FP) QD laser both when free-running and under optical injection, and compare the results with measurements of the laser dynamics in the respective setups.

## 2. Laser model and experimental setup

We employ a numerical delay-differential equation (DDE) model, based on the separation of the laser cavity into a small number of longitudinal sections [3]. The electric field propagation is governed by the propagation delay between these sections. We expand the occupation probability of the QD active medium within each longitudinal section  $k$  in terms of its Fourier coefficients,

$$\rho_k(z, t) = \rho_k^{(0)}(t) + 2 \operatorname{Re}[\rho_k^{(2)}(t) e^{2ikz}],$$

describing the carrier grating induced by the standing wave within the cavity [4]. The QD laser device we investigate is a 4.5 mm long FP cavity laser with a nominal emission wavelength of 1.3  $\mu\text{m}$ , and a mode spacing of 8.9 GHz. We measure the optical properties of this device using an optical spectrum analyser and a high-speed photodiode and oscilloscope.

## 3. Results and discussion

The characterisation of the free-running laser is shown in Fig. 1. The laser reaches its threshold at a pump current of 30 mA, with the number of lasing modes steadily increasing with higher pump currents, reaching 102 lasing modes (within -10 dB of the strongest mode) at a pump current of 90 mA. The individual modes exhibit a small red-shift with increasing current due to heating of the laser cavity. Additionally, the envelope of the lasing modes shows a strong red-shift, which can be explained by the band-gap shrinkage and Varshni shift with increasing charge-carrier density and temperature. The experimental spectra furthermore show an underlying fine structure, which we attribute to minor structural asymmetries or defects in the cavity. The simulations do not take into account the overall red-shift of the spectrum, but reproduce the increase in the spectral envelope very well. Note that we plot only the spectral peak envelope, neglecting the spectral valleys between modes for legibility. The spectrum is slightly asymmetric, favouring the modes at longer wavelengths due to the phase-amplitude coupling of the semiconductor medium.

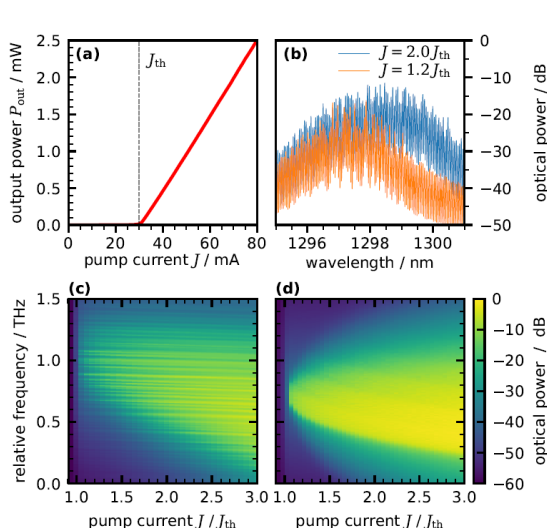


**Figure 1:** Free-running FP laser characterisation. (a) Fibre-coupled output power vs pump current. (b) Optical spectra at pump currents of 36 mA (orange) and 60 mA (blue). (c) Measured and (d) simulated optical spectra (color-coded) as a function of the pump current. For legibility, only the spectral peak values are shown, not resolving the spectral valley between modes.

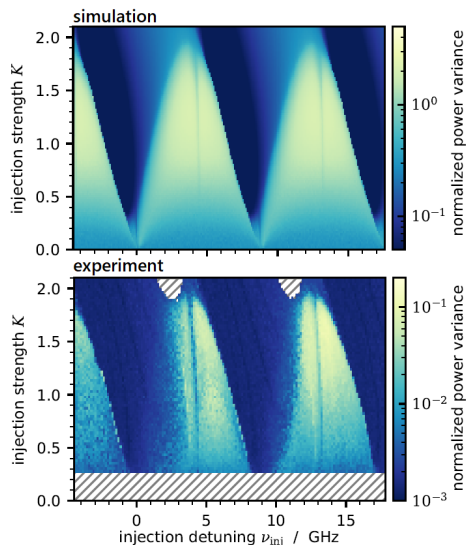


**Figure 2:** Two-dimensional parameter sweeps of the normalised power variance under optical injection, in dependence of the injection strength,  $K$ , and the detuning frequency,  $\nu_{\text{inj}}$ . No measurement was possible in the hatched regions. The laser was biased at 36 mA. The power variance is low when the laser output is nearly constant and high for fluctuating output.

Next, the dynamics under optical injection is investigated. Depending on the wavelength of the monochromatic injected light of the master laser, individual FP modes become phase-locked. We evaluate the normalised power variance in dependence on the injection strength,  $K$ , and the detuning frequency,  $\nu_{\text{inj}}$ , as shown in Fig. 2. We observe individual locking regions for each cavity mode, which overlap for strong injection. In between locking tongues, the laser is unlocked and the dynamics becomes complex due to the multitude of lasing modes. The parameter space can be divided into different regions, dominated by the interaction of the injected signal with the respective closest lasing mode. These regions are bounded by thin regions of reduced dynamic complexity (at  $\nu_{\text{inj}} \approx 4$  GHz and  $\nu_{\text{inj}} \approx 13$  GHz). The SHB in the injected laser leads to a minimum injection strength required to suppress the non-injected lasing modes, as can be seen in Fig. 2(a) for  $K < 0.3$ . For lower injected power, the injected mode is phase-locked while the laser emission remains multimode. Our laser model reveals this to be caused by a dynamically changing magnitude of the carrier grating induced by SHB.

#### 4. Conclusion

In conclusion, we have investigated the multimode dynamics of a long-cavity QD laser. We have formulated a DDE model to describe the laser dynamics and overcome the limitations of conventional multimode rate equation models. The model furthermore allows a direct insight into the spatial dependence of the SHB-induced carrier grating. We identify differences in the locking behaviour compared to optically injected single-mode lasers. The strong SHB introduces a minimum injection strength to fully suppress the non-injected modes when locking a given laser mode. Potential extensions of the work could include a further reduction of the model towards a spatially-averaged model to investigate the bifurcation structure when the laser is injected in between two neighbouring laser modes.

#### 5. References

- [1] M. Ahmed and M. Yamada, IEEE J. Quantum Electron. **38**, 682 (2002).
- [2] M. Giovannini, P. Bardella, and I. Montrosset, IEEE J. Sel. Top. Quantum Electron. **21**, 1900811 (2015).
- [3] S. Meinecke, L. Drzewietzki, C. Weber, B. Lingnau, S. Breuer, and K. Lüdge, Sci. Rep. **9**, 1783 (2019).
- [4] P. Bardella, L. Columbo, and M. Giovannini, Opt. Express **25**, 26234 (2017)

# Temperature Distribution Analysis of Multi-Section Slotted Semiconductor Lasers

Robert McKenna<sup>1\*</sup>, Sepideh T. Naimi<sup>1,3,4</sup>, Simon Corbett<sup>1</sup>, David McCloskey<sup>1,3,4</sup>,  
and John F. Donegan<sup>1,2,3,4</sup>

<sup>1</sup> School of Physics, Trinity College Dublin, Ireland

<sup>2</sup> Future Networks and Communications (CONNECT), Trinity College Dublin, Ireland

<sup>3</sup> Centre for Research on Adaptive Nanostructures and Nanodevices (CRANN), Trinity College Dublin, Ireland

<sup>4</sup> Advanced Materials and BioEngineering Centre (AMBER), Trinity College Dublin, Ireland

\* [mckennr2@tcd.ie](mailto:mckennr2@tcd.ie)

**Abstract:** An experimental study of the temperature distribution of a two section slotted laser during its operation is undertaken in this work. High resolution thermal images of the laser are measured by means of CCD-TR microscopy. The temperature distribution along laser cavity is provided.

## 1. Introduction

Semiconductor lasers comprise an integral part of the global communication network. The immense growth in data traffic in recent years has necessitated the drive towards low cost, high performance and energy efficient optical components. The self-heating of semiconductor lasers during operation leads to a number of negative consequences. The laser wavelength is sensitive to the temperature of the laser cavity, which for InP based QW 1550 nm lasers is typically on the order of 0.1 nm/K. Thus, dense wavelength division multiplexing (DWDM), for which the channel spacing can be less than 0.4 nm (50 GHz) requires active cooling of the laser diode. High temperatures also lead to a large increases in non-radiative recombination leading to low output power. Efforts to engineer the laser structure to minimize temperature excursions require knowledge of the laser temperature. Wavelength drift can provide the spatially averaged temperature of the laser cavity, however it does not provide the temperature distribution. Recently, CCD-TR microscopy has been demonstrated to provide high resolution measurements of the thermal distribution of semiconductor lasers. [1][2] In this work we provide an experimental and numerical analysis of the self-heating and thermal distribution of a 2 section slotted laser. Having a better understanding of the temperature distribution along the laser cavity will assist in designing semiconductor lasers with enhanced energy performance.

## 2. Laser Structure and Thermal Modelling

A single mode slotted grating laser, shown in figure 1, was used in this work. The laser cavity is formed by a 2  $\mu\text{m}$  wide ridge. The ridge is separated into a 160  $\mu\text{m}$  unslotted gain section and a 240  $\mu\text{m}$  grating section in which 24 slotted are etched. The gain and grating sections are both active and are both contacted with gold pads which are electrically isolated from each other, allowing independent current injection. The front and back facets are coated with anti-reflection and high reflection coatings respectively. Simulation and characterisation of slotted lasers can be found in [3], [4], and [5].

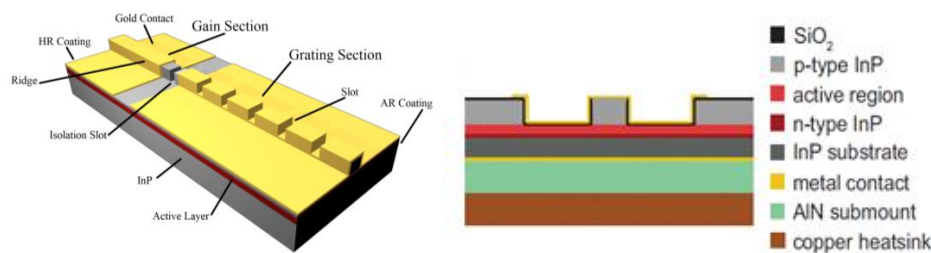


**Figure 1.** (a) 3-D representation and (b) cross-section showing material structure of the laser studied in this work.

## 3. CCD Thermo-Reflectance measurements

In this work the temperature distribution of a slotted laser, as shown in figure 2 (b), is determined by means of charged coupled device thermo-reflectance (CCD-TR) microscopy. This technique makes use of the fact that the

reflectivity of some materials varies with temperature. The relationship between reflectivity and temperature is given by

$$\Delta R = \frac{1}{R} \frac{\partial R}{\partial T} = \kappa \Delta T$$

where  $\kappa$  is the thermorelectance coefficient. The thermorelectance coefficient depends on material, wavelength, numerical aperture of the imaging system and can be modified by transparent overlayers, as such it must be calibrated for each specific system. Gold, the contact material used in the laser studied herein, was found to have a  $\kappa$  of  $-1.57 \times 10^{-4} \text{ K}^{-1}$  at 515 nm, allowing the measurement of the temperature distribution of the upper surface of the laser diode. The experimental setup is shown in Fig. 2(a). The laser is illuminated with a green LED. The reflected light is passed through a narrowband filter centered at 515 nm and is detected by a CCD camera. An in-depth analysis of CCD-TR can be found in Farzaneh et al [6]. The measured temperature rise due to laser operation of the device outlined in section 2 is shown in Fig. 2(b). Both sections are biased with 100 mA. The full 2D temperature map is shown in Fig. 2(c). The laser chip is in contact with a heatsink that is maintained at 20 °C with a Peltier module. A large temperature rise of approx. 32 °C rise can be observed in the gain section, compared to an approx. 14 °C rise in the grating.

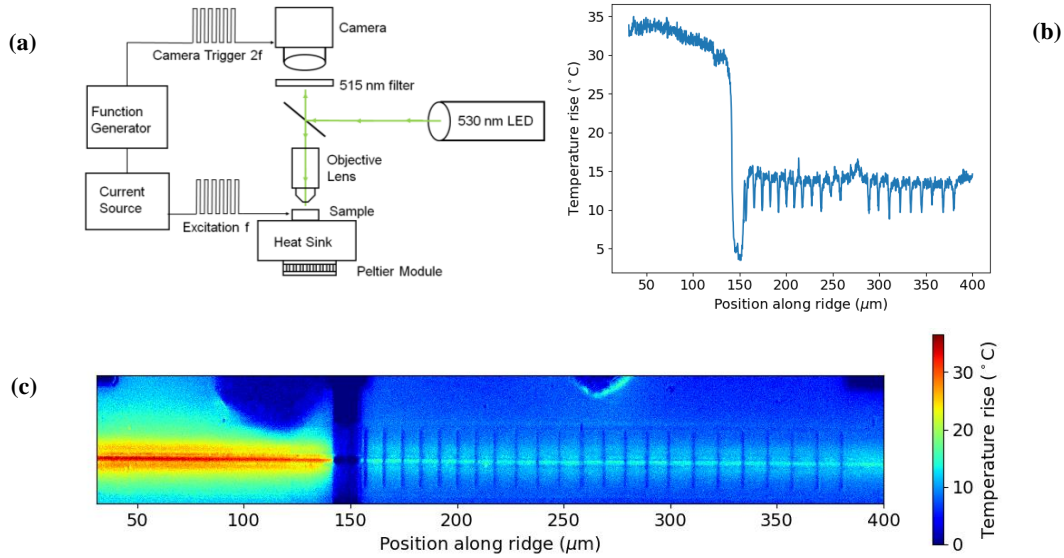


**Fig. 2.** (a) Schematic of the CCD-TR setup. (b) Experimentally determined temperature distribution along the laser ridge with 100mA injection in both sections. (c) Experimental temperature map of the laser surface.

#### 4. Conclusions

In this work we demonstrate the high resolution thermal imaging of a two section semiconductor laser. We show that there can be a significant difference in the local temperature rise in each section under the same input current which would not be easily picked up by monitoring wavelength drift. CCD-TR microscopy has been shown to be an effective tool for analyzing local temperature distributions in these devices which can serve as input for device modelling.

#### 5. References

- [1] M.J. Wallace, R. O'Reilly Meehan, R. Enright, et al "Athermal operation of multi-section slotted tunable lasers," *Opt. Express* 25, 14414-14426 (2017).
- [2] D. McCloskey, R. O. Meehan, M. J. Wallace, R. Enright, and J. F. Donegan, "CCD-based thermorelectance measurements of a multi-section slotted laser," in *2017 Conference on Lasers and Electro-Optics (CLEO)*, pp. 1-2, 2017.
- [3] Q. Lu, W.-H. Guo, D. Byrne, and J. Donegan, "Design of slotted single-mode lasers suitable for photonic integration," *IEEE Photonics Technol. Lett.* 22, 787-789 (2010).
- [4] A. Abdullaev *et al.*, "Improved performance of tunable single-mode laser array based on high-order slotted surface grating," *Opt. Express, OE*, vol. 23, no. 9, pp. 12072-12078, May 2015.
- [5] A. Abdullaev *et al.*, "Linewidth Characterization of Integrable Slotted Single-Mode Lasers," *IEEE Photonics Technology Letters*, vol. 26, no. 22, pp. 2225-2228, Nov. 2014.
- [6] M. Farzaneh *et al.*, "CCD-based thermorelectance microscopy: principles and applications," *J. Phys. D: Appl. Phys.*, vol. 42, no. 14, p. 143001, (2009).

**Acknowledgements:** This project was funded by Science Foundation Ireland under project number 15/IA/2854.

# Semiconductor Fano lasers

Jesper Mork\*, Thorsten S. Rasmussen, Yi Yu, Dagmawi Bekele,  
Elizaveta Semenova, Aurimas Sakanas, and Kresten Yvind

DTU Fotonik, Dept. of Photonics Engineering, Technical University of Denmark, DK-2800 Kgs.Lyngby, Denmark  
\*jesm@fotonik.dtu.dk

**Abstract:** We discuss the use of Fano resonances for improving the properties of integrated opto-electronic devices, focusing on the fundamental properties and possible applications of semiconductor Fano lasers.

## Summary

A Fano resonance [1] arises by the interaction of a continuum of modes and a discrete mode and arises in many different physical systems, including plasmonics and photonics [2]. We have shown that by using a Fano resonance as one of the mirrors in a laser cavity, one gets a very rich system with new possibilities for ultra-fast modulation and pulse generation [3]. A schematic of the Fano laser, implemented in a photonic crystal membrane structure, is shown in Fig. 1. The laser was recently demonstrated experimentally [4].

In this talk we will explain the fundamental properties of semiconductor Fano lasers [5], which may be considered to be based on a so-called bound-mode-in-the-continuum [6]. In contrast to conventional lasers, the semiconductor Fano laser can be modulated via the Fano mirror, which enables FM-modulation of the laser at modulation speeds far exceeding the relaxation oscillation frequency [3]. By exploiting nonlinearities in the nanocavity constituting the Fano mirror, one can also realize a regime of short-pulse generation [3,4].

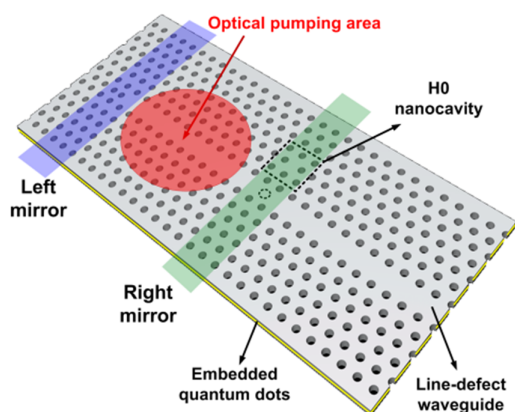


**Fig. 1.** Schematic of a Fano laser realized in an InP membrane structure. The waveguide and nanocavity are implemented as a line-defect and a point-defect in the crystal lattice of air-holes. The left laser mirror is a conventional photonic crystal mirror and the right mirror is implemented as a Fano resonance. The gain is provided by quantum dots embedded in the membrane structure and are pumped optically in such a way that only the dots in the main laser cavity are excited.

Since integrated optical isolators suitable for integrated photonic circuits are not available, lasers used in such circuits need to be robust towards feedback from interfaces, waveguides, etc. Recent theoretical results show that Fano lasers are inherently much more stable towards feedback than conventional lasers; i.e. the transition to coherence collapse occurs at feedback levels that are several orders of magnitude higher. In the talk we will characterize and analyze this increased feedback sensitivity.

## 5. References

- [1] U. Fano, Phys. Rev. **124**, 1866 (1961).
- [2] A. E. Miroshnichenko, S. Flach, and Y. S. Kivshar, Rev. Mod. Phys. **82**, 2257 (2010).
- [3] J. Mork, Y. Chen, and M. Heuck, Phys. Rev. Lett. **113**, 163901 (2014).
- [4] Y. Yu, W. Xue, E. Semenova, K. Yvind, and J. Mork, Nature Photon. **11**, 81 (2017).
- [5] J. Mork, Y. Yu, T. S. Rasmussen, E. Semenova, and K. Yvind, IEEE J. Select. Top. Quantum Electron. **25**, 2900314 (2019).
- [6] C. W. Hsu et al, Nature Reviews Materials **1**, 16048 (2016)

# Optical coupling of quantum-dot micropillar lasers with perspective towards neuromorphic computing

Xavier Porte\*

FEMTO-ST Institute/Optics Department, 15B avenue des Montboucons, 25030 Besançon Cedex, France  
\*javier.porte@femto-st.fr

**Abstract:** I will review latest findings on optical coupling of quantum-dot micropillar lasers, putting those results in the context of future application to neuromorphic computing.

Optical coupling of semiconductor lasers is a long and fertile research field that has explored fascinating nonlinear dynamics and has unveiled interesting applications for these devices [1,2]. Lately, the interest for an even-further miniaturization and integration of semiconductor lasers has pushed this field closer to the nanoscale, where cavity quantum electrodynamics (cQED) effects become relevant and optically coupled microlasers show new and interesting properties [3]. Here, I will review latest findings on optical coupling of quantum-dot (QD) micropillar lasers in experiments performed at the Technical University of Berlin in the group of Stephan Reitzenstein using QD micropillar samples grown at the University of Würzburg. Complex behavior resulting from optical injection and delayed feedback of QD micropillar lasers will be discussed, focusing on the demonstration of mutual coupling and synchronization [4-6]. Understanding the behavior of micropillar lasers in these optical coupling configurations is relevant to utilize them in photonic neuromorphic computing schemes like artificial neural networks.

Artificial neural networks (ANNs) are very successful brain-inspired computing architectures based on computing principles different from those of classical algorithmic computing. Particularly, recurrent Neural Networks are nonlinear dynamical systems capable to process and classify complex information or predict chaotic signals with excellent performance. Moreover, physical implementations of recurrent Neural Networks typically benefit from reservoir computing approach, where input weights and internal connection weights are not individually optimized [7], drastically reducing the complexity to train such physical ANNs. In the second part of this work, I will present an approach to use arrays of QD micropillar lasers as photonic neurons in ANNs, profiting from the several intrinsic nonlinearities of these lasers. We will follow the diffractive coupling scheme introduced in [8] to create a complexly coupled network of vertically emitting QD micropillar lasers. The arrays of QD micropillar lasers are grown in the same group at Technical University of Berlin, where they have recently overcome the challenge to grow large laser arrays maintaining uniform emission wavelengths [9]. By using an analogous diffractive coupling architecture, our group at FEMTO-ST Institute demonstrated networks of thousands optically coupled Ikeda maps collectively performing chaotic time-series prediction tasks with state-of-the-art performance [10]. In the experiments with QD micropillar lasers, we will speed up this successful scheme by nine orders of magnitude, matching the GHz dynamics bandwidth of such microlasers.

## References

- [1] M. C. Soriano *et al*, "Complex photonics: Dynamics and applications of delay-coupled semiconductor lasers," *Rev. Mod. Phys.*, vol. 85, pp. 421-470 (2013).
- [2] M. Sciamanna and K. A. Shore, "Physics and applications of laser diode chaos," *Nat. Photon.*, vol. 9, Iss. 3, pp. 151-162 (2015).
- [3] A. Carmele *et al*, "Single Photon Delayed Feedback: A Way to Stabilize Intrinsic Quantum Cavity Electrodynamics," *Phys. Rev. Lett.*, vol. 110, Iss. 1, p. 013601 (2013).
- [4] S. Holzinger *et al*, "Tailoring the mode-switching dynamics in quantum-dot micropillar lasers via time-delayed optical feedback," *Optics Express*, vol. 26, no. 17, pp. 22457-22470 (2018).
- [5] E. Schlottmann *et al*, "Injection Locking of Quantum-Dot Microlasers Operating in the Few-Photon Regime," *Phys. Rev. Applied*, vol. 6, Iss. 4, p. 044023 (2016).
- [6] S. Kreinberg *et al*, "Mutual coupling and synchronization of optically coupled quantum-dot micropillar lasers at ultra-low light levels," *Nature Communications*, vol. 10, Iss. 1, p. 1539 (2019).
- [7] H. Jaeger and H. Haas, "Harnessing nonlinearity: predicting chaotic systems and saving energy in wireless communication," *Science*, vol. 304, no. 5667, pp. 78-80 (2004).
- [8] D. Brunner and I. Fischer, "Reconfigurable semiconductor laser networks based on diffractive coupling," *Optics Letters*, vol. 40, Iss. 16, p. 3854 (2015).
- [9] T. Heuser *et al*, "Development of Highly Homogenous Quantum Dot Micropillar Arrays for Optical Reservoir Computing," *IEEE JSTQE*, vol. 26, Iss. 1, pp. 1-9 (2020).
- [10] J. Bueno *et al*, "Reinforcement learning in a large-scale photonic neural network," *Optica*, vol. 5, Iss. 6, pp. 756-760 (2018).

# Neuromorphic photonic circuits with VCSEL-based artificial spiking neurons

J. Robertson, M. Hejda, J. Bueno, E. Wade, A. Hurtado\*

*Institute of Photonics, Dept. of Physics, University of Strathclyde, Glasgow, Scotland, UK.  
\*antonio.hurtado@strath.ac.uk*

**Abstract: We demonstrate basic neuromorphic (brain-inspired) processing functionality at ultrafast speed rates using artificial photonic spiking neurons based upon Vertical-Cavity Surface-Emitting Lasers (VCSELs). We report here experimentally on controllable ultrafast spiking ( $10^7$  times faster than biological neurons) for memory systems and the emulation of retinal neuronal circuits. These neuro-inspired photonic systems, based on inexpensive, compact, off-the-shelf components offer high promise for novel applications in emerging neuromorphic computing technologies for information processing and artificial intelligence.**

## 1. Introduction

The emulation of biological neuronal responses using electrical and optical techniques has been receiving growing research interest for novel neuro-inspired (neuromorphic) computing architectures and Artificial Intelligence (AI) technologies. In recent years, largely impressive electronic neuromorphic systems capable of simulating up to one million neurons have emerged, helping us better understand these spike-based systems and how they operate [1-2]. However, as of late, photonics-based realizations of neuromorphic information processing systems have begun to surface due to the unparalleled advantages of light based technologies. Neuromorphic information processing in the optical domain makes use of the ultrafast speeds (up to 7 order of magnitude faster than biological neurons), wavelength-division multiplexing capabilities, low crosstalk and large bandwidths unavailable to electrical-based systems [3]. Semiconductor lasers have been the dominant systems behind many of the recent photonic realizations of neuromorphic systems with Vertical-Cavity Surface Emitting Lasers (VCSELs) being one of the most popular of platforms among a plethora of options. Compact VCSELs are indeed great candidates for artificial photonic neurons as their low cost, high interconnectivity, compatibility with telecommunication platforms and complex non-linear dynamics make for controllable, scalable neuron-like models compatible with future photonic communication and computing networks [4].

In this work we present our recent experimental results investigating ultrafast spiking VCSEL-Neurons with autaptic (self-feedback) connections for spiking photonic memory systems and VCSEL-neuron circuits emulating neuronal circuits in the retina. The spiking dynamics produced in this work are generated using modulated optical injection as demonstrated in previous works [5-8] and behave similar to biological neurons but at ultrafast speeds. These results show how simple biological circuits can be emulated using these devices and how spiking signals can be fed back into a VCSEL-Neuron to produce repeating memories. These results demonstrating the emulation of biological neuronal systems with ultrafast photonic technologies offer promise for future photonic spiking processing platforms yielding functionalities such as pattern recognition, learning and pattern storage as it is performed in the brain.

## 2. Experimental Setup

The experimental setup used in our first demonstration of ultrafast spiking memory (Fig. 1) is made up of a tunable master laser (ML) injecting light into a VCSEL-Neuron. The optical injection is amplitude-modulated using a Mach-Zehnder modulator and controlled using a pulse generator. The output of our VCSEL-Neuron is split into two where half is (1) analyzed at detection using a fast photodiode and a 13 GHz real-time oscilloscope and (2) fed back to the VCSEL-Neuron. In our second demonstration (Fig. 2) of retinal-neural functionality, a circuit of 3 cascaded VCSEL-Neurons emulates the operation of a photoreceptor in the eye (M-VCSEL), a non-spiking bipolar cell neuron (BC-VCSEL), and a spiking retinal ganglion cell neuron (RGC-VCSEL). Full details on the experimental setups used in this work can be found in [5].

## 3. Results and Discussion

Figure 1 depicts the results achieved for the implementation of a spiking memory system with a VCSEL-Neuron in autaptic configuration (under self-feedback). Here a single spike (red highlighted) is controllably activated in the VCSEL-neuron every 666ns following the arrival of external perturbations into the system. Fig. 1(a) shows that a first activated spike is successfully regenerated every 142ns (corresponding to the delay feedback loop length), hence creating a 142ns long memory of a 1-spike pattern. The continuation of this trace (Fig. 1(b)) shows the controlled activation of a second spike (red highlighted) following the arrival of a new perturbation that circulates alongside the previous spike. The resulting 2-spike pattern is then stored within the same 142ns temporal

memory. The temporal map (Fig. 1(c)) shows the consistency of the spiking memory across nine consecutive 142ns-long memory cycles. In Fig. 1(c) peaks of spike intensity appear yellow and troughs of minimum intensity appear dark blue. We have also observed that this spiking memory remains stable for a high number of cycles and that spike patterns of numerous spikes may exist in a single memory cycle.

Figure 2 shows our experimental results emulating the response of a basic neural circuit in the retina formed by three cascaded neurons, namely a photoreceptor, a bipolar cell and a retinal ganglion cell. Fig. 2(a) displays the photoreceptor-replicating modulated output of M-VCSEL used to injection-lock BC-VCSEL. Upon receiving the M-VCSEL input BC-VCSEL experiences a power drop but remains locked to the injection, creating a graded potential similar to bipolar cells in the retina (Fig. 2(b)). Consequently upon receiving the graded potential from BC-VCSEL, the injection locked RGC-VCSEL creates a neuronal spiking output analogous to the spiking signal in retinal ganglion cells (Fig 2(c)). This all-optical 3 VCSEL-Neuron circuit therefore successfully reproduces the functionality of biological retinal cells at ultrafast speeds which highlights the prospects of practical neural network emulation for future simulation and information processing platforms.

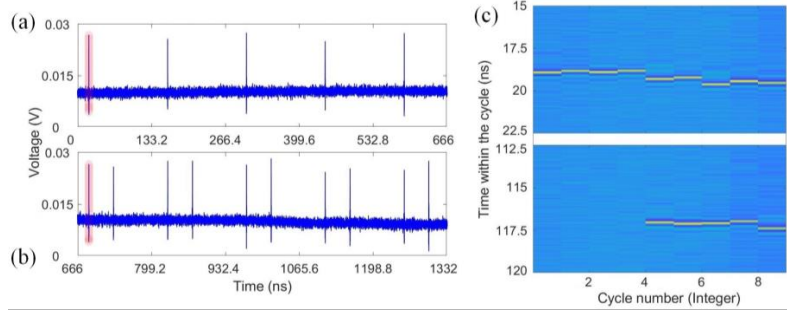


Fig. 1 – (a-b) Output time series of the VCSEL-Neuron showing controlled spike activation (red highlighted) and storage. (c) Temporal map corresponding to the time-series in (a-b) showing the consistency of the spiking across 9 memory cycles.

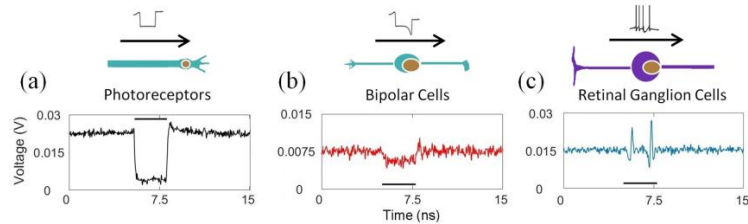


Fig. 2 – Schematic of retinal ON- type neuronal circuitry and the time-series output of the replicating (a) photoreceptor VCSEL (M-VCSEL), (b) Bipolar Cell VCSEL (BC-VCSEL) and (c) Retinal Ganglion Cell VCSELs (RGC-VCSEL).

#### 4. Conclusion

We report our recent experimental work on spiking memory systems and retinal neuronal circuit emulation with VCSEL-based artificial optical neurons. We demonstrate writing and storage of ultrafast spiking patterns in a VCSEL spiking memory, and the generation of graded and spiking potentials in VCSEL-Neurons towards the emulation of basic neuronal circuits in the retina but at ultrafast sub-ns speed rates. During the presentation we will also report on the foundations and properties of the VCSEL-Neurons as well as our current ongoing work in functional spiking processing circuits. These results outline the potential of ultrafast, compact VCSEL photonic neurons for future spike-based functionalities towards brain-inspired information processing and AI.

#### 5. References

- [1] B.V. Benjamin et al, “Neurogrid: A Mixed-Analog-Digital Multichip System for Large-Scale Neural Simulations,” *Proc. IEEE*, 102, 699 (2014)
- [2] S. Fuber et al, “The SpiNNaker Project”, *Proc. IEEE*, 102, 652 (2014)
- [3] P.R. Prucnal et al, “Recent progress in semiconductor excitable lasers for photonic spike processing” *Adv. Opt. Photon.*, 8, 228 (2016)
- [4] M. Turconi et al, “Control of excitable pulses in an injection-locked semiconductor laser”, *Phys. Rev. E*, 88, 022923 (2013)
- [5] J. Robertson et al, “Towards Neuromorphic Photonic Networks of Ultrafast Spiking Laser Neurons”, *IEEE J. Sel. Top. Quantum. Electron.*, 26, 7700715 (2020)
- [6] J. Robertson et al, “Controlled inhibition of spiking dynamics in VCSELs for neuromorphic photonics: theory and experiments”, *Opt. Lett.*, 42, 1560 (2017)
- [7] T. Deng et al, “Controlled Propagation of Spiking Dynamics in Vertical-Cavity Surface-Emitting Lasers: Towards Neuromorphic Photonic Networks”, *IEEE J. Sel. Top. Quantum. Electron.*, 23, 1800408 (2017)
- [8] A. Hurtado et al, “Controllable spiking patterns in long-wavelength vertical cavity surface emitting lasers for neuromorphic photonics systems”, *Appl. Phys. Lett.*, 107, 241103 (2015)

# Nanoscale light sources for neuromorphic nanophotonic circuits

B. Romeira,<sup>1\*</sup> P. Moura,<sup>1,2</sup> C. Maibohm,<sup>1</sup> and Jana B. Nieder<sup>1</sup>

<sup>1</sup>Department of Nanophotonics, Ultrafast Bio- and Nanophotonics Group, INL – International Iberian Nanotechnology Laboratory, Av. Mestre José Veiga n/a, 4715-330 Braga, Portugal

<sup>2</sup>Departamento de Ciência dos Materiais, Faculdade de Ciências e Tecnologia, Universidade Nova de Lisboa, Campus de Caparica, 2829-516 Caparica, Portugal

\*bruno.romeira@int.int

**Abstract:** We are witnessing an enormous effort towards integrated neuromorphic (brain-like) circuits as the hardware that can reproduce the neurotransmitter dynamic properties of neurons. Biological neurons encode information in sequences of intensity spikes. Here, we present our work towards the implementation of energy-efficient nanoscale semiconductor light-emitting sources for generation of spiking events, analogous to the signaling in neurons. Specifically, we will discuss the challenges of nano-light sources for ultralow current operation, fast pulse-based modulation and large scale integration for neuromorphic computing systems.

Neuromorphic photonic integrated circuits could take advantage of energy-efficient optical interconnects to achieve neuron-like responses at speeds much faster than neurons. However, efficient on-chip and chip-to-chip interconnection platforms require photonic components that consume much less energy than nowadays light sources. Nanophotonic light sources, and specifically nanolasers and nanolight-emitting diodes (nanoLEDs), show unique potential for small footprint, ultra-fast (>10 GHz) and low energy consumption (<10 fJ/bit) as required in high-density interconnected optical circuits [1]. Advances in this field will significantly boost the transmission and processing capabilities of optical chips [2], which are said to outperform electronic solutions in neuromorphic computing for artificial intelligence (AI) systems [3].

Despite much progress, neuromorphic circuits using nanoscale lasers [2] and nanoLEDs [4] suitable for generation of optical spiking analogous to neurons are lacking. Among numerous challenges, difficulties in achieving neuron-like nonlinear properties, poor light extraction, and large nonradiative recombination rates play a key role to realize efficient brain-inspired sources. Here, we present our recent work on artificial nanophotonic spiking neuron circuits using vertical-emitting metal-cavity nanopillars. These are formed by GaAs-based nanostructured compound semiconductors integrated with subwavelength cavities. Specifically, we will cover: i) passivation methods for suppression of nonradiative effects; ii) strategies for ultrahigh light extraction efficiency; and iii) metal-cavity design for enhancement of radiative emission. Lastly, we discuss the implementation of these nanoscale light sources for on-chip neuromorphic photonic circuits and interconnects.

In the future, novel neuron-inspired nanoscale semiconductor light sources as the ones discussed here are crucial to develop cognitive processors and sensing systems as well as to understand how the brain works.

## Acknowledgments

The work was supported in part by the Marie Curie COFUND Programme—NanoTRAINforGrowth II and in part by the European Union’s Horizon 2020 research and innovation programme through the H2020-FET-OPEN Project “ChipAI” under grant agreement 828841.

## References

- [1] D. A. B. Miller, “Attojoule Optoelectronics for Low-Energy Information Processing and Communications,” *J. Light. Technol.*, vol. 35, no. 3 (2017).
- [2] M. T. Hill and M. C. Gather, “Advances in small lasers,” *Nat. Phot.*, vol. 8, no. 908 (2014).
- [3] P. R. Prucnal and B. J. Shastri, *Neuromorphic Photonics*, CRC Press, Taylor & Francis Group, Boca Raton, Florida (2017).
- [4] V. Dolores-Calzadilla *et al.*, “Waveguide-coupled nanopillar metal-cavity light-emitting diodes on silicon,” *Nature Commun.*, vol. 8, Feb. 2017.

# Optical frequency comb generation via pulse excitation using step-recovery diodes in an optically-injected semiconductor laser

A. Rosado<sup>1\*</sup>, E. P. Martín<sup>2</sup>, A. Pérez-Serrano<sup>1</sup>, J. M. G. Tijero<sup>1</sup>, I. Esquivias<sup>1</sup> and P. M. Anandarajah<sup>2</sup>

<sup>1</sup> CEMDATIC - E.T.S.I Telecomunicación, Universidad Politécnica de Madrid (UPM), 28040 Madrid, Spain

<sup>2</sup> Photonics Systems and Sensing Lab, School of Electronic Engineering, Dublin City University, Glasnevin, Dublin 9, Ireland

\*Alejandro.rosado@upm.es

**Abstract:** We report on the experimental generation of a high-quality optical frequency combs (OFC) at low repetition rates. A Step-Recovery Diode (SRD) is used to gain-switch an optically injected semiconductor laser. The employment of an SRD as the electrical pulse generator allows us to produce high-quality OFCs with over 900 comb tones spaced by 100 MHz. These combs are compared with previously reported pulse pattern generator (square wave) driven gain switched combs. The use of SRDs reduces the cost, complexity and footprint of the OFC generation scheme enhancing its commercial viability.

## 1 Introduction

Optical spectroscopy is considered a crucial tool to understand the atomic and molecular structure of existing materials. Although there are several methods to retrieve the information of the material structure encoded in the optical spectra, the dual-comb (DC) approach has been recognized as one of the more useful and quicker methods [1]. In consequence, the generation of OFCs for DC spectroscopy has recently become very important [2], in particular at low frequencies (100 -500 MHz), as they provide high resolution in the absorption profiles. OFC generation in semiconductor lasers can be achieved utilising different techniques, i.e., gain switching (GS), mode-locking and electro-optic external modulation [3]. In previous publications [4], high-quality OFCs were generated by using a combination of optical injection and pulsed GS, employing square wave signals with different duty cycles and repetition rates (100 - 500 MHz). These square waves were produced by a pulse pattern generator (PPG). However, the use of a PPG for the generation of OFCs is not commercially feasible owing to its high cost and large footprint. In this abstract, we present for the first time as far as we know, an OFC generator consisting of an optically-injected gain-switched semiconductor laser using a step-recovery diode (SRD) as an electrical pulse generator. We compare the optical spectra generated by the PPG and SRD techniques to verify the differences in their characteristics.

## 2. Model description, experimental setup

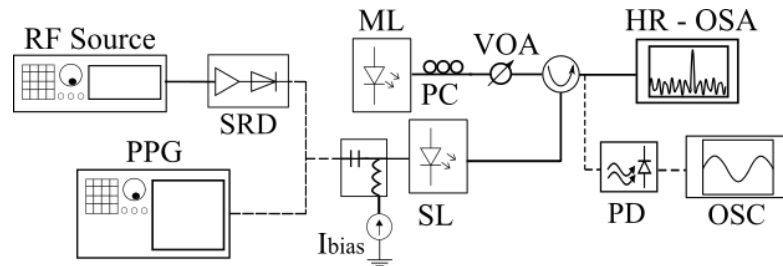


**Figure 1:** Schematics of the experimental setup for low repetition rate OFC generation: SRD: Step-Recovery Diode, ESA: Electrical Spectrum Analyzer, PPG: Pulse Pattern Generator, OSC: Oscilloscope, ML: Master Laser, SL: Slave Laser, PC: Polarization Controller, VOA: Variable Optical Attenuator, PD: Photodetector, HR-OSA: High-Resolution Optical Spectrum Analyzer.

The experimental setup is shown in Fig. 1. The OFC generator is built using a typical master-slave architecture. The master laser is a semiconductor wavelength tunable laser that can be tuned over the C-Band. The slave laser (SL), a discrete mode laser (DML), is gain-switched using a combination of a DC bias current and electrical pulses derived from a SRD that is driven with an amplified sinusoidal waveform at a frequency of 100 MHz. The spectral response of the optically-injected gain-switched laser is measured with a high-resolution (20 MHz) optical spectrum analyzer (OSA, AP2050A).

### 3. Results and discussion

Fig. 2 shows the optical spectra of the optically-injected semiconductor laser that is gain-switched with pulses from a SRD (Fig.2 (a) and (b)) and a PPG (Fig.2 (c)). The SRD, when driven with a 100 MHz sinusoidal signal amplified to a peak-to-peak amplitude of 20 V, generates inverted electrical pulses with a peak-to-peak amplitude ( $V_{RF-output}$ ) of 7 V. These pulses are used to modulate the SL. Under these driving conditions and without optical injection, the resulting optical spectrum is wide and continuous without discernible comb tones (not shown). This type of spectrum can be attributed to the lack of coherence between the optical pulses, as each pulse is built-up from spontaneously emitted photons with random initial phases. When external light is injected into the cavity, it acts as a seed for the phase, fixing the initial phase of the optical pulses and improving the coherence. The phase correlated pulses result in a high-quality OFC. The carrier-to-noise ratio (CNR) of the OFC shown in Fig. 2(a) is 16 dB, with 900 tones within 10 dB from the spectral peak. There is an equally impressive 730 tones within a 3 dB window from the spectral peak that are useful characteristics for spectroscopic applications. This spectrum was compared with an OFC generated by the same SL in similar driving conditions, but with an amplified 1% duty cycle square wave signal at 100 MHz provided by a PPG. (Fig. 2 (c)). In the latter case, the generated OFC exhibits good performance in terms of coherence, flatness and spectral width (CNR = 13 dB with 1120 peaks in the first 10 dB). Although, both techniques generate OFCs that are similar in shape and quality, the cost, size and energy consumption of the SRD is several orders of magnitude lower than the PPG.

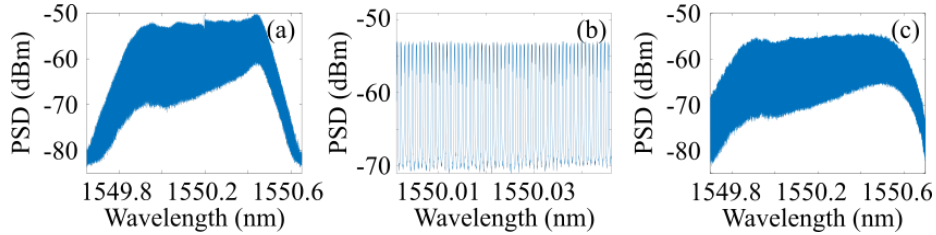


**Figure 2:** (a) Experimental optical spectrum using the PPG as the pulse source in the following driving conditions:  $f_R = 100$  MHz,  $I_{bias} = 1.7$  mA,  $V_{RF-output} = 7$  V and  $P_{opt} = -27$  dBm and  $\lambda_{inj} = 1550.2$  nm, (b) Zoom of Fig.2(a), (c) Experimental optical spectrum using the SRD-A as the pulse source in the following driving conditions:  $f_R = 100$  MHz,  $I_{bias} = 1.45$  mA,  $V_{RF-output} = 7$  V and  $P_{opt} = -25$  dBm and  $\lambda_{inj} = 1550.195$  nm

### 4. Conclusion

OFC generation in an optically injected gain-switched semiconductor laser at a low repetition rate by using an SRD as a pulsing source is experimentally demonstrated. We have compared the spectral quality of the generated OFC in two different scenarios: using a PPG and a SRD as pulsing sources. The performance of both devices as OFC generators in terms of coherence and bandwidth are similar. However, the SRD is a more suitable choice to generate OFCs at low repetition rate due to its characteristics, such as simplicity, easy integration, low cost and energy consumption.

### 5. References

- [1] Coddington, I, Swann, W, and Newbury, N, "Coherent Multiheterodyne Spectroscopy Using Stabilized Optical Frequency Combs" Physical Review Letters, 100, 013902, Jan 2008.
- [2] Jerez, B., Martín-Mateos, P., Prior, E., de Dios, C., & Acedo, P. "Dual optical frequency comb architecture with capabilities from visible to mid-infrared". Opt. Exp., 24(13), 14986-14994, 2016.
- [3] Imran, M., Anandarajah, P. M., Kaszubowska-Anandarajah, A., Sambo, N., & Potí, L. "A survey of optical carrier generation techniques for terabit capacity elastic optical networks". IEEE Commun. Surv. Tutor., 20(1), 211-263, 2018.
- [4] Rosado, A., Pérez-Serrano, A., Tijero, J. M. G., Valle, Á., Pesquera, L., & Esquivias, I. "Enhanced optical frequency comb generation by pulsed gain-switching of optically injected semiconductor lasers". Optics express, 27(6), 9155-9163, . 2019.

**Acknowledgments:** This work is supported by the Science Foundation Ireland SFI-15/CDA/3640), the SFI/European Regional Development Fund (13/RC/2077) and Ministerio de Economía y Competitividad of Spain (COMBINA, TEC201565212-C3-1-P and TEC201565212-C3-2-P). A. Rosado, A. Pérez-Serrano, J. M. G. Tijero and I. Esquivias also acknowledge support from Comunidad de Madrid and FEDER Program under grant SINFOTON2-CM (S2018/NMT-4326). A. Pérez-Serrano acknowledges support from the Programa Propio of the Universidad Politécnica de Madrid.

# Tunable Kerr frequency combs and cavity solitons in a nonlinear time-delayed Gires-Tournois interferometer

C. Schelte<sup>1,2,\*</sup>, A. Pimenov<sup>3</sup>, A. G. Vladimirov<sup>3</sup>, J. Javaloyes<sup>1</sup>, S. V. Gurevich<sup>2</sup>

<sup>1</sup> *Departament de Física, Universitat de les Illes Balears & Institute of Applied Computing and Community Code (IAC-3), C/ Valldemossa km 7.5, 07122 Palma de Mallorca, Spain*

<sup>2</sup> *Institute for Theoretical Physics, University of Münster, Wilhelm-Klemm-Str. 9 & Center for Nonlinear Science (CeNoS), University of Münster, Corrensstr. 2, D-48149 Münster, Germany*

<sup>3</sup> *Weierstrass Institute for Applied Analysis and Stochastics, Mohrenstr. 39, 10117 Berlin, Germany*

**Abstract:** In this work we show that a high finesse Gires-Tournois Interferometer (GTI) micro-cavity containing a Kerr medium, coupled to a external cavity and in presence of optical injection can give rise to phase-locked temporal dissipative solitons. These Localized Structures (LSs) possess a strongly asymmetrical oscillating tail which is the result of Third Order Dispersion (TOD) caused by the cavity. Dispersion is found to induce soliton molecules and tunable Frequency Combs. Because of the external locking to the injection field, the LSs are phase coherent with each other, and could be used for interferometric applications.

Our schematic setup is depicted in Fig. 1 (left) in which we show the intra-cavity field  $E$  and the external cavity field  $Y$ . We follow the approach of [1] that consists in solving the field propagation in the linear sections of the micro-cavity. That way one obtains a dynamical model linking the two fields  $E$  and  $Y$ . Their coupling is achieved considering the transmission and reflection coefficients of the top Distributed Bragg Mirror (DBR). After normalization, one obtains the rate equations for the fields  $E$  and  $Y$

$$\dot{E} = \left[ -1 + i \left( |E|^2 - \delta \right) \right] E + hY, \quad (1)$$

$$Y = \eta [E(t - \tau) - Y(t - \tau)] + \sqrt{1 - |\eta|^2} Y_0. \quad (2)$$

We scaled Eqs. (1-2) by the photon lifetime in the micro-cavity  $\kappa$ , and the field such that the Kerr effect value is unity. The cavity enhancement due to the highly reflectivity mirrors can be scaled out, making that  $E$  and  $Y$  are of the same order of magnitude. This scaling has the additional advantage of simplifying the input-output relation of the micro-cavity that reads simply  $O = E - Y$ . The minus sign represents the  $\pi$  phase shift of the incoming field  $Y$  upon

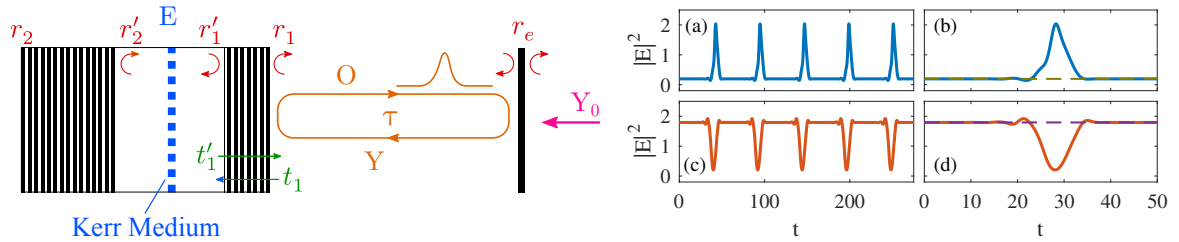


Fig. 1. (left) A schematic of the coupled cavity configuration.  $E$  denotes the field amplitude in the Kerr region. The output and injection fields in the external cavity are represented by  $O$  and  $Y$ , respectively. The round-trip time is  $\tau$ . (right) Pulse trains of bright (a) and dark (c) CSs as a function of time  $t$ . The respective pulse profiles are depicted in panels (b) and (d), respectively. Parameters are:  $(Y_0, \delta, h, \rho_e, \varphi, \tau) = (0.51524, 1.5, 2, 0.5, 0, 50)$ .

reflection from the top DBR. After a round-trip in the external cavity of duration  $\tau$ , the output field  $O(t - \tau)$  is re-injected with an attenuation factor  $\eta = r_e \exp(\varphi)$ , with  $r_e$  the external mirror reflectivity and  $\varphi = \omega_0 \tau$  the propagation phase, defining  $\omega_0$  as the carrier frequency of the field. The injected field is  $Y_0$ .

The system given by Eqs. (1,2) allows for the coexistence of both dark and bright solitons that live on high and low intensity continuous wave (CW) backgrounds, respectively. They are presented in Fig. 1 (right) where we show the pulse trains and the detailed temporal profiles. One can see the leading tail oscillations preceding the main pulse which are due to TOD induced by the GTI like micro-cavity. GTIs are used as optical elements with tunable second order dispersion. Yet, close to resonance, TOD becomes the leading term and causes strongly asymmetrical soliton profiles.

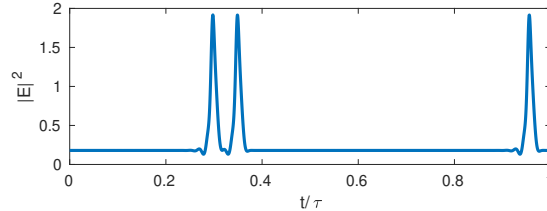


Fig. 2. A solution of Eqs. (1-2) showing a regime with a molecule of two LSs due to asymmetrical oscillating tail as well as an isolated LS.  $(Y_0, \delta, h, \rho_e, \varphi, \tau) = (0.5, 1.5, 2, 0.5, 0, 300)$ .

A typical regime from Eqs. (1-2) is depicted in Fig. 2 where we demonstrate the coexistence between a single LS and a LS molecule. The LS can be understood as the locking of fronts between the upper and lower CW states. Due to third order dispersion the fronts exhibit slowly decaying oscillating tails which induce, via their interaction, a series of preferred distances. Depending on parameters the fronts move slowly with respect to each other and a pair of fronts can lock together. The stability of such configurations is determined by the interplay between the interaction strength and the tendency of fronts to drift apart.

Since the governing time scale is the photon lifetime in the micro-cavity, the temporal separation between pulses is limited to typically 1 ns as found in [2], the density of the localized structure train can reach several hundreds of GHz. One can envision an external cavity of a few cm that will still be able to hold many LSs (considering that 1 cm corresponds to  $\simeq 50$  LSs). This compact system could be competitive with respect to micro-rings to generate portable frequency combs [3] while showing the tunable repetition rate, high optical power and the low jitter usually found in Vertical External-Cavity Surface-emitting lasers systems.

## References

- [1] J. Mulet et al., *Mode-Locking Dynamics in Electrically Driven VECSELS*, Journ. Quant. Elec. **41** (2005), pp. 1148
- [2] M. Marconi et al., *How Lasing Localized Structures Evolve out of Passive Mode Locking*, Phys. Rev. Lett. **112** (2014), pp. 223901.
- [3] H. Guo et al. *Mid-infrared frequency comb via coherent dispersive wave in SiN nanophotonic waveguides*, Nat. Phot. (2018)

# Mode-Hop Suppression by Cavity-Length Engineering in Hybrid External Cavity Photonic Crystal Lasers

R. Sheehan,<sup>1,2\*</sup> P. Singaravelu,<sup>1,2</sup> S. Butler,<sup>1,2</sup> G. Devarapu,<sup>1,2</sup> S. Hegarty,<sup>1,2</sup> L. O'Faolain<sup>1,2</sup>

<sup>1</sup>Centre for Advanced Photonics and Process Analysis, Cork Institute of Technology, Cork, Ireland

<sup>2</sup>Tyndall National Institute, Prospect Row, Cork, Ireland

\*[robert.sheehan@cit.ie](mailto:robert.sheehan@cit.ie)

**Abstract:** A hybrid external cavity Photonic laser was formed by butt-coupling a reflective semiconductor optical amplifier (RSOA) to a vertically coupled two-dimensional silicon (Si) photonic crystal cavity. Mode-hop free operation of the Photonic Crystal laser was attained by reducing the Fabry-Perot length of the laser cavity and without the aid of active mode locking mechanisms. The shorter length of the laser cavity ensures the selection of a single longitudinal mode under the bandwidth of the photonic crystal cavity reflection peak.

## 1. Introduction

Demand for high-bandwidth optical telecommunications is increasing. In [1] it is anticipated that by 2020 77% of global internet data traffic will take place within data-centres. It has been shown that silicon integrated photonics technologies have the potential to satisfy the high-bandwidth requirements in data centres [2]. A wide range of silicon integrated photonic devices, such as III-V-on-Si transmitters [3], Mach-Zehnder modulators [4] and high-speed photo-detectors [5] have been demonstrated in data-centre applications. In order to meet demand for low-cost transmitters the hybrid integrated external cavity laser (HECL) is being extensively studied. The HECL is formed by creating a laser cavity through butt-coupling a reflective semiconductor optical amplifier (RSOA) to a wavelength selective mirror fabricated in passive material such as silicon [6]. This hybrid approach is advantageous because it allows for the independent optimisation of each material system. In our case the wavelength selective mirror is formed by patterning a 2D photonic crystal cavity in silicon and the RSOA is a commercially available device [7]. The HECL is known to be power efficient, with reported wall-plug efficiency of 12.2 % [8], but it also suffers from mode-hopping, caused by thermally changes in the refractive index of the RSOA material as the amount of current in the device is increased [9].

In this paper we describe how to suppress mode-hopping in a hybrid Photonic Crystal (PhC) Laser through the use of cavity length engineering. We will show that by decreasing the total cavity length of the HECL mode-hopping can be prevented at RSOA operating currents of 100 mA. Typical HECL cavity lengths are on the order of 5000  $\mu\text{m}$ , this is due to the use of DBR structures as the wavelength selective mirror [9], however, in our approach we can achieve an HECL cavity length of 870  $\mu\text{m}$  since we are using 2D PhC cavities, which are approximately 20  $\mu\text{m}$  long. It is possible to achieve mode-hop free operation in HECL through the use of control electronics, however, this adds cost and sacrifices power efficiency [10]. Other advantages associated with the use of PhC cavities include the ability to lithographically define operating wavelengths [11] and the possibility of dense integration for WDM applications [12].

## 2. HECL Fabrication

The PhC cavity design used in this work is similar to that in that used in [13]. The PhC cavities have period of  $a = 390$  nm with hole radius of 90 nm, total length of the cavity is 20  $\mu\text{m}$ . Spin-on-glass (SOG) is used to fill-in the holes in the PhC cavity. This has the effect of improving the symmetry of the cavity mode and enhancing mechanical stability. To enhance coupling between the RSOA and the PhC cavity a polymer bus waveguide with cross-section area of 5  $\mu\text{m}^2$  is placed over the PhC cavity [14]. To vary the length of the laser cavity the PhC cavities were fabricated at different positions on the same Si chip. The loaded Q-factor of the fabricated PhC cavities was greater than 20,000.

A 400  $\mu\text{m}$  long, ridge waveguide geometry based RSOA was used as the gain chip for the PhC laser. The RSOA was butt-coupled with the Si chip to form a laser cavity. The RSOA consists of multiple quantum wells to emit photons by spontaneous emission. The quantum wells are made up of AlGaInAs/InP quaternary alloys. The back-facet of the RSOA waveguide is high-reflective (HR) coated with  $R > 90\%$  to provide the maximum reflection into the laser cavity and also to keep the minimum power loss at this interface. The front-facet of the RSOA waveguide is anti-reflection (AR) coated with  $R < 1\%$  to avoid the parasitic reflections from the RSOA and Si chip waveguide facets. The RSOA's are commercially available from the compound semiconductor fab [7]. The HECL is formed by aligning the RSOA chip with the Si chip using micro-manipulators. A schematic of the device is shown in Fig. 1.

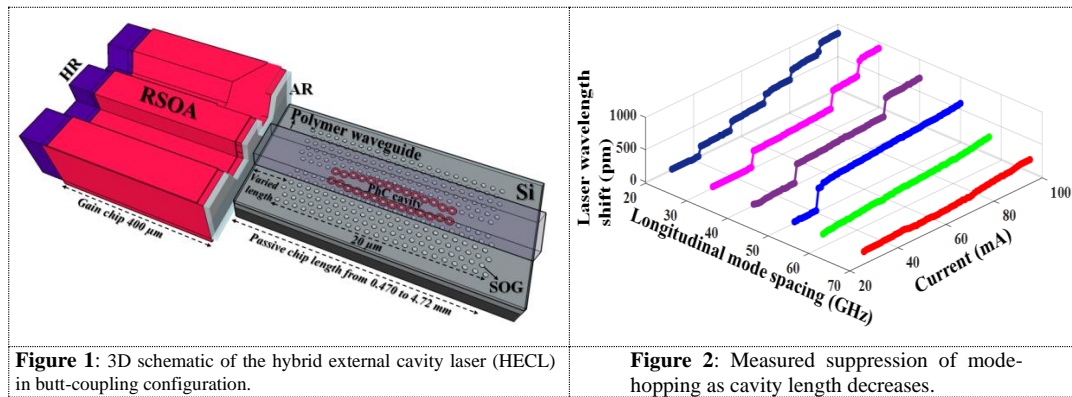


**Figure 1:** 3D schematic of the hybrid external cavity laser (HECL) in butt-coupling configuration.

**Figure 2:** Measured suppression of mode-hopping as cavity length decreases.

### 3. Mode-Hop Suppression Results

The ratio between the longitudinal mode spacing (LMS) and the full width half maximum of the PhC resonance the mode hopping behavior of the PhC laser see fig. 2. Two regimes of operation can be identified. If the LMS of the PhC Laser is greater than the FWHM (48 GHz) of the lasing PhC resonance peak then continuous stable single-mode lasing with increasing gain current. Conversely, if the LMS is less than the FWHM, multiple longitudinal modes lie with the reflection bandwidth of the PhC. As current is increased and the lasing wavelength changes as thermal effects alter the wavelength of the longitudinal modes of the laser cavity, competition occurs between the modes resulting in mode hopping. There is a corresponding effect on the side mode suppression ratio (SMSR). As the LMS increases (from ~15GHz to 50GHz) the SMSR shows a monotonic increase. Once the LMS exceeds the FWHM, the SMSR saturates at a value of 45dB.

### 4. Conclusion

We have shown that cavity length engineering can be used to realize mode hop free operation of a hybrid Photonic Crystal laser without active control. The ratio between the longitudinal mode spacing of the laser cavity and the full width at half maximum of the Photonic crystal cavity resonance has a very strong influence on the behavior of the laser, with the best results obtained for  $LMS > FWHM$ . The uniquely short length of the PhC resonator allows much shorter laser cavities than other approaches (e.g. silicon ring resonators), enabling mode free operation without the use of control electronics.

### 5. References

- [1] K. Zhong et al.: 'Digital Signal Processing for Short-Reach Optical Communications: A Review of Current Technologies and Future Trends,' J. Lightwave Technol., 36 (2), 2018.
- [2] T. Alexoudi et al.: 'Optics in Computing: From Photonic Network-on-Chip to Chip-to-Chip Interconnects and Disintegrated Architectures,' J. Lightwave Technol., 37 (2), 2019.
- [3] R. N. Sheehan et al.: 'Repeaterless data transmission at 1310 nm using silicon photonic integrated circuit,' Proc. SPIE Europe, pp 106860J, 2018.
- [4] J. Witzens, "High-speed silicon photonics modulators," Proc. IEEE, 106 (12), 2018.
- [5] J. Van Campenhout et al.: 'Silicon Photonics for 56G NRZ Optical Interconnects,' Proc. OFC, W11.1, 2018.
- [6] S. M. Butler et al., "Frequency modulated hybrid photonic crystal laser by thermal tuning," Opt. Expr., 27 (8), 2019
- [7] Compound Semiconductor Technologies, <https://www.cstglobal.uk/>, accessed august 2019
- [8] J-H. Lee et al., "Demonstration of 12.2 % wall plug efficiency in uncooled single mode external-cavity tunable Si/III-V hybrid laser," Opt. Expr., 23 (9), 2015.
- [9] A. J. Zilkie et al, "Power-efficient III-V/Silicon external cavity DBR lasers," Opt. Expr., 20(21), 2012.
- [10] J-H Lee et al., "III-V/Si hybrid laser stabilization using micro-ring feedback control," IEEE Phot. J., 8 (5), 2016
- [11] A. Liles et al., "Lithographic wavelength control of an external cavity laser with a silicon photonic crystal cavity based resonant reflector," Opt. Lett., 41 (5), 2016
- [12] K. Debnath et al., "Cascaded modulator architecture for WDM applications," Opt. Expr., 20 (25), 2012
- [13] K. Welna et al., "Novel dispersion-adapted photonic crystal cavity with improved disorder stability," IEEE J. Quant. Electron., 48(9), 2012.
- [14] K. Debnath et al., "Highly efficient optical filter based on vertically coupled photonic crystal cavity and bus waveguide," Opt. Lett., 38 (2), 2013.

# Frequency Locking Mechanisms enabled by Optical Frequency Comb Injection

K. Shortiss,<sup>1,2,\*</sup> B. Lingnau,<sup>1,2,3</sup> F. Dubois,<sup>1,2</sup> B. Kelleher,<sup>1,2</sup> and F. H. Peters<sup>1,2</sup>

<sup>1</sup>Department of Physics, University College Cork, Ireland

<sup>2</sup>Tyndall National Institute, Cork, Ireland

<sup>3</sup>Institut für Theoretische Physik, Technische Universität Berlin, Germany

\*kevin.shortiss@tyndall.ie

**Abstract:** We present experimental and theoretical results which show two separate frequency locking mechanisms that occur with optical comb injection. We show that the slave laser's relaxation oscillations can be frequency locked to rational fractions of the optical comb's spacing, and that the slave laser's frequency can also be fixed between the injected comb lines.

## 1. Introduction

Single frequency optical injection locking has been extensively studied since the first demonstration [1,2], and has been shown to improve laser linewidth and increase modulation bandwidths in devices. Recently, optically injecting locking has been considered as a method of demultiplexing optical combs [3]. In this work, we instead focus on using the nonlinear interaction between the comb and the slave laser to tune the output optical comb spacing. We present experimental and theoretical results which show the relaxation oscillations in a slave laser can be frequency locked to rational fractions of the optical comb spacing, and that the slave's lasing frequency can be fixed between comb lines, allowing the frequency spacing of the output comb to be tuned.

## 2. Experimental Setup and Model Description

To study the frequency locking of the slave laser's relaxation oscillations (ROs) and lasing frequency under the injection of an optical frequency comb, the experimental setup in Fig. 1 (a) was used. A Mach-Zehnder modulator was used to create a 3 line comb, which was injected into a slave laser using a circulator.

A rate equation model was used to model the optical injection, defined by the equations [4]:

$$\frac{d}{dt}E = (1 + i\alpha) \left( \frac{N - N_0}{2} - \kappa \right) E + \sqrt{\beta} (\xi'_{sp}(t) + i\xi''_{sp}(t)) + KE_0(1 + 2m \cos(\phi_{comb})) e^{i\phi_{inj}(t)} - i2\pi\nu_{inj}E,$$

$$\frac{d}{dt}N = \frac{J - N}{T} - (N - N_0)|E|^2, \quad \frac{\partial \phi_{comb}}{\partial t} = 2\pi\Delta + \sqrt{2\pi\Delta\nu_{comb}} \xi_{comb}(t), \quad \frac{\partial \phi_{inj}}{\partial t} = \sqrt{2\pi\Delta\nu_{inj}} \xi_{inj}(t).$$

Here, the  $E(t)$  is the complex electric field inside the cavity,  $N(t)$  the normalised active medium carrier density (in units of inverse time),  $J$  is the normalised pump current,  $N_0$  is the transparency carrier density,  $T$  is the carrier lifetime, and  $\alpha$  is the amplitude-phase coupling parameter. The optical cavity loss rate is given by  $2\kappa$ , where the strength of the spontaneous emission is controlled by  $\beta$ . The terms  $\xi'_{sp}$  and  $\xi''_{sp}$  provide complex Gaussian white noise sources.  $\Delta\nu_{comb}$  is the RF comb linewidth, with  $\Delta\nu_{inj}$  representing the optical linewidth. The two final terms in the complex field rate equation account for the modulated injected light, where  $K$  is the injection strength,  $\Delta$  is the optical comb spacing, and  $m$  is the relative strength of the injected side modes at frequencies  $\nu_{inj} \pm \Delta$ .

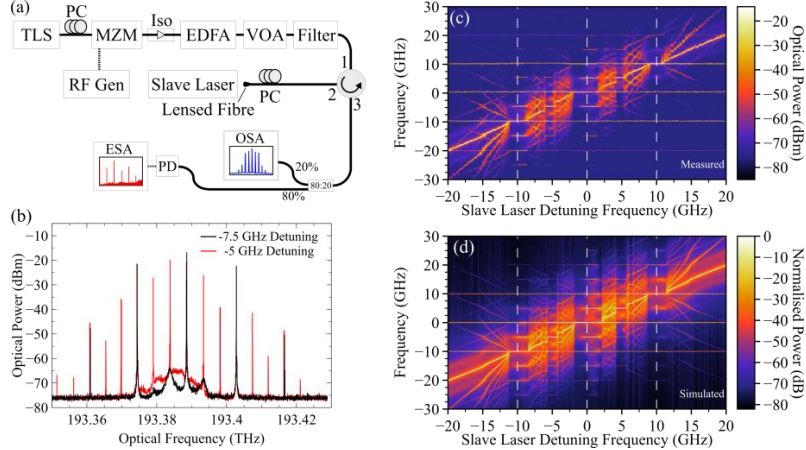


**Figure 1:** (a) Experimental setup. (b) Measured optical spectra which show the behaviour of the slave laser ROs at two different detunings, while the slave is under optical injection from a 14 GHz comb. (c) Measured and (d) simulated optical spectra as the detuning between the slave and centre line of a 10 GHz optical comb.

### 3. Results and discussion

Figure 1(b) shows measured optical spectra from a slave laser under injection from a 3 line 14GHz comb, at two different detunings. At -7.5 GHz detuning, the slave laser's spectrum shows the strongest three frequencies present are those in the injected comb, as the slave laser is stably locked to the centre line of the comb. As the detuning decreases, the relaxation oscillations in the slave become undamped, rising in optical power, until they frequency lock to a rational fraction of the comb spacing. For the case shown in Fig. 1(b), the ROs lock to 1/3 of the comb frequency spacing, in effect decreasing the output spacing of the comb. This harmonic frequency locking is enabled by an intensity modulation caused by the beating between the undamped ROs and the unlocked comb lines. The ROs can in fact lock to any rational fraction of the optical comb's frequency spacing. Figures 1 (c) and (d) show experimental and simulated detuning sweeps as a slave laser is tuned across a 10 GHz comb. Vertical dotted lines indicate where the slave's frequency matched that of a comb line. In both theory and experiment, the ROs can be seen to become undamped as the slave sweeps across each comb line.

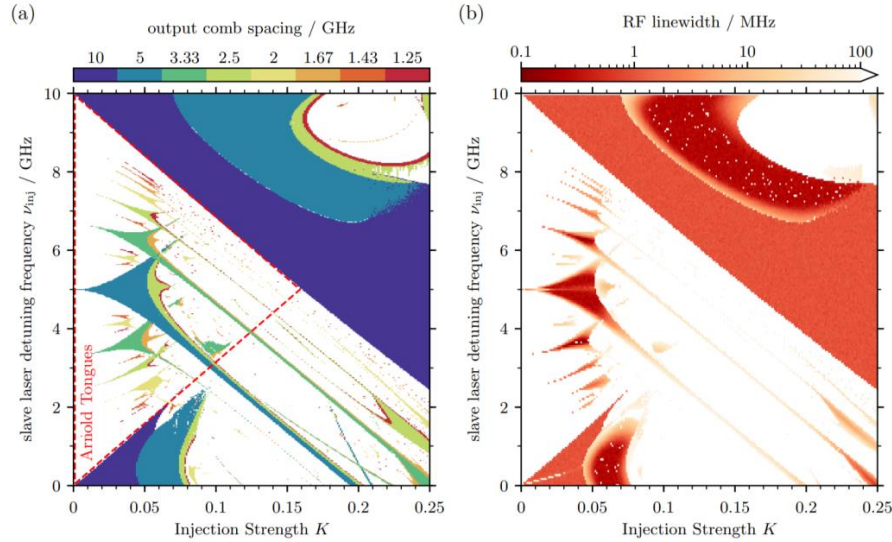


**Figure 2:** Two dimensional maps of the parameter space spanned by detuning and injected power. (a) Map of the output comb frequency spacing. White regions indicate unlocked states. (b) RF linewidth of the dominant harmonic's beat note.

As the slave laser tunes between the comb lines in Fig. 1(c) and (d), the slave's lasing frequency can also be observed to approximate a devil's staircase [5]. The slave laser's frequency becomes locked due to the periodic forcing caused by the neighbouring comb lines, and this forcing leads to regions of stable locking. Figure 2 shows two dimensional maps of the parameter space spanned by detuning and injected power for a 3 line 10 GHz optical comb. The output comb spacing is shown in Fig. 2(a), for a detuning span between two comb lines. Arnold locking tongues can be seen in between the two Adler locking cones (these cones are centred at 0 GHz and 10 GHz detuning), and appear approximately at detunings which are rational fractions  $p/q$  of the optical comb spacing. As the denominator  $q$  grows, the Arnold tongues are seen to shrink in size. Figure 2(b) shows the simulated RF linewidth over the same parameter space. Within both the RO locked regions and the Arnold tongues, the output linewidth can be seen to fall below the free running comb and the slave laser's linewidths (both assumed to be 1 MHz here), indicating that optical injection locking could be used to regenerate optical combs.

#### 4. Conclusion

We show that relaxation oscillations can be undamped and frequency locked to an injected optical comb, which in effect decreases the optical spacing of the output comb. The slave laser's frequency can also be fixed between the injected comb lines, which can create a comb with lower linewidth, while reducing the output comb spacing.

#### 5. References

- [1] Lang, R., "Injection locking properties of a semiconductor laser," *IEEE Journal of Quantum Electronics*, 18(6), 976–983. (1982)
- [2] Wiczorek, S., Krauskopf, B., Simpson, T. B., & Lenstra, D., "The dynamical complexity of optically injected semiconductor lasers," *Physics Reports*, 416(1–2), 1–128 (2005).
- [3] Cotter, W., Morrissey, P. E., Yang, H., O'Callaghan, J., Roycroft, B., Corbett, B., & Peters, F. H. "Integrated demultiplexing and amplification of coherent optical combs," *Optics Express*, 27(11), 16012. (2019).
- [4] Ohtsubo, J., "Semiconductor lasers: stability, instability and chaos," *Springer*, (2013).
- [5] Lingnau, B., Shortiss, K., Dubois, F., Kelleher, B., & Peters, F. H., "The Devil's Staircase in the Frequency and Amplitude Locking of Nonlinear Oscillators with Continuous Periodic Forcing," *arXiv:1905.01122*. (2019).

# **Spatiotemporal extreme events in spatially extended semiconductor lasers**

**G. Tissoni**

*Université Côte d'Azur, Institut de Physique de Nice, France*

In the last decades, extreme events have been under study in many different physical systems, from hydrodynamics to optics, where they have been identified as optical rogue waves. We present here some recent results about extreme events in spatially extended semiconductor laser systems with different geometries and configurations, spanning from broad area VCSELs (2D) with intra-cavity saturable absorber or coherent injection, to macroscopic ring semiconductor lasers (1D) with coherent injection.

In all of them we can identify regimes where the light emitted shows huge intensity peaks. We study the statistics of these peaks and shed some light on their possible generating mechanisms. Strong similarities with different types of dissipative solitons (cavity solitons, phase solitons) are also identified.